AC Losses in Superconducting Magnetic Bearings

Mohammad Siamaki

Paihau-Robinson Research Institute

Victoria University of Wellington

A thesis submitted for the degree of

Doctor of Philosophy

March 2023

Acknowledgements

First and foremost, I would like to express my deepest appreciation to my supervisors Prof. Rod Badcock and Dr. James Storey for giving me the opportunity to work on this project, for their extraordinary academic, technical, and moral support, and for pushing me to develop as an engineer.

I would also like to acknowledge Dr. Arsalan Hekmati who introduced me to the world of applied superconductivity, and for the insightful conversations we have had along the way.

I would like to extend my sincere thanks to Grant Kellett and Mike Davies for being there whenever I needed their incredible technical help and support. I am also grateful to Dr. Shen Chong, Dr. Xiyong Huang, Dr. Bart Ludbrook, Dr. Dominic Moseley, and Dr. Sriharsha Venuturumilli who generously provided knowledge and expertise. Thanks should also go to the lab technicians, office mates, research assistants, librarians, management team, and proof readers for their contribution, peer support, peer pressure, assistance, and editing help.

I am deeply indebted to my friends Digby, Gus, Negaar, and Vahid for making the past three years much more enjoyable and my life in New Zealand much easier. Thank you for being a wonderful bunch of people.

Words cannot express my gratitude to my family, especially my mother, Farangis, for their unlimited love and emotional support, and for encouraging me to do better in life and not settling for less.

Lastly, I would like to acknowledge the Ministry of Business, Innovation and Employment (MBIE) of New Zealand, who financed this work.

Abstract

Since the discovery of high-temperature superconductors, superconducting magnetic bearings have become an icon of applied superconductivity. Their ability to provide passive stable levitation/suspension has attracted much attention for industrial applications such as maglev trains, flywheel energy storage systems, and high speed electrical machines.

Paihau-Robinson Research Institute has been working on the design and construction of a 22 kW, 30000 rpm homopolar superconducting motor for a hybrid aircraft propulsion system. Superconducting magnetic bearings seem to be a potential solution to overcome the speed limits imposed by friction and heat in mechanical bearings. Considering the lack of commercial availability of superconducting bearings, the Institute has decided to investigate the challenges involved in developing suitable bearings for ongoing and future projects. The focus of this thesis is to explore the development of suitable low-loss bearings from bulk high-temperature superconductors, and to develop suitable test methodologies that allow the properties and behaviour of high-temperature superconducting bearings to be explored.

In order to accurately predict the behaviour of superconducting magnetic bearings, a precise knowledge about the non-linear voltage-current (E-J) relationship is required for input to simulations. Unlike coated conductors, this cannot be achieved by transport measurements in superconducting bulks. In this thesis, a convenient non-destructive method based on levitation force decay in superconducting bearings is introduced and evaluated to map the non-linear electrical properties in superconducting bulks. Furthermore, fibre Bragg grating sensors are employed in an actual superconducting bearing environment to monitor temperature at the bearing surface. Accurate cryogenic temperature monitoring with large electromagnetic fields present is of great importance in practical applications, and is problematic with conventional electronic sensors.

A barrier to commercial application is suspected to be the effects of inhomogeneous magnet, or superconducting, properties on the efficiency of bearings. The key drivers of this, AC loss mechanisms in superconducting bearings are investigated and a new analytical expression is proposed for hysteresis loss in superconducting bearings which takes magnetic field inhomogeneity, magnetic field periodicity, and loss surface distribution into account. This new expression is tested by performing spin-down experiments, and the results are found to be in good agreement.

Lastly, a high-speed superconducting motor/generator demonstration is built, which sets a record for the fastest superconducting bearing made in New Zealand. This will enable applications such as flywheel energy storage systems, direct-drive generators and high speed microfans to be explored whilst also providing the opportunity to demonstrate key technology elements such as flux-pumped high-temperature superconducting field windings and low-loss high-speed bearings. AC loss mechanisms at kHz-rated rotational frequencies are also studied with this prototype. The results show that at high rotational frequencies the superconducting

bulks are pushed into a resistive flux-flow regime, where AC losses are created by an eddy-current-like mechanism.

This thesis explores two phenomena of practical importance in superconducting bearings, and proves the principle of the application of superconducting bearings for ongoing and future projects in New Zealand.

Contents

List of Figures

List of Tables

Acronyms

AWG American wire gauge. 36

BLDC brushless direct current. 32, 36

COF coefficient of friction. 16, 18, 20, 63, 67–70

FBG fibre Bragg grating. 5, 14, 15, 21, 23, 31, 32, 41, 43, 48–52, 54, 59, 81, 82, 84

FC field cooled. 6, 7, 13, 14, 46, 64

FE finite-element. 3, 10, 11, 24, 41, 43, 59, 81

HTS high temperature superconductor. 1, 3–5, 10–24, 29–35, 37, 41, 46, 48–55, 57, 59–61, 63–65, 67, 68, 70–74, 76, 77, 79–82, 84

ID inner diameter. 32, 33, 35, 36

LTS low temperature superconductor. 1, 12

LVDT linear variable differential transformer. 29

OD outer diameter. 32, 33, 35, 36

PM permanent magnet. 1, 2, 8, 10, 11, 13, 15–21, 24–36, 43, 44, 46, 48–51, 54, 55, 59, 61–70, 72–74, 76, 80, 81, 84, 99–104

PWM pulse width modulation. 73

SMB superconducting magnetic bearing. 1–5, 8–16, 18–24, 26, 29–32, 34, 35, 41, 48, 49, 54, 55, 57–63, 65, 69, 72, 73, 79, 81–84

ZFC zero field cooled. 6, 7, 11, 13, 14, 28, 49, 55

1 Introduction

1.1 Introduction

The picture of a permanent magnet (PM) stably levitated above a high temperature superconductor (HTS) bulk submerged in liquid nitrogen (figure 1.1) is known as an icon of applied superconductivity and is a widely used demonstration of superconductivity in most introductory presentations in this field. Looking simple and yet magical, such a picture shows the two main features of superconductors namely zero DC resistance and diamagnetic response to a magnetic field, and has encouraged researchers to design and build non-contact bearings for rotating machinery.

Although superconducting magnetic bearing (SMB) technology has progressed significantly, especially after the discovery of HTS materials, they have not been widely adopted in practical applications. This has made this technology a great economic opportunity, since there is no SMB commercially available at the date of writing this thesis.

From an academic point of view, I have studied two main SMB parameters of practical importance, namely levitation force decay and AC losses in this thesis. From an applied point of view, I have attempted to prove the principle of SMB application, and to develop the capability of designing and building SMBs for technological projects being developed in New Zealand.

1.2 Problem Statement

Although the levitation phenomenon of using a low temperature superconductor (LTS) and a PM was observed in the 1940's, great effort has gone into taking advantage of this phenomenon to design and construct SMBs after the discovery of HTSs in 1986 [1].

SMBs have several advantages over conventional magnetic and mechanical bearings. As SMBs provide contactless rotation, they can make high rotational velocities possible, without any need for lubrication. In addition, type-II superconductors can provide stable levitation or suspension because of the flux pinning phenomenon, without the need for additional controllers to adjust the position of

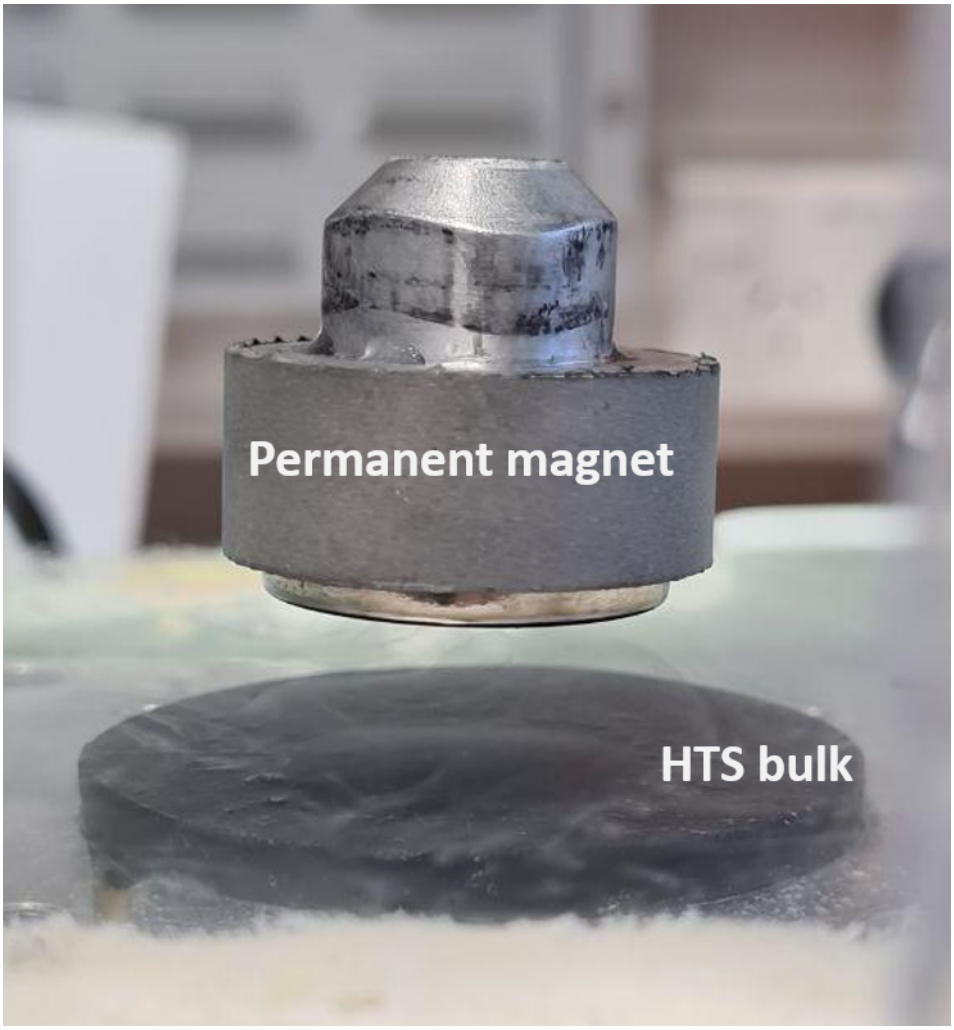

Figure 1.1: Photo of a NdFeB PM levitated above an YBCO bulk submerged in liquid nitrogen used in this thesis work.

the levitated/suspended body when subjected to disturbances. These advantages as well as their ability to operate in high vacuum environments have attracted huge interest from various scientific groups [1, 2]. Although great effort has gone into manufacturing prototypes, there are no commercially available SMBs in the market. Magsoar [3] claims that they produce a wide range of SMBs, however, there is no information available about their products.

SMBs seem to be the only efficient solution to overcome the speed-limit barrier in electrical machines, however, there are some issues that need to be addressed. An important issue about SMBs is the energy loss mechanism. Magnetic field inhomogeneity has been said to be one of the major sources of energy loss in SMBs [4], however, the relation between inhomogeneity and rotational loss (AC loss), and the precise impact of inhomogeneity on SMB dynamics have not been

experimentally investigated in a real rotating SMB environment. Another practical issue about SMBs is the relaxation of levitation force which is intrinsic to HTSs. Considering the relaxation mechanism, this phenomenon can be exploited to extract HTS bulk parameters non-destructively.

Therefore, the experimental evaluation of the relationship between magnetic field inhomogeneity and AC loss in SMBs, the impact of magnetic field inhomogeneity of dynamic behaviour of SMBs, and developing a non-destructive method to estimate HTS bulk parameters from levitation force decay mechanism in SMBs are the main academic goals of this thesis. Furthermore, considering the lack of commercial availability of SMBs, the global tendency to exploit this technology, and domestically-developed projects' requirements to achieve high rotational speeds, the applied goal of this thesis is to prove the principle of high-temperature superconducting bearings by designing and building prototype demonstrations. In order to achieve these goals, a finite-element (FE) model was used to simulate and predict the electromagnetic behaviour of HTSs as well as SMB parameters. Experimental rigs were designed and built to perform the designed experiments and to explore the academic goals of this thesis. A prototype kHz-rated motor/generator demonstration was designed, built, and successfully tested, enabling us to widen our understanding on this advanced technology and to domestically develop manufacturing capabilities.

1.3 Motivation

One of the main drawbacks of currently available electric machines is the speed limit imposed by their bearings. Electric machines can operate at high speeds with conventional bearings, but such bearings cannot withstand high speeds for a long time because the heat created by tribological losses can easily damage mechanical bearings [5–7]. Therefore, in applications where high operational speed is required, such as flywheel energy storage systems, centrifuges, reaction wheels, and hybrid aircraft propulsion systems, commercially available bearings cannot meet the speed requirement. SMBs can be considered as possible alternatives to conventional bearings. However there are some issues about SMBs that need to be addressed before construction.

Although SMBs offer contact-less rotation, they are not totally loss-free. When subjected to an alternating magnetic field, energy will be dissipated resulting in rotational drag. The AC loss in SMBs is one the most important parameters that must be taken into account when designing and constructing them. Despite the considerable studies done to measure and formulate the rotational loss, its

mechanism has not been precisely explained nor been explored in actual SMB environments. Exploring the AC loss mechanism can lead to the design and manufacture of SMBs with a reduced loss level and a higher efficiency.

SMBs operation is highly dependent on temperature, and requires reliable cooling systems to provide cryogenic temperatures below the critical temperature of superconductors. Although SMBs provide passive control, they do not offer high stiffness and damping compared to mechanical bearings, and may fail during large disturbances. However, these disadvantages, along with higher manufacturing costs, have not prevented research into developing and improving these bearings.

Some practical prototypes have been built and integrated into flywheels, but they are not commercially available. Accordingly, it is not possible to provide SMBs from suppliers and install them wherever needed. *Paihau-Robinson Research Institute* has been working on the design and construction of a 22 kW, 30000 rpm HTS motor for a hybrid aircraft propulsion system, and superconducting reaction wheels for satellites. In order to meet the technical requirements, such as levitation force, speed, stiffness, damping, and loss, a SMB should be designed, modelled, constructed, and then integrated into these systems.

1.4 Research Questions

The main theoretical and applied goals of this work have been explained in previous sections. The following objectives are included in this research:

1. Developing a non-destructive method based on a levitation force relaxation mechanism to estimate HTS assembly parameters in SMBs.

2. Investigating the AC loss and its relationship with magnetic field inhomogeneity in actual SMB conditions. This will provide a good comprehension of the main contributors to the AC loss, how they are affected by other parameters, and how they can be mitigated.

3. Designing, building, and testing a high-speed motor/generator demonstration in order to prove the principle and to develop our capabilities of manufacturing SMBs that can meet our project requirements.

To achieve these objectives, experimental test rigs have been designed and built at *Paihau-Robinson Research Institute* to measure the required data and compare them with simulation results.

1.5 Organisation of the Thesis

This thesis is split into seven main chapters:

- Chapter 1 covers the research questions, motivation to solve them, and main objectives of the thesis.
- The literature review chapter, after giving a brief overview of superconductivity and superconducting levitation, details the work conducted by other researchers to model and simulate superconductors and SMBs, followed by a review of the practical SMB parameters.
- Chapter 3 elaborates all methods used in this thesis and covers all the material needed to reproduce the experimental and simulation results presented in this thesis.
- Chapter 4 hypothesizes and develops a non-destructive method to estimate the flux creep exponent, or n-index, for HTS bulks. The method is tested on three individual SMBs. Furthermore, the application of fibre Bragg grating (FBG) sensors in an actual SMB system is introduced and tested in this chapter.
- Chapter 5 covers one the main academic goals of this thesis, where the relationship between magnetic field inhomogeneity and AC losses in an actual SMB environment, as well as the impact of inhomogeneity on the dynamic stiffness of the bearing, is discussed.
- Chapter 6 shows the design, build, and evaluation of a laboratory-scale kHz-rated motor/generator. This prototype has been serving as a visual demonstration of SMB technology, our institute capabilities, and the future of rotary machinery.
- Chapter 7 summarises the studies conducted and the results presented in this thesis, followed by some suggestions for future studies in this field.

2
Literature Review

2.1 Introduction

The first step in answering my research questions is to review what has been done up to date. This chapter gives a brief review of superconducting levitation and the underlying physics fundamental to this thesis. Since the focus of this thesis is AC losses in high temperature superconducting bearings, superconducting levitation is reviewed from a macroscopic point of view. The content of this chapter highlights the current state of the art and covers the work done up to the date of writing this thesis.

2.2 Superconductivity; Type-I and Type-II

Meissner and Ochsenfeld discovered magnetic exclusion and magnetic expulsion in superconductors in 1933, the latter of which is known as the Meissner effect [8]. This was an important discovery in superconductivity, because perfect conductivity (zero resistance for direct current) discovered by Onnes [9] was assumed to be the only feature of superconductors for many years. Meissner and Ochsenfeld discovered that when a lead tube was cooled to below its transition temperature T_c, and then a magnetic field was applied (zero field cooled (ZFC) condition), the superconductor showed diamagnetic behaviour and excluded the magnetic field like a perfect conductor (see figure 2.1). This diamagnetic behavior could be predicted by conventional electromagnetism. In another experiment, they cooled the superconductor in the presence of a magnetic field (field cooled (FC) condition). According to the conventional electromagnetism, they expected the magnetic field to be locked in the superconductor. But, they observed that the magnetic field was expelled from the interior of the tube, which was different to the expected response of a perfect conductor. Meissner effect, in fact, showed that superconductors are more than just perfect conductors with zero DC resistance. The two main features of superconductors, namely Meissner effect and zero resistance were formulated later by London brothers. The so-called "London equations" describe "the electromagnetic equations of the supra-conductor" and predict a finite length

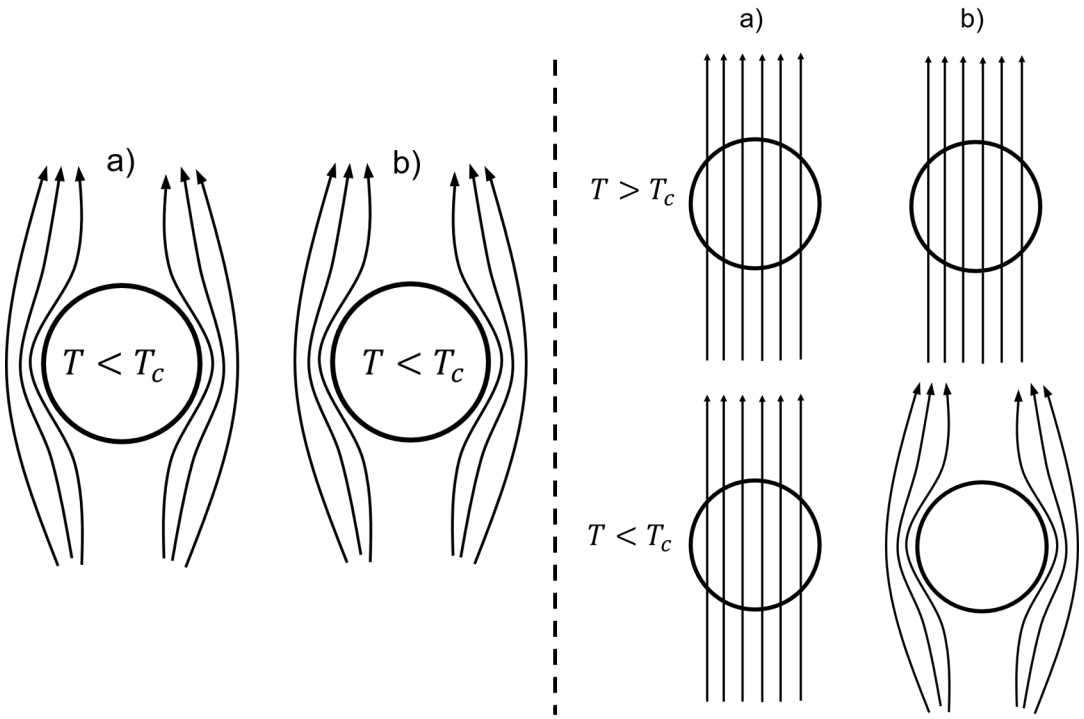

Figure 2.1: The schematic diagram of the response of a perfect conductor (a) and a superconductor (b) to an external magnetic field in ZFC condition (left) and in FC condition (right). The arrows indicate the external magnetic field applied to material domains shown by circles.

up to which a steady external magnetic field can penetrate into a superconductor to maintain a diamagnetic volume current [10].

The first experiments on magnetization of superconducting alloys were performed in 1937 [11] on Pb-Tl samples, where the authors attributed the gradual transition from superconducting to normal state to the inhomogeneity of samples. In 1952, Abrikosov defined a new group of superconductors as "superconductors of the second group" and formulated the theory of "vortex lattice" and "mixed state", when he could not fit experimental data on critical magnetic field of thin films to the Ginzburg-Landau theory [12]. According to "the theory of superconductivity" proposed by Ginzburg and Landau [13] and according to Abrikosov's studies, superconductors can be classified into type-I and type-II based on the ratio (κ) of their coherence length (ξ) to their penetration depth (λ).

Abrikosov's theory describes the dependence of magnetization on the applied magnetic field as follows (see figure 2.2): In type-I superconductors there is only one critical magnetic field H_c. The superconductor is in Meissner state and shows perfect diamagnetism for fields (H) smaller than the critical field, and superconductivity is completely destroyed and shows no magnetization as the applied field exceeds

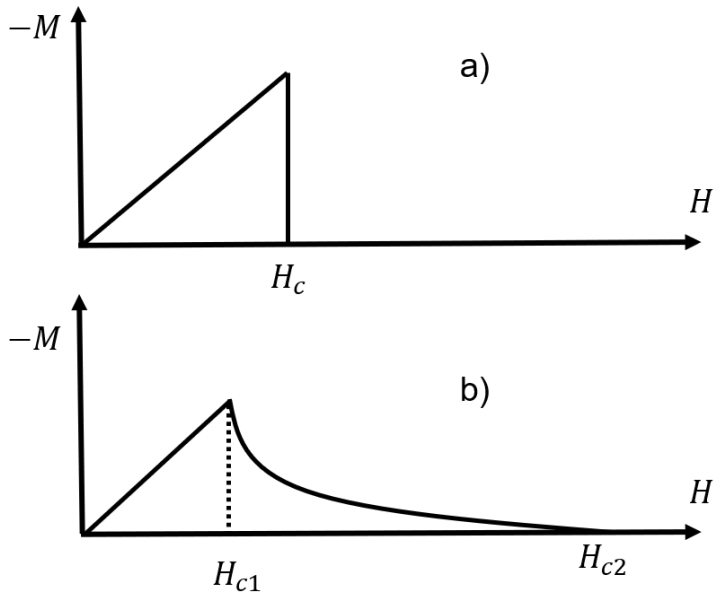

Figure 2.2: Schematic representation of magnetization in type-I (a) and type-II (b) superconductors.

the critical magnetic field. In type-II superconductors, however, there are two critical magnetic fields, namely H_{c1} and H_{c2}. For $H < H_{c1}$, type-II superconductors are in the Meissner state. As the applied magnetic field is increased and exceeds H_{c1} the magnetic field penetrates inside the superconductor in the shape of small cylinders called "vortices", all of which carry a quantized amount of magnetic flux of $\phi_0 = 2.068 \times 10^{-15}\, Wb$ [12, 14]. When the applied magnetic field exceeds H_{c2}, superconductivity is destroyed in type-II superconductors.

2.3 Superconducting Levitation

Since the discovery of superconductivity, many applications have emerged related to its special electrical and magnetic characteristics [15]. One of the most promising applications of superconductors is the SMB, where a PM can be levitated above a superconductor bulk or vice versa [4]. The first levitation experiment involving a superconductor was carried out in 1945, where a small cubic PM was levitated above a concave lead disc cooled by liquid helium [16]. Soon after, the deceleration rate of a superconducting lead sphere levitated in a magnetic field and cooled by helium was reported [17]. Proposals were made and prototypes were built for application of superconducting bearings in gyroscopes [18] and three phase electric motors [19]. Large-scale applications of superconducting levitation for transportation and rocket launchers emerged after niobium-titanium wires were made [20, 21].

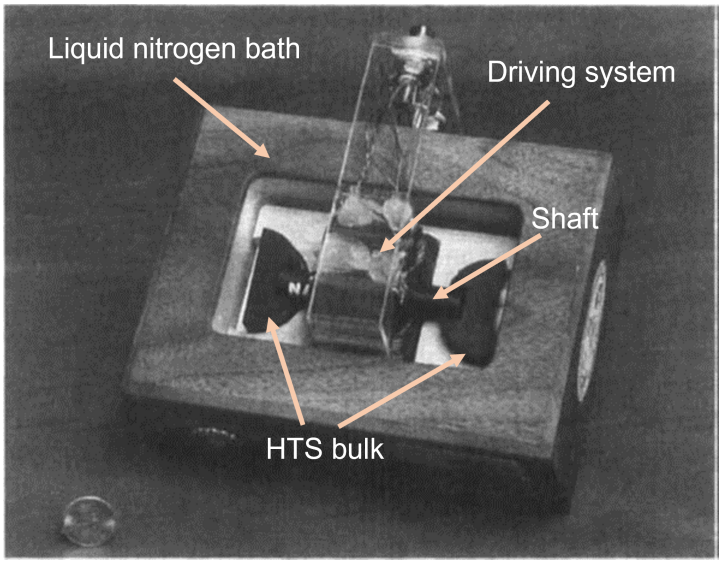

Figure 2.3: Photograph of a rotor levitated by two YBCO bulks cooled down in a liquid nitrogen bath. Figure reprinted from [28] with necessary permissions (Copyright © 2004 WILEY-VCH Verlag GmbH & Co. KGaA).

These early studies and applications of low-temperature superconductors, however, did not attract much attention because of the necessity of using expensive and complex liquid helium cryostats.

After the discovery of high-temperature superconductors in 1987 [22, 23], many laboratories resumed levitation studies using YBCO. Demonstrations of superconductivity at the temperature of liquid nitrogen (77 K) were reported in the same year, where the "pendulum test" and "floating magnet" experiments were carried out with YBCO and SmCo magnets [24]. Shortly after, high-temperature superconductors were proposed for bearing applications [25–27]. The first prototype high-temperature superconducting bearing was built and spun up to 10000 rpm in 1987 [28]. This bearing system was upgraded (see figure 2.3) in the next year and spun up to 120000 rpm [28]. Since then, the levitation applications of high-temperature superconductors in SMBs have progressed significantly and have been reviewed extensively elsewhere [1, 4, 28].

2.4 Stability in Superconducting Levitation

The most important advantage of high-temperature superconducting levitation over other kinds of levitation [26] is passive stability. According to Earnshaw's theorem, there is no stable equilibrium for a body placed in a repulsive or attractive static force field where force and distance are related by an inverse square law [4]. In electromagnetism, this theorem means that "a body with static charges,

magnetization, or currents placed in a static electric or magnetic field cannot be stably levitated or suspended under the action of electric and magnetic forces alone" [29]. This theorem simply explains why a system combined of any arbitrary set of PMs and electromagnets is inherently unstable, and why externally supplied active controllers are required to maintain stability in active magnetic bearings.

Earnshaw's theorem, however, does not govern diamagnetic materials. In 1939 [4], it was proved that adding a diamagnetic material ($\mu_r < 1$) to the system can provide stable magnetic suspension [4]. Although superconductors are not ideal diamagnets, they show diamagnetic behaviour in magnetic fields, and they can provide passive stability in levitation applications. Superconducting levitation in a type-I superconductor or a type-II superconductor in the Meissner state would be stable vertically but unstable horizontally; because in these situations the magnetic field of the PM is expelled from the interior of the superconductor and the levitated body will be repelled. In order to provide horizontal stability for a PM levitated above a type-I superconductor, the superconductor should be given a concave shape [16].

Stable superconducting levitation is only achievable with type-II superconductors in the mixed state, where the magnetic field penetrates inside the superconductor in the form of vortices. Inside each vortex, the material is in the normal state, surrounded by localized shielding currents. The trapping of vortices by spatial inhomogeneities is known as flux pinning. These inhomogeneities may exist naturally or be added artificially [30]. These vortices are analogous to mechanical springs attached to the levitated PM and the type-II superconductor, acting as stabilizing tools. These "springs" move the PM back to its initial position after being displaced by external forces [1, 4]. In fact, levitation of a PM above a superconductor arises from the diamagnetic response of the superconductor, and the passive stability of this levitation arises from flux pinning in type-II superconductors. This makes this group of superconductors the most technologically favorable materials for levitation applications, such as superconducting bearings.

2.5 Modelling

It is of great importance to model and simulate the electromagnetic response of HTSs and predict SMB key parameters such as levitation force, stiffness, and losses prior to construction. Efforts have been made to build analytical and numerical models among which the finite-element (FE) method has been widely developed to

solve different formulations such as $\boldsymbol{H}$, $\boldsymbol{A}$-$\boldsymbol{V}$, $\boldsymbol{T}$-Ω, etc. Detailed reviews about superconductor modelling are provided in [31–33].

The $\boldsymbol{E}$-$\boldsymbol{J}$ power law describing the nonlinear relation between electric field and current density inside superconductors, has been widely used alongside formulations to solve Maxwell's equations [31]. The general formula of the $\boldsymbol{E}$-$\boldsymbol{J}$ power law is:

$$\mathbf{E} = E_c \, (\frac{\mathbf{J}}{J_c})^n$$

Where E_c and J_c are the critical electric field and critical current density, respectively, and n is the power index which describes the flux creep in high-temperature superconductors. For $n = 1$, the power law reduces to Ohm's law in normal conductors. When n tends to infinity, it describes the Bean model [34], where the creep is not considered. For $1 \ll n < \infty$, the power law describes the creep. Various detailed expressions have been proposed to describe the relation between E and J, considering the temperature and magnetic field dependence of critical current density and n index [35].

Among the formulations mentioned above, H-formulation has become the most popular and versatile method for modelling the electromagnetic behaviour of HTS because of its accuracy, convergence, and ability to model various HTS applications. Comprehensive reviews of this formulation can be found in [31, 36].

In H-formulation, the state variable is magnetic field intensity $\boldsymbol{H}$, and the problem is formulated by combining Faraday's law and Ampere's law as:

$$\nabla \times \rho \nabla \times \mathbf{H} = -\mu_0 \frac{\partial \mathbf{H}}{\partial t} \tag{2.1}$$

where μ_0 is the permeability of free space and ρ is the resistivity of HTS given by the constitutive power law as:

$$\rho(|\mathbf{J}|, \mathbf{B}) = \frac{E_c}{J_c(\mathbf{B})} \left| \frac{\mathbf{J}}{J_c(\mathbf{B})} \right|^{n-1} \tag{2.2}$$

Equation 2.1 can be solved by home-made codes or by commercially available FE software such as *COMSOL Multiphysics* [31].

2.6 Levitation Force Decay

The relaxation of levitation force is one of the important parameters that needs to be taken into account when designing SMBs for practical applications. In a simple thrust bearing which consists of a PM disc and an HTS bulk, if the PM moves from its initial position in ZFC condition (point A in figure 2.4) towards

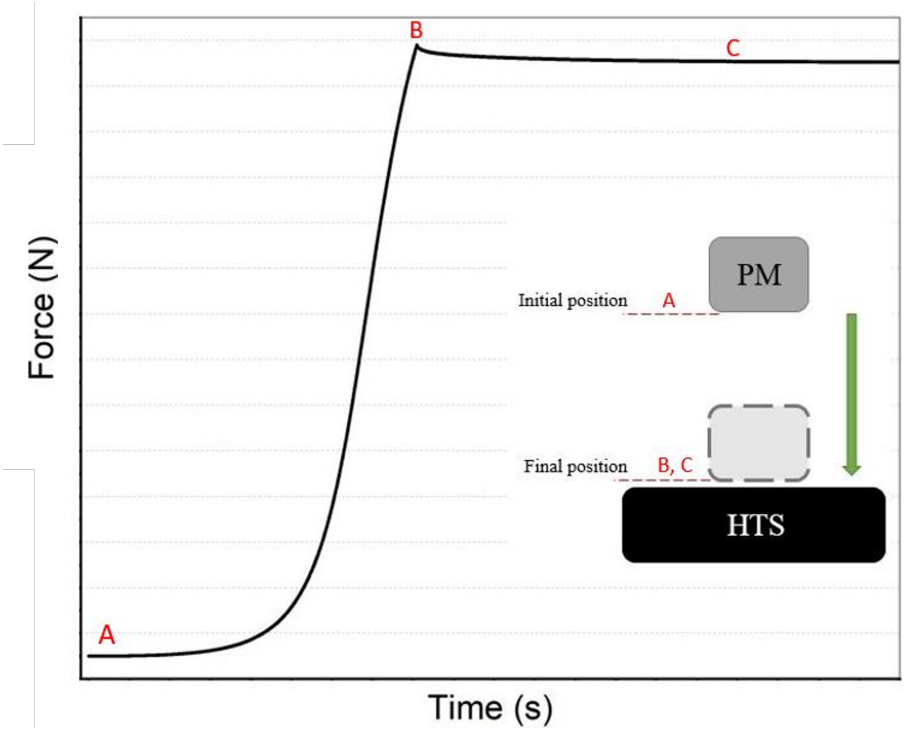

Figure 2.4: Illustration of a typical force decay in a simple thrust SMB.

the HTS bulk and then stops at its final position near the top surface of the HTS, the levitation force increases as the distance between them decreases, then it reaches a peak (point B) at the final position. Finally, it decays gradually with time and reaches a plateau (point C). This phenomenon has been reported widely in the literature [37–39], all of which has mentioned magnetic relaxation in high-temperature superconductors as the reason.

Magnetic relaxation in superconductors was first studied by Anderson and Kim in low-temperature superconductors, where they formulated the so-called "flux creep" theory [40, 41]. They proposed a logarithmic change of magnetic moment with time caused by thermally activated motion of Abrikosov flux lines in superconductor lattice. Although being a successful qualitative idea, the flux creep theory was roughly formulated and failed to explain some phenomena observed later in high-temperature superconductors [40, 41]. Soon after the discovery of HTS, researchers noticed the large size of magnetic relaxation in HTS samples compared to LTS. Since then, various models have been developed to deal with the magnetic relaxation in HTS from both microscopic and macroscopic points of view. A detailed review of these models can be found in [42].

According to a general flux creep theory, the flux is trapped at a pinning center; however, it can escape from there in a certain probability with the help of

thermal activation [43–45]. As a result, the force relaxation has been described as a consequence of the thermally activated flux creep in HTS. Therefore, the force decay behaves the same as the magnetization decay, i.e. logarithmically.

Tseng *et al.* studied the levitation force decay in three YBCO samples of different size as a function of temperature [46]. In their research, they conducted several measurements in ZFC condition and at different temperatures from 40 K to 85 K for three different sample sizes. They observed a logarithmic levitation force decay which increased with temperatures, and decreased with sample size. However, they did not discuss the relationship between the decay rate and temperature qualitatively.

The impact of initial cooling conditions, levitation height, and lateral displacement on levitation and lateral forces in a maglev test setup is reported in [47]. A detailed quantitative analysis of levitation and lateral forces has been made, which reports a logarithmic force decay. Their report, however, does not provide any qualitative analysis from a fundamental and/or applied point of view. Moreover, the experimental sequence would make any further analysis complicated, because the lateral force decay has been measured on an already-penetrated sample.

Liu *et al.* [48] investigated the effect of a varying external magnetic field on levitation force relaxation. In order to apply a varying magnetic field, they used an inhomogeneous rotating PM guideway, above which a YBCO assembly was levitated. They performed dynamic tests at different speeds and found that by increasing the rotation speed, the levitation force decays and this force attenuation becomes more intense at higher speeds. Following the spin-up tests, they performed slow-down experiments and reported that the levitation force recovers as the rotation speed decreases. They also observed that this recovery was slightly affected by repetitive acceleration and deceleration. This report is of significant importance when designing SMBs for high rotational speeds.

In order to study the levitation force and stiffness behaviour under the influence of reciprocating motion around the working height of a superconductor-magnet system and the grain orientation of YBCO bulks, Xu *et al* designed and conducted experiments in both ZFC and field cooled (FC) conditions [49]. According to their results, levitation force at the same operating height remains the same after several cycles of moving upward and downward under both cooling conditions. They explained this behaviour by flux distribution memory and said that after reciprocating motion, flux lines could be gradually and stably redistributed in a more optimal way, resulting in suppression of the levitation force decay. After such motion, magnetic stiffness tends to increase under ZFC and decrease under FC conditions, which affects the natural resonance frequency of the system. This study

was meant to mimic the real vibrations in HTS levitation systems. However, the amplitude of the reciprocating motions is much larger than what would happen in real vibrations. The impact of the rate of reciprocating motions could have been studied as it can influence the maximum levitation force and the shielding currents induced in YBCO bulks. The relaxation was reported as being logarithmic, but, no qualitative nor quantitative analysis of this decay and its relation to magnetic flux memory was reported.

2.7 fibre Bragg Grating (FBG) Sensors: Application in SMBs

fibre Bragg grating sensors [50] have been widely used in the field of applied superconductivity for temperature and/or strain measurement because of their numerous advantages over conventional electronic sensors. These sensors are light weight and small-sized. They are also electromagnetically insulated, which makes them a favorable option in high-field applications such as superconducting magnets. The low thermal conductivity of the fibre and thermal insulation between sensor and data processing unit allow FBG sensors to be employed at cryogenic temperatures [51–55].

The thermal expansion coefficient of a melt-textured YBCO sample was measured in orientations of its crystal planes (ab-direction and c-direction) by FBG sensors over the temperature range of $30-300$ K [56]. In this experiment, a block of YBCO was mounted on a copper disc which was in direct contact with the cold head of a cryocooler. The quantitative data analysis might be problematic because the impact of vacuum chamber deflection on strain was not taken into account. Moreover, they used a fibre with a single FBG in it mounted on the copper disc and used it as the reference sensor to subtract the temperature effect from the other sensors' readings. The authors have mentioned that the reference sensor was not mechanically attached to the copper disc to prevent strain from being read by the sensor. However, if the freezing point of the adhesive used to attach the fibre to the copper disc was in the range of $30-300$ K, a finite amount of strain would be transferred to the sensor.

Flux-pinning-induced strain in a YBCO disc during FC and ZFC magnetization cycles was measured over the disc surface as a function of disc radius and magnetic field with six FBG sensors inscribed in a single fibre at 60 K [57]. This study is of great significance from an applied and practical point of view because it widens our understanding on mechanical stresses in bulk superconductors for levitation, and bulk superconducting magnet applications. The experimental results were

compared with simulations and the reasons for large discrepancies were discussed. However, the impact of vacuum chamber deflection on strain has been neglected as a potential source of discrepancy.

Despite being used in many superconducting applications, FBG sensors have not been employed in actual SMB environments. In practical SMBs, measuring the temperature of the HTS assembly surface facing the rotating PM structure is challenging with conventional sensors. Apart from usually limited mounting space, electromagnetic interference can seriously influence the output signal of electronic sensors. Poor thermal insulation of electronic sensors is another issue when using them in SMBs. Multi-point temperature and/or strain sensing is also not trivial due to the limited mounting space. All these issues, however, might be solved by appropriately introducing FBG sensors to SMB environments. Considering the impact of temperature on decay behaviour in HTS bulks, FBG sensors seem to be useful tools to monitor HTS bulk temperature in relaxation studies.

2.8 Rotational Loss

The contactless rotation of a PM above a superconductor bulk in vacuum seems to be lossless, however, this is not the case. The loss mechanism in SMBs is rather complicated, which has been investigated by many researchers [4, 58–66].

The rotational loss in SMBs is mostly due to the azimuthal inhomogeneity of the PM magnetic field [58, 67, 68]. It has been said that the rotational loss has two main components; hysteresis loss and eddy current loss. The former, which arises from flux pinning inside the superconductor, is considered as frequency independent [69]. However, some researchers claimed that there would be a small frequency dependence in hysteresis loss [4]. The latter can be created in all electrically conducting parts which are subjected to an AC magnetic field from either a rotating PM or an inhomogeneous HTS magnetization. In a bearing with a simple structure where a PM disc rotates above an HTS disc, if the PM magnetic field is inhomogeneous in the azimuthal direction, the HTS disc and all surrounding conductors see an AC field which induces eddy currents. The HTS trapped magnetic field may also be inhomogeneous, due to either the discrete structure of the HTS bulks arrangement or the inhomogeneous shielding current of a single HTS bulk, which induces eddy currents in rotating conductors such as PM rotor [70, 71].

In 1983, Wilson formulated hysteresis generated in a superconducting slab and a long superconducting disc in a varying magnetic field [72]. Afterwards, many

researchers developed this formula and utilized different methods to simulate and calculate the hysteresis loss [58, 60, 73, 74].

Weinberger *et al.* [75] presented the coefficient of friction (COF) as a parameter to calculate the rotational loss, and as a figure of merit to compare different types of SMBs. Afterwards, the COF, which is obtained from spin-down tests, has been used by other researchers as a reliable tool when studying rotational loss in HTS bearings [59, 61, 62, 76–80].

The main challenge in performing spin-down tests in SMBs is to engineer a driving system to accelerate and decelerate the levitating PM. Gas jets [58, 81], electrical motors [58, 63, 69, 82], a 3-phase handmade brushless motor [64, 83], eddy current clutches [61, 63, 84–87], and magnetic gears [88] have been employed to accelerate the rotating part of superconducting bearings. These methods are associated with complex coupling structures, loss creation, limited maximum speed, and lack of precision when it comes to speed control.

Trentiev *et al.* [70] performed an experiment to investigate the AC loss mechanism by measuring the quality factor of an oscillator. This factor determines how damped the system is. They attached a PM to an oscillator and made it resonate near the surface of an HTS disc. In order to investigate the contribution of eddy current loss to the total dissipation, they used a non-conductive PM and found that the total loss showed almost cubic dependence on the magnetic field inhomogeneity. This dependence changed to a square law when they attached a thin copper disc to the PM. This result shows the AC magnetic field experienced by the copper disc can also be seen by the PM. They reported, at low frequencies, the hysteresis loss is the main component of the total dissipation in a superconducting bearing which means the total loss is almost proportional to the third power of magnetic field inhomogeneity ($W = \frac{2\mu_0 H_{ac}^3}{3J_c d}$) which was consistent with Wilson's equation. The authors also reported that in cases where the bearing rotates at the speed of a few kHz, the eddy current loss in the conducting PM becomes dominant as it is dependent on frequency. This implies that the AC loss would be almost proportional to the second power of the magnetic field inhomogeneity. In this paper, two magnets are used in the oscillator; one facing the YBCO bulk, and the other one facing the resonator coil. These two magnets are attached together on a cantilever beam. the impact of the resonator magnet on the magnetic field profile of the levitation magnet has not been discussed. Moreover, the YBCO bulks used in these experiments were multi-grain, which may add to the inhomogeneity of the trapped field in the YBCO bulk, and hence, may change the AC loss behaviour. The authors have assumed the main source of eddy current loss is the conductive

PM. Although eddy currents are induced in all conductive parts, study shows [89] that the eddy current loss mechanism appears in HTS bulk at frequencies much lower than it appears in conductive magnets.

Kordyuk *et al.* [90, 91] investigated the AC loss mechanism in a PM-HTS configuration with the non-contact resonance oscillation technique. They measured the quality factor with respect to the amplitude of vibrations with the assumption that the AC field is a linear function of vibration amplitude. They showed that the Q^{-1} factor has a linear relation with the amplitude $(\alpha + \beta A)$, so the formula for energy loss would be: $W = \alpha A^2 + \beta A^3$, where α and β are constants and A is the amplitude of vibrations. This says that energy loss has two components, hysteresis and viscous. They have mentioned that the viscous part (the first term in the equation) is frequency dependent, but, no frequency analysis was reported in the paper. The amplitude dependence of AC loss can change with frequency from quadratic at kHz frequencies to cubic at low frequencies. The equation they proposed for AC loss seems to be a superposition of both regimes, which requires further detail about their experimental frequency.

A group of scientists [92] proposed a formula to model the magnetic field inhomogeneity of a PM and then performed simulations to model the relation between inhomogeneity and rotational loss. According to their simulations, rotational loss is proportional to the second power of the ratio of magnetic field inhomogeneity to the mean value of magnetic field. In this paper, the authors mention using liquid nitrogen, but, no temperature dependent analysis was performed or presented. The inhomogeneous magnetic field was defined as an AC component by a sinusoidal function, which does not represent a real inhomogeneous PM. Simulations were performed at the rotational speed of 600 rpm with and without the effect of s stainless steel cryostat. The contribution of the conductive cryostat was presented for a single rotational speed, but a frequency sweep analysis would have been helpful, since the origin of loss in a conductive cryostat is strongly frequency dependent. In another paper [93], they have mentioned that the rotational loss is proportional to f^2B^2, where f is frequency and B is field amplitude. They have considered eddy current loss in conductive rotor as the main component of the rotational loss. In this paper, authors have suggested an optimal arrangement for HTS bulks in order to reduce the inhomogeneity of the magnetic field trapped in an arrangement of bulks. However, they have completely ignored the impact of rearrangement on hysteresis loss as the main component of rotational loss at low frequencies.

Simulations have been conducted to examine the rotational loss reduction ideas. According to the literature, there are ideas to reduce the eddy current loss in rotating

parts, to enhance the homogeneity of the trapped magnetic field in the HTS bulks, and to enhance the azimuthal homogeneity of the levitation PMs [60, 66, 93, 94].

Ferromagnetic shims were used to reduce the inhomogeneity of a PM [60]. Spin-down experiments showed that the low-velocity COF was improved for the shimmed PM, but, the high-speed COF remained unchanged. In this paper a figure of merit, ϕ, for PM was defined as:

$$\phi = \sum_{r} \sum_{\theta_{i=0,2\pi}} [\Delta B_z(r, \theta_i)]^3 \tag{2.3}$$

which is indicative of its expected hysteresis loss. Here, r is the radius and θ is the azimuthal angle. In equation 2.3, ΔB_z is defined as:

$$\Delta B_z(r, \theta) = \left| B_z(r, \theta)|_{max} - B_z(r, \theta)|_{min} \right| \tag{2.4}$$

The authors have reported an improvement of a factor of ≈ 3 in ϕ after shimming. However, the periodicity of B_z in a 2π rotation has been factored out in equation 2.4. This periodicity can affect both hysteresis and eddy current losses.

Masaie *et al.* [95] simulated the influence of superconductor bulk shapes on the levitation force and the rotational loss. However, they did not validate their simulations by experimental results. They proposed three shapes for the HTS bulks used in a SMB for a flywheel energy storage system. According to the authors, changing the shape of the HTS bulks can reduce the rotational loss by 50 %.

In another paper focusing on the rotational loss of a SMB [66], Koshizuka investigated the impact of changing the HTS bulks shape on the rotational loss of a 100 kWh flywheel energy storage system. He mentioned the rotational loss can be decreased by taking this measure. Moreover, he investigated the eddy current loss in the PMs, and proposed that laminating the PMs can reduce the eddy current loss. In fact, it has not been clarified whether the reduction of the rotational loss is due to reduction of the eddy currents in the PM or is due to the change in magnetic field distribution after laminating. It could be better if the author had mapped the magnetic field of the PM before and after laminating. Moreover, the contribution of the eddy current loss in the PM to the total rotational loss is not determined.

The Boeing group [84] investigated the impact of cooling methods on the rotational loss in a superconducting flywheel energy storage system. A liquid nitrogen bath and conducting copper bars connected to a coldhead were used as two different cooling systems. The authors concluded that the eddy current loss is mainly created in the rotor structure, but they have not clarified the origin of eddy current loss in the rotor structure. The spin-down measurement results

presented in the paper are very difficult to compare, since the experiments were performed at different temperatures, air gaps, and with different rotor releasing mechanisms. Furthermore, the impact of temperature on eddy current loss was only taken into account for conducting copper bars, and was neglected for the magnetic field trapped in the HTS bulks.

One the most important advantages of superconducting bearings over conventional bearings is removing the speed limit in rotary machines. Hence, researchers have studied high-speed performance and loss mechanism of superconducting bearings.

A high-speed superconducting bearing prototype was built and its drag torque was studied by Moon [83] where the drag mechanism was attributed to the magnetic field inhomogeneity of levitation PM and was said to be independent of rotational frequency. However, several studies showed the frequency dependence later.

Hull *et al.* [64] performed spin-down experiments on a superconducting bearing configuration similar to the system described in [83] and discussed the frequency dependent term appearing in the deceleration curve. They described the frequency dependent term as a result of pushing HTS bulks into the flux flow regime. This dependency was believed to be governed by skin depth at high frequencies, which was in agreement with AC susceptibility measurements performed on superconductors [89, 96]. At high frequencies, when the rotational loss is governed by skin depth, the shielding currents flow in a narrow region near the circumference of the bulk. Because of material inhomogeneities and finite thermal conductivity of YBCO, maintaining an isothermal condition is of great significance. In this study, however, the YBCO bulks were cooled by a conduction cooling method with their back surface (not facing the levitation magnets) attached to copper bars. Although in this configuration conductive parts such as copper bars are separated from magnets, the HTS region where the shielding currents flow is not in direct contact with cold copper. In the flux flow regime, currents induced in the HTS bulk are greater than J_c and dissipate heat, which must be removed from the bulk before it disrupts isothermal condition of the experiment. Heat management in the driving coils is also important, as these coils operate in a vacuum chamber. Despite successful operation, no explanation was given about the driving system heat management.

The key points of AC loss studies can be outlined as follows:

- AC loss (rotational loss) in SMBs is mainly created by magnetic field inhomogeneity.
- AC loss in SMBs is evaluated by performing spin-down measurements.

- COF has been used as a figure of merit to characterise the deceleration rate of SMBs.
- AC loss in SMBs has two main components, namely hysteresis loss and eddy current loss.
- AC loss is mainly dominated by hysteresis loss at low rotational frequencies, but dominated by eddy current loss at high rotational frequencies.
- Hysteresis loss is intrinsic to HTS material, whereas eddy current loss can occur in all conducting parts in an SMB.
- Hysteresis loss is said to be independent of rotational frequency, whereas eddy current loss is dependent on rotational frequency.
- Hysteresis loss has been formulated based on Bean's critical state model. However, the periodicity of the magnetic field in a complete rotation in an actual SMB has not been taken into account in that formulation.
- AC loss studies lack experimental evaluation of the relationship between magnetic field inhomogeneity and AC loss in an actual SMB environment.
- Simulations show that AC loss is dependent on the shape of the HTS assembly in SMBs, because the field trapped in the HTS assembly is changed by the shape of the bulks.
- kHz-rated spin-down experiments show that HTS bulks may be driven into resistive flux-flow regime.

2.9 Summary

According to Earnshaw's theorem, PM-PM systems are unstable. introducing HTS materials can make them stable. Passively stable superconducting magnetic levitation can be achieved by type-II superconductors in mixed state, where the levitation force is provided by the diamagnetic response of the superconductor and passive stability is provided by flux pinning feature of type-II superconductors. This feature of superconductors has attracted much attention resulting in the design and construction of SMBs. However, before manufacturing SMBs, their behaviour should be simulated and predicted. Several numerical and analytical models have been proposed, among which finite element models have been widely developed. In this thesis, the H-formulation developed by Queval *et al.* [31] is adopted and

will be modified to model and simulate the electromagnetic behaviour of SMB, because of its flexibility and capability to simulate different HTS structures in 2D and 3D configurations. Moreover, detailed experimental results are provided to validate simulation results, which makes this model reliable.

The levitation force decays logarithmically due to thermally activated flux creep in HTS bulks. The decay amplitude and rate depends on several parameters such as temperature, the initial cooling condition, the variation of the external magnetic field, and the vibration around the operating point. There are also several ways, such as preloading and cooling, to suppress the force decay. The magnetic relaxation in type-II superconductors is related to their E-J relationship. Levitation force decay can be related to the non-linear E-J power law, and creep exponent n can be extracted from levitation force decay measurements. However, experiments assessing this hypothesis have not been reported elsewhere.

Although providing cryogenic temperatures for HTSs is no longer a major challenge, maintaining an isothermal operating condition is crucial for practical applications. This requires precise and reliable temperature monitoring and controlling. In some applications of bulk superconductors such as superconducting magnets, flux-pinning-induced tensile stresses can cause micro-cracks or can break a single large superconducting bulk into some smaller domains. In order to avoid such breaks, the mechanical stress on superconducting bulks must be monitored. For both strain and temperature measurement, there are several electronic sensors available on the market, but the main problem with these sensors for high-field superconducting applications (such as superconducting bearings) or for applications with high magnetic field variation (such as superconducting bearings, and maglev) is electromagnetic interference and poor thermal insulation. Optical FBG sensors, however, are not affected by electromagnetic fields and offer an acceptable thermal insulation. These sensors have been studied widely for applied superconductivity projects. One of the important parameters in SMBs is the temperature of the HTS bulk surface facing the levitation PM. Conventional temperature sensors do not seem practical in bearing projects where the air gap between HTS stator and PM rotor is of a few millimeters and sensor is subjected to a varying magnetic field. Monitoring magnetostrictive behaviour of HTS stator in a real SMB system can also widen our understanding about the mechanical properties of HTS bulks. Up to the date of writing this thesis, FBG sensors have not been used in a SMB.

Rotational loss, also known as AC loss, is a significant property in SMBs which affects the performance of the bearing system. Spin-down tests have been widely performed to measure rotational loss. Magnetic field inhomogeneity is said to be the

primary source of AC loss in SMBs, which can create hysteresis loss in HTS bulks and eddy current loss in all conductive parts, including HTS bulks. Several measures such as changing the HTS bulk shape, and cooling methods have been proposed to reduce the AC loss. But the contribution of the magnetic field inhomogeneity to the AC loss components, and the extent to which these measures can mitigate the AC loss components is not clear. According to Bean critical state model, AC loss has been formulated as a cubic function of magnetic field inhomogeneity. However, this model has factored out the impact of magnetic field periodicity and the distribution of AC loss over the surface of the bearing. Furthermore, by the time of writing this thesis, there was no experimental evaluation of the inhomogeneity-AC loss relationship in an actual SMB environment. High-speed superconducting bearings have also been built and studied. But the loss mechanism in superconducting bearings at kHz-rated rotational frequencies has not been fully studied. As one of the major advantages of SMBs is overcoming speed limits imposed by mechanical bearings, building and studying a high-speed motor/generator prototype can contribute to the understanding of high-speed loss mechanisms and can help develop our capability of employing these bearings for practical applications.

The key findings of this chapter can be summarized as follows:

- Type-II superconductors in the mixed state can provide passive stable levitation/suspension:
  - Levitation/suspension is provided by the diamagnetic response of type-II superconductors.
  - Stability is provided by flux pinning.
- H-formulation is adopted and will be modified to model and simulate the electromagnetic behaviour of SMBs, because of its flexibility and reliability.
- Levitation force decay can be related to the non-linear E-J power law.
  - Creep exponent, n, can be extracted non-destructively from decay experiments.
  - This is of great importance for HTS bulk simulations.
- Precise and reliable temperature monitoring is crucial for maintaining an isothermal condition in practical SMB applications.
  - In conduction-cooled applications, the temperature of the HTS surface may be different to the temperature of coldhead.

  - It is difficult to monitor the temperature of HTS bulk surface with electronic sensors, due to limited space, thermal insulation, and electromagnetic interference.
  - FBG sensors seem to be a potential solution for temperature monitoring at the bearing surface.

- AC loss is mainly caused by magnetic field inhomogeneity in SMBs.
  - It is measured in spin-down experiments.
  - It has two components; hysteresis and eddy current loss.
  - Hysteresis loss has been formulated based on Bean model.
  - Magnetic field periodicity in one rotation and the distribution of AC loss over bearing surface have not been considered in that formulation.
  - AC loss mechanism at kHz-rated rotational frequencies has not been fully explored.
  - At kHz-rated rotational frequencies, HTS bulk is pushed into resistive flux-flow regime.

In the past two chapters the motivation for writing this thesis, the research questions to study, as well as a review of the work done were presented. Having known the questions, the next step is to employ the methods required to answer the questions. Some of these methods were already designed and were already available, whereas some other methods were designed and built during the course of this thesis. A detailed report of these methods will be provided in the next chapter.

3 Methodology

3.1 Introduction

Elaborated in this chapter are the basic methods used to design and build experimental setups and to simulate electromagnetic behaviour of high-temperature superconductor bearings. In total, five experimental setups, which were used to perform the experiments reported in this thesis, are described in this chapter.

Two experimental setups were used to study levitation force decay and its relationship with flux creep exponent, n-index, in HTS bulks. In one setup a liquid nitrogen cryostat was used, but in the other one a dry cryo-cooled coldhead was employed.

In order to study AC losses in SMBs, two further experimental rigs were designed and built. In the first rig, the relationship between AC losses and magnetic field inhomogeneity is studied in a thrust bearing, where the axis of rotation is parallel to the levitation force axis. In this rig a novel coupling mechanism is designed, built, and tested at rotational speeds up to 10000 rpm. The second rig was designed and built to prove the principle of SMB application in a laboratory-scale high-speed motor/generator prototype. Furthermore, this rig allowed AC losses to be studied at kHz-rated frequencies in SMBs.

An additional experimental setup was used to map and characterise the magnetic field of permanent magnets used in AC loss studies. This experimental setup, alongside AC loss setups, is essential for exploring the relationship between AC losses and magnetic field profiles. This rig will also be required for practical SMB applications, where magnets with the least contribution to AC losses should be selected.

The corresponding results and further explanations about the basic physics, experimental setups, and experiment procedures will be presented in the subsequent chapters separately.

3.2 FE modelling

The PM-HTS interaction was simulated in *COMSOL Multiphysics* [97]. The H-formulation method presented in [98] and developed by Queval *et al.* [99] was

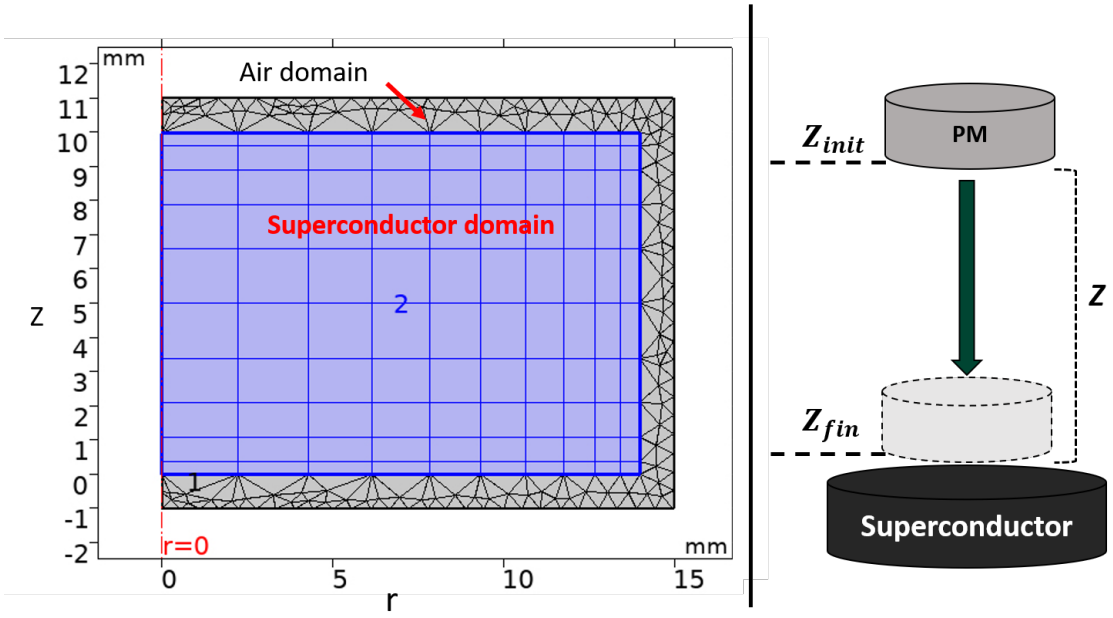

Figure 3.1: Left: the 2-D axisymmetric meshing of the superconductor (blue) and thin air (gray) domains. The enclosing air region is 1 mm larger in either direction. Right: the movement scenario depicted by the arrow.

adopted. This method has been independently verified by our group [100]. Here, the applied magnetic field from a stationary PM is calculated from the A-formulation and exported to a look-up table. The time dependence of the external magnetic field $\boldsymbol{H}(x, y, z)$ is taken into account by shifting the stored $\boldsymbol{H}(x, y, z)$ within the spatial frame. The total magnetic field, which is the sum of the external magnetic field from the PM ($\mathbf{H}_{ext}$) and the self-field from the superconductor domain ($\mathbf{H}_{self}$) is applied as a Dirichlet boundary condition to the boundaries of a thin air region enclosing the superconductor. The non-linear resistivity of the superconductor is given by [100]:

$$\rho = \frac{\rho_{NS} \cdot \rho_{SC}(\mathbf{J})}{\rho_{NS} + \rho_{SC}(\mathbf{J})} \tag{3.1}$$

where, $\rho_{NS} = 3.5 \times 10^{-6}\ \Omega$.m is the normal state resistivity [100], and $\rho_{sc}(J)$ is superconductor resistivity defined as [100]:

$$\rho_{sc}(\mathbf{J}) = \frac{E_c}{J_c}\left|\frac{\mathbf{J}}{J_c}\right|^{n-1} \tag{3.2}$$

$\boldsymbol{J}$ is the current density inside the superconductor, and J_c is the critical current density at the electric field criterion $E_c = 10^{-4}$ V/m. For simplicity, J_c is taken to be field-independent and spatially homogeneous. Mapped and free triangular meshes were applied to superconductor and air domains, respectively (figure 3.1).

Simulations were performed in a 2D-axisymmetric geometry with the relative tolerance of 10^{-3} for A-formulation and 10^{-4} for H-formulation [99]. The levitation force along the z-axis is calculated from:

$$\mathbf{F} = \int_v \mathbf{J} \times \mathbf{B} \, dv \tag{3.3}$$

where the integral is performed over the volume of the superconductor. The displacement Z represents the vertical distance between the PM and superconductor (figure 3.1). In the simulations, the PM remanent flux density was 1.32 T, and the stored magnetic field was shifted from $Z = Z_{init}$ to $Z = Z_{fin}$ at various velocities.

3.3 Magnetic Field Mapping

Studying AC loss mechanisms in SMBs requires comprehensive study of the applied magnetic field profiles. Considering the rotation of the levitated magnet around its axis of symmetry in an SMB, magnetic field profiles in the azimuthal direction need to be characterised. In order to achieve this, a benchtop setup (figure 3.2) was designed and built. The magnetic field was measured by a P15A Hall sensor supplied by *AHS* [101]. The Hall sensor was driven by a *Keithley* 2400-c sourcemeter [102] at 1 mA, and was read by a *NI USB*-6009 card supplied by *National Instruments* [103]. The sensor is mounted on the tip of a cylinder made of G10. The 3D motion (along x, y, and z axes) with a resolution of 0.05 mm is realized by linear stages. Two linear stages work in parallel along the x-axis. A rotary table for rotating an object beneath the sensor with the resolution of 1.8°, gives a fourth axis around which the table rotates. PMs of different sizes can be installed on the center of the rotary table. The sensor mount and PM are aligned axially with an accuracy of 10 μm. The rotary table and all linear stages are controlled by an MC 405 controller supplied by *TrioMotion* [104]. There are some limitations in this setup. Mounting the Hall sensor parallel to the G10 cylinder surface and PM surface was challenging. In order to keep the sensor level on the tip of the G10 cylinder, a thin PCB circuit was used on top of the sensor, which increased the minimum distance between the sensor and the top surface of PM to 2.6 mm.

3.4 Force Decay Characterisation Setup: Liquid Nitrogen Cryostat (Tinius Olsen rig)

An experimental test rig was designed and built to measure levitation force decay in a superconducting thrust bearing. The superconducting bearing consists of a

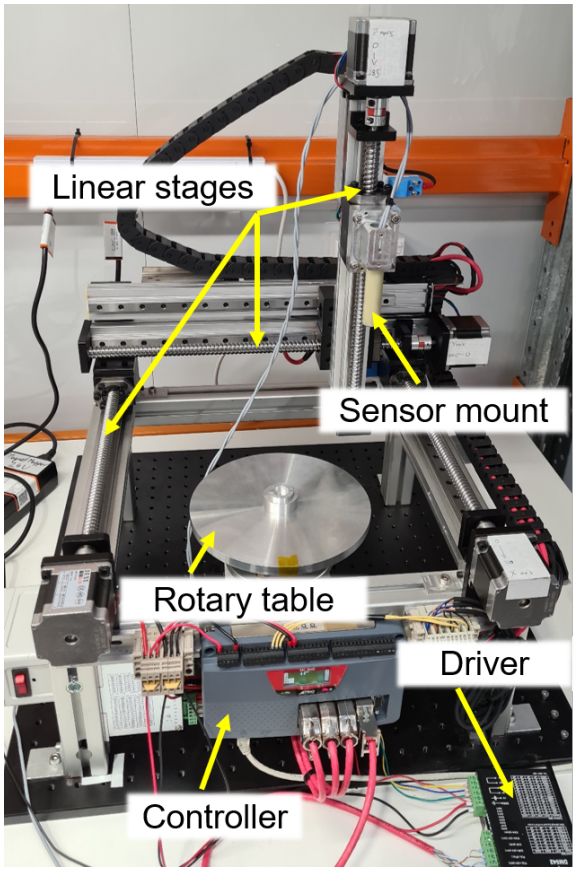

Figure 3.2: Photo of the magnetic field mapping setup. This setup was used to measure the magnetic field of PMs around their circumference.

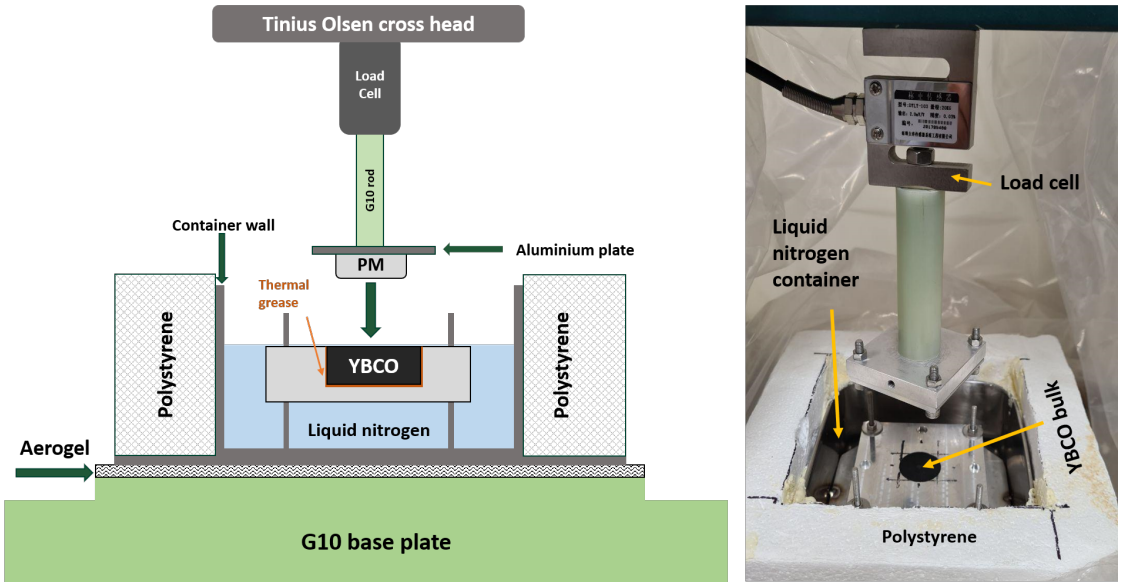

Figure 3.3: Schematic (left) and photo (right) of the experimental test rig showing the cryogen level. Note that the liquid nitrogen at no point exceeds covering the YBCO bulk and is never in direct fluid contact with the PM

20 mm diameter, 12 mm thick cylindrical N45-grade *NdFeB* PM, and a cylindrical superconducting bulk 28 mm in diameter and 10 mm thick. The bulk is melt-textured $YBa_2Cu_3O_{7-\delta}$, capable of trapping magnetic field up to 0.9 T at 77 K, and was provided by *CAN Superconductors* [105]. The superconducting bulk was fully recessed into an aluminium plate to provide a stable thermally conductive mount for the bulk. A thin layer of thermal grease was used to enhance thermal contact between the disc and the plate. The aluminium plate was placed inside a stainless steel container and fixed by bolts welded to the container bottom surface. The container was mounted on a G10 plate. The container side walls and bottom surface were thermally insulated using polystyrene pieces and Aerogel, respectively. The entire assembly was fixed with bolts to a larger G10 base plate. Liquid nitrogen was used as a cryogen to provide isothermal conditions, and no temperature controller was in operation in this experimental rig. The schematic and picture of the assembly is shown in figure 3.3.

The displacement was provided by a *Tinius Olsen* H10KT machine [106], whose crosshead can move vertically at velocities ranging from 0.001 mm/min to 1000 mm/min. This machine was controlled by *LabVIEW* software [107]. As the levitation force was predicted to be smaller than 100 N, an s-type loadcell with a range of ±20 kg was attached to the crosshead of the machine. The PM was bonded to an aluminium plate with a two-part epoxy [108]. A 40 mm long G10 rod was mounted between the PM and the loadcell to provide thermal insulation between the loadcell and cryogenic environment. The entire test setup was covered by a plastic bag to provide a positive pressure volume created by nitrogen gas inside the bag. This minimizes airflow inside the cryogenic environment and prevents ice formation on cold surfaces.

In this experiment, the YBCO bulk was cooled down to the boiling temperature of liquid nitrogen, 77 K, with the PM far enough to achieve a ZFC condition. The displacement, Z, represents the vertical distance between the bottom surface of the PM and the top surface of the superconductor. The vertical (Z) axis of the PM and the YBCO bulk were aligned to minimize undesirable lateral forces during levitation force measurement. After reaching an isothermal cryogenic condition and performing a zeroing of the load cell, the PM which was initially at a displacement of Z = 60 mm, was moved downwards to a minimum displacement of Z = 1 mm at a velocity of 1 mm/s, then held at that position until the first derivative of the normalized force fell below the noise level of the loadcell, which for this rig was almost 1.6×10^{-4} N. This criterion confirms that the levitation force has reached a steady-state level. This process was repeated for minimum displacements of Z = 2 mm and Z = 3 mm.

During each movement, the levitation force and PM position were measured at an acquisition rate of 10 Hz. After each measurement, the superconductor was warmed above its critical temperature to remove any trapped flux [100, 109, 110].

3.5 Force Decay Characterisation Setup: Dry Cold Head

Another experimental setup was designed and built to measure levitation force decay from cryo-cooled bulks in a vacuum chamber [111]. Two SMBs were studied in this experimental rig. The first consists of a disc-shaped HTS bulk and a disc-shaped PM identical to the SMB described in section 3.4. The second consists of a conical frustum-shaped N50-grade *NdFeB* PM, supplied by *SuperMagnetMan* [112], and an HTS assembly including a trapezoidal toroid, inside which a small disc is placed. The entire HTS assembly is melt-textured $YBa_2Cu_3O_{7-\delta}$ and was provided by *Can Superconductors* [113]. The HTS assembly is fixed to an aluminium plate by clamping it to avoid movement due to electromagnetic interaction with PM. Vacuum grease is used to enhance thermal contact between the toroid and the clamp.

Another aluminium plate is directly mounted on the cold head of a *Cryomech AL63* cryocooler. The HTS part of both SMB configurations is mounted on this aluminium plate. The wider (top) surface of the PMs is bonded to an aluminium plate, which is mounted to a 3-axis *Galoce* load cell sensor model $GPB161$ with a measurement range of ±500 N [114]. This load sensor is mounted on a linear movement system realizing lateral and vertical displacement which is controlled by *TrioMotion MC464*, a *National Instruments Compact DAQ hardware*, and *LabVIEW* software. Two linear variable differential transformers (LVDTs) model *DC-EC 500 ASSY* with a full stroke range of ± $12.7mm$ are used to measure linear displacement [115]. The configuration and dimensions of the HTS assembly and PM in both configurations are shown in figure 3.4. Figure 3.5 illustrates the experimental test arrangement.

Temperature measurement is carried out using XP-100 platinum [116] and *S950-SM* silicon diode [117] cryogenic thermal sensors. In order to measure the toroid temperature, a small slot is cut onto the clamp and a XP-100 sensor is bonded to the shaved side of the toroid through that slot. A thin layer of thermal grease is applied to improve the thermal contact between the XP-100 and toroid. The XP-100 is retained using a zip tie which applies more pressure and enhances the contact between the sensor and toroid. Two XP-100s are also used to measure the temperature of aluminium plates to which the HTS assembly and the PM are

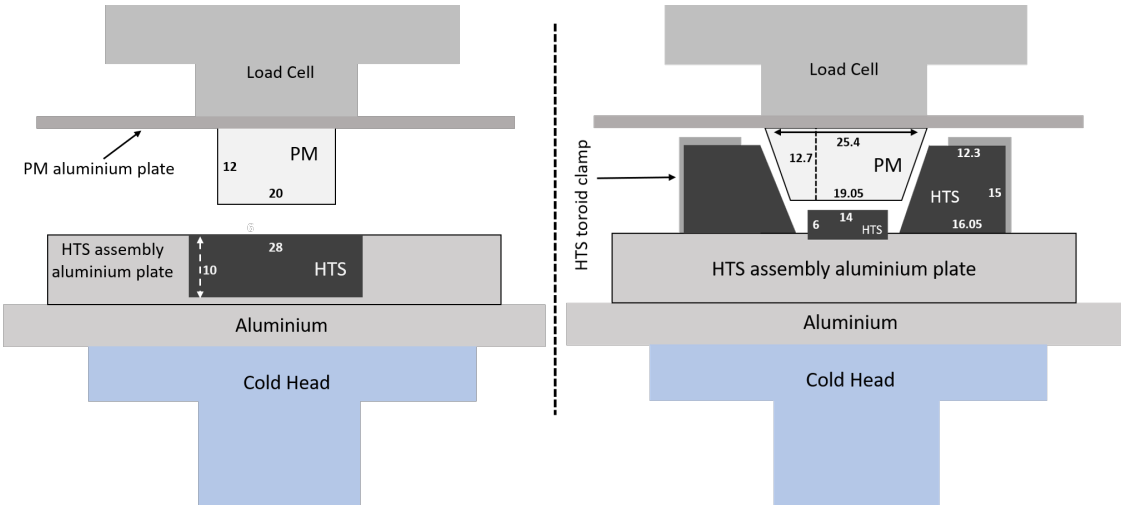

Figure 3.4: Cross-sectional view of the studied SMB configurations. Dimensions are in mm.

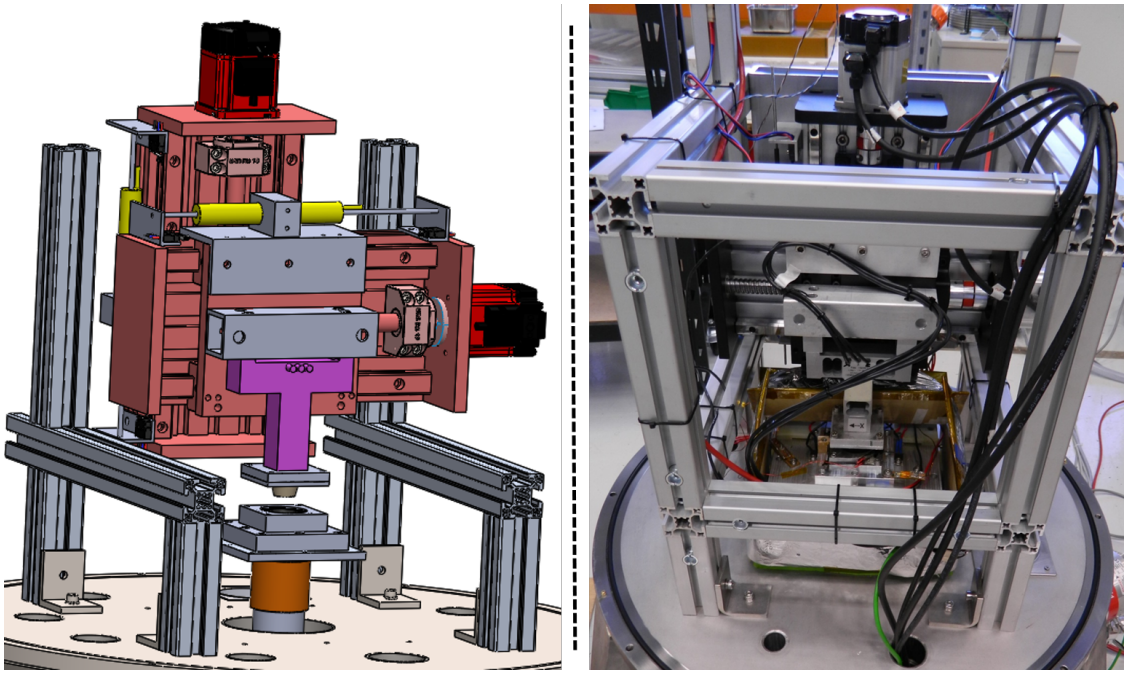

Figure 3.5: Drawing and photo of the test rig with the toroid-shaped HTS assembly and frustum-shaped PM, showing the load cell sensor (purple), displacement sensors (yellow) and translational stage and motors (red). Some parts have been removed from drawing for clarity.

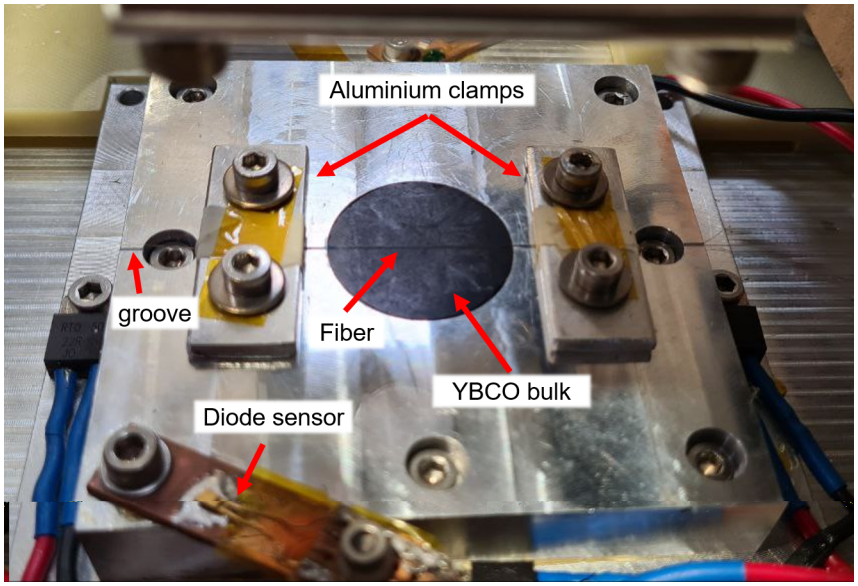

Figure 3.6: Photo of the disc-shaped HTS bulk with the FBG sensor installed on top of it.

attached. In addition, a diode sensor is mounted on the aluminium plate which is in direct contact with the cryocooler cold head. A 4-channel *Cryocon*-26 temperature controller [118] capable of operating from 500 mK to 1500 K, and in proportional (P), proportional-integral (PI), and proportional–integral–derivative (PID) modes is used to control the temperature. Four 50 W heater resistors are controlled by the controller. The XP-100 attached on the toroid side and the diode sensor provide feedback signal in the trapezoidal toroid SMB and disc-shaped SMB, respectively. The HTS assembly temperature can be stabilized from 42 K to 90 K in both configurations. XP-100s were calibrated by reading the diode sensor output as the reference temperature and matching them with the PT100 resistance at the same time, during warming up from 40 K to room temperature. The warming process is more gradual, and therefore any thermal gradients will be suppressed and the setup is more likely to be isothermal. This results in a more accurate calibration.

The entire setup is housed inside a turbo-pumped vacuum chamber, capable of reaching the pressure of 10^{-3} hPa.

3.6 Temperature and Strain Measurement with FBG Sensors

FBG sensors have not been employed in actual SMB environments. In practical SMBs, measuring the temperature of the HTS surface facing the rotating PM is challenging with conventional sensors due to electromagnetic interference, limited

mounting space, and poor thermal insulation. Employing FBG sensors in SMB environments, however, can address these issues.

In order to attempt to measure the temperature at the top surface (facing the PM) of the HTS bulk in the disc-shaped SMB configuration, a germanium doped, single mode silica fibre, manufactured by *FBGS Technologies* using Draw Tower Gratings (DTG ®) was employed [119]. The fibre is Ormocer coated [120] with a diameter of 170 μm. The fibre contains one FBG whose reflection spectrum is centered at 1540 nm. A V-shaped groove was machined on the aluminium plate to hold the fibre on the HTS bulk center line. The groove cross section is an equilateral triangle with side length of 0.9 mm. A thin layer of *Apiezon N* grease [121, 122] was applied between the FBG and the bulk to maintain a consistent contact between the fibre and the bulk. The fibre was sleeved into a PTFE tube (ID of 0.305 mm, OD of 0.762 mm) and was retained using aluminium clamps installed at either side of the HTS bulk. A thin layer of latex was used between the clamps and the fibre to prevent damage. Extra care should be taken when tightening the clamps to avoid three-point bending caused by levitation force. Figure 3.6 shows the experimental setup.

3.7 Dynamic Measurement rig: Vertical Configuration

The SMB in this rig is a thrust bearing that consists of a disc-shaped PM and a disc-shaped HTS bulk supplied by *Magnets NZ* [123] and *Can Superconductors* [105], respectively. In general, this rig consists of three main parts, namely the driving system, vacuum chamber and cooling system, and sensors and measurement devices.

3.7.1 Driving System

The main challenge in this rig was to spin up the PM, release it, then capture it again. Figures 3.7b and 3.7c show the schematic and a photo of the driving system in this rig. A high-speed brushless direct current (BLDC) motor, whose characteristics are shown in table 3.1, is used to spin the PM. The motor is model *ECXSP22L BL KL A STEC 48V* supplied by *MaxonMotor* [124]. This motor is controlled by a built-in Maxon controller and software. Because the motor operates in vacuum where heat dissipation through convection is not possible, the motor is encased in an aluminium heat sink to cool it. This heat sink with the motor inside is mounted on a vertical linear displacement stage.

A power transmission mechanism consisting of two main parts was designed and built to transfer power from the motor shaft which is 4 mm in diameter to

Table 3.1: Motor Parameters

Parameter	Value
Nominal voltage	48 V
No load speed	57300 rpm
No load current	263 mA
Nominal speed	55500 rpm
Nominal torque (max. continuous torque)	25.5 mNm
Nominal current (max. continuous current)	3.42 A
Max. efficiency	91.6%

the PM which is 17 mm in diameter. The first part includes the male side of the PM coupling. This part is a hollow cylinder inside which the PM is bonded. The male part is made of acetal (polyoxymethylene) because it is a high strength, low friction, and easy-to-machine engineering plastic. Moreover, it prevents eddy currents from being induced in the male part by the magnetic field trapped in the HTS bulk. The ID and OD of the cylinder are 18 mm and 30 mm, respectively. The top surface of the cylinder is machined to form a P4C-like polygon based on DIN 32712 (see figure 3.7b). At the upper edge of the polygon a chamfer with the aspect ratio of 1 : 1, and dimensions of 3 mm $\times$ 45° is machined. This chamfer helps self-centring during coupling and decoupling processes. These characteristics are chosen due to machining equipment limitations. The second part consists of a 65 mm long aluminium shaft. The bottom surface of the shaft is a cut-through P4C-like polygon with the same chamfer characteristics as that of the male part and serves as the female side of the PM coupling. The upper part of the shaft is a jaw-type coupling and connects the aluminium shaft to the motor shaft. The aluminium shaft is fixed and supported by two ceramic ball bearings embedded at two ends of an aluminium box. This box improves the bearing's axial alignment and enhances heat dissipation. The shaft is made of aluminium because it is lightweight and easy to machine. Moreover, since it is not ferromagnetic, it does not interact with the PM and the motor.

A shielding box made of polycarbonate is used to protect sensitive parts like sensors from being hit by the PM during an unexpected unstable rotation. This material can absorb high kinetic energy without breaking. Moreover, the material

is cheap, easy to machine, and transparent which allows monitoring the rotation process. This box covers the PM, coupling systems, and the HTS bulk.

A thin aluminium spacer mounted on a vertical linear displacement stage, is provided to adjust the cooling height of the PM above the HTS bulk surface. This spacer together with the linear stage are mounted on another lateral linear stage, which can move the spacer aside after reaching the desired temperature. All linear stages are controlled by an Arduino-based controller.

3.7.2 Vacuum Chamber and Cooling System

The whole test setup is housed inside a cylindrical stainless steel vacuum chamber, which is 600 mm in both diameter and length. Two windows are machined on the side wall of the chamber, allowing non-vacuum-rated displacement sensors to be installed outside the vacuum environment. The base plate of the chamber allows the cold head of the cryocooler and electronic connections to be fed through (figure 3.7a).

A two-stage *Edwards T-Station 85*[125] is used to evacuate the chamber. The *Edwards T-Station 85* seamlessly combines an *nEXT85H* turbomolecular pump with a dry diaphragm backing pump (*XDD1*) and a simple controller. This system is capable of providing vacuum to below 1×10^{-6} mbar, thereby ensuring the stability of the cryogenic environment.

The HTS bulk is a melt-textured $YBa_2Cu_3O_{7-\delta}$ disc [105] and is 28 mm in diameter and 10 mm in thickness. The HTS disc which forms the stator part of the SMB is partially recessed into a copper plate mounted on the *Coolstar 0/40* cold head of a GM cryocooler supplied by *Oxford Cryosystems* [126].

3.7.3 Sensors and Measurement Devices

In this test rig we are interested in measuring the vibrations of the PM during spin-down measurements especially when it passes through its resonance frequencies. For this purpose a *Keyence IB-30* laser displacement sensor [127] is employed. A *Monarch Instrument* remote optical sensor model *ROS-W* [128] mounted on the setup frame measures the rotational frequency of the PM by detecting a reflected pulse from a reflective tape attached to the side surface of the male part of the PM coupling. This sensor is capable of measuring speeds up to 250 krpm, which is well above our maximum desired frequency. A small plug & play camera, capable of 60 frames per second, and the associated light source are installed inside the vacuum chamber to monitor and record the experimental process. An *S950-SM* silicon diode sensor [117] mounted on the copper plate is used as the temperature

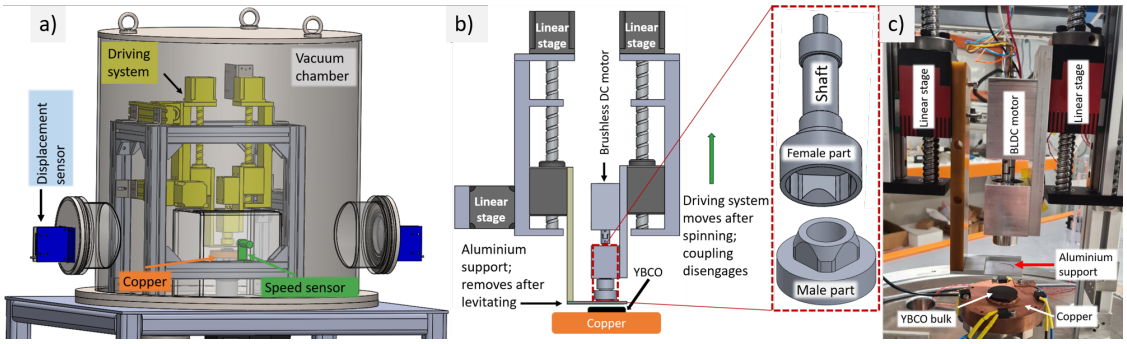

Figure 3.7: Schematic demonstration of the test rig (a), the driving system (b), and a photo of the driving system (c).

reference. The temperature of the motor and ceramic bearings is measured by XP-100 sensors. The XP-100 sensors were calibrated against the standard curve of the diode sensor by mounting them together on a copper plate during a cool-down/warm-up measurement sequence. The temperature of the superconducting puck is controlled by a *Cryocon-26* controller [118].

3.8 Dynamic Measurement rig: Horizontal Configuration

A dynamic test rig was designed and built based on the setup of Hull *et al.* [64]. In this configuration the rotational axis is perpendicular to the levitation force, so it can be considered as a journal bearing. In general, The test rig consists of a PM rotor levitated by HTS bulks, driving system, and cryogenics and vacuum system. The general scheme of this SMB is shown in figure 3.8.

3.8.1 Rotor

The rotor consists of a fibreglass tube and three cylindrical PMs. The tube, supplied by *Kilwell Fibre Tube* [129], is 148 mm long, and its OD and ID are 12 mm and 10 mm, respectively. Identical N40 grade NdFeB PMs, 9.53 mm in diameter and 12.7 mm in length, with a remanent flux density of 1.25 T, are embedded at either end of the tube. These PMs are magnetized axially and interact with HTS bulks to act as the rotor of the superconducting bearing. The third PM is placed at the midpoint of the tube, forming the rotor of the driving system. This transversely magnetized N52 PM is of the same size as the levitation PMs. All PMs were supplied by SuperMagnetMan [130]. A small hole is drilled at either end of the tube to balance the pressure inside and outside the rotor, enhancing its operation under vacuum. The rotor parameters are shown in table 3.2.

Table 3.2: Rotor Parameters

Parameter	Value
Tube ID	10 mm
Tube OD	12 mm
Tube length	148 mm
PM diameter	9.53 mm
PM length	12.7 mm
Total mass	29 g
Moment of inertia	2.48×10^{-7} Kgm^2

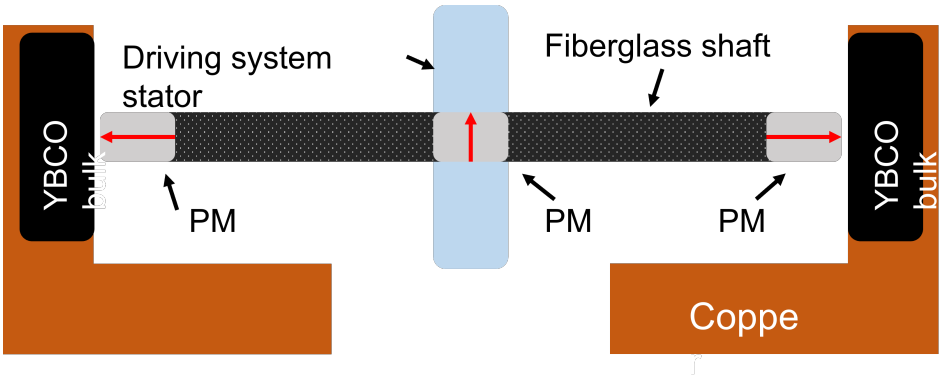

Figure 3.8: Schematic of the bearing and the driving system. Red arrows on PMs indicate their magnetization direction.

3.8.2 Driving System

The driving system consists of a three-phase winding connected in star configuration and a cylindrical PM, forming a BLDC motor. Solid 20 AWG copper wires are handwound on a non-conducting core made of a stack of three polymethyl methacrylate (acrylic) pieces, onto which the core pattern was cut (figure 3.11). Each core piece was 4.5 mm thick. This non-conductive core was chosen to eliminate eddy current and iron losses that act as disruptive forces on the rotor. The length of the core can be altered by adding or removing individual pieces.

A three-phase relay together with associated power electronics is used to switch the windings to an open circuit configuration after reaching the desired rotor speed. This prevents eddy currents from being induced in the winding during spin-down tests; otherwise, the induced currents would act as a magnetic brake on the rotating

Table 3.3: Driving System Parameters

Parameter	Value
Core ID	17 mm
Core OD	60 mm
Core length	13.5 mm
PM diameter	9.53 mm
PM length	12.7 mm
Copper wire diameter	0.85 mm
Turns per phase	44
Phase inductance	10.8 μH

shaft. A *SuperVolt* speed controller model $OOTDTY$ is used to adjust the rotor speed [131]. The driving system parameters are shown in table 3.3.

In order to hold the rotor in place while cooling the HTS bulks, a mechanical arm driven by a servo mechanism was used.

3.8.3 Superconducting bearings, cryogenics and vacuum system

The stator part of the superconducting bearing consists of two $YBa_2Cu_3O_{7-\delta}$ discs, both of which are 28 mm in diameter and 10 mm thick [105]. The HTS discs are fully recessed in L-shaped copper bars. The L-shaped copper bars are mounted on a base copper plate which is connected via a flexible thermal link to a *Coolstar* single stage 0/40 coldhead (42 W @ 77 K) driven by a *K450* helium compressor. The thermal link consists of a stack of 10 copper foils. Each copper foil is 150 mm long, 40 mm wide, and 0.2 mm thick. These foils are soldered together over over 25 mm of their length at either end. The flexible path provides more damping than a rigid busbar and can absorb the vibrations imposed by the cryocooler. It also provides more contact surface area compared to copper braids which enhances the cooling process. Figures 3.9 and 3.10 show the cryogenics system and the top view of the whole setup, respectively.

The driving system winding was potted with *Stycast ®2850 FT* and tinned copper braids were employed to transfer heat generated in windings to the base plate of the vacuum chamber (see figure 3.11d). *Stycast ®2850 FT* was used

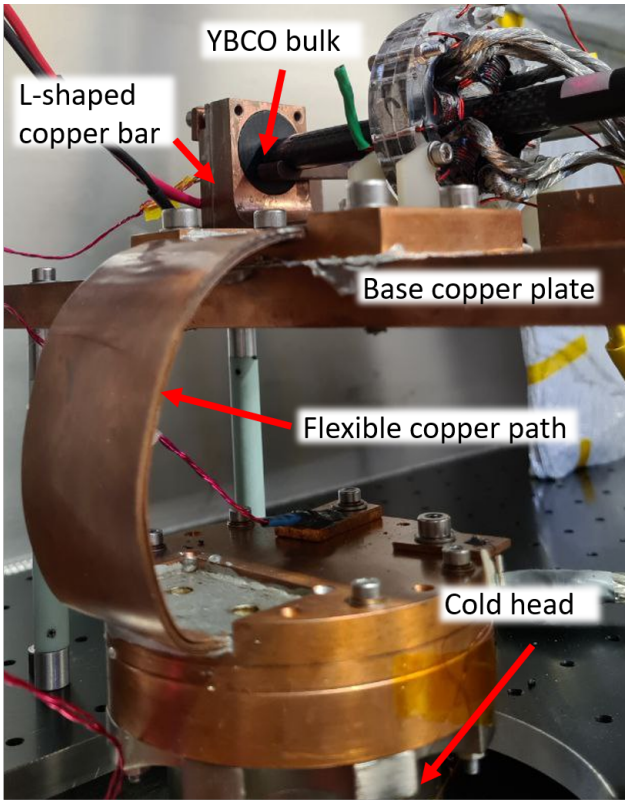

Figure 3.9: Photo of the cryogenics system, showing the flexible thermal link connecting the base copper plate to the cold head of the cryocooler. Indium foils were used between contact surfaces.

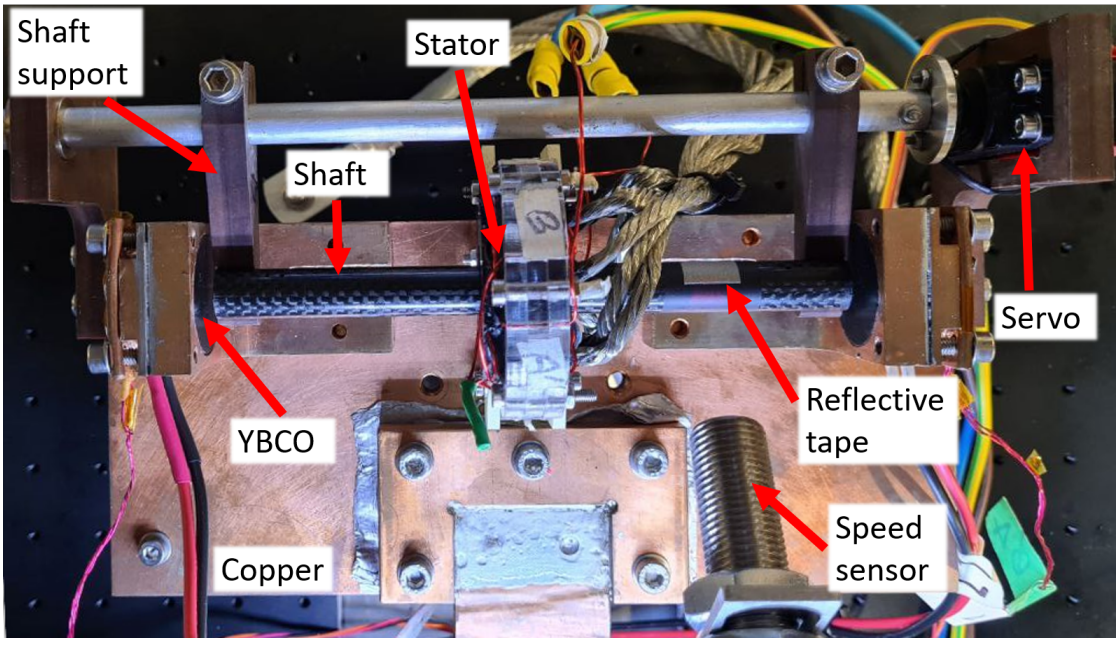

Figure 3.10: The top view of the experimental setup installed in the vacuum chamber.

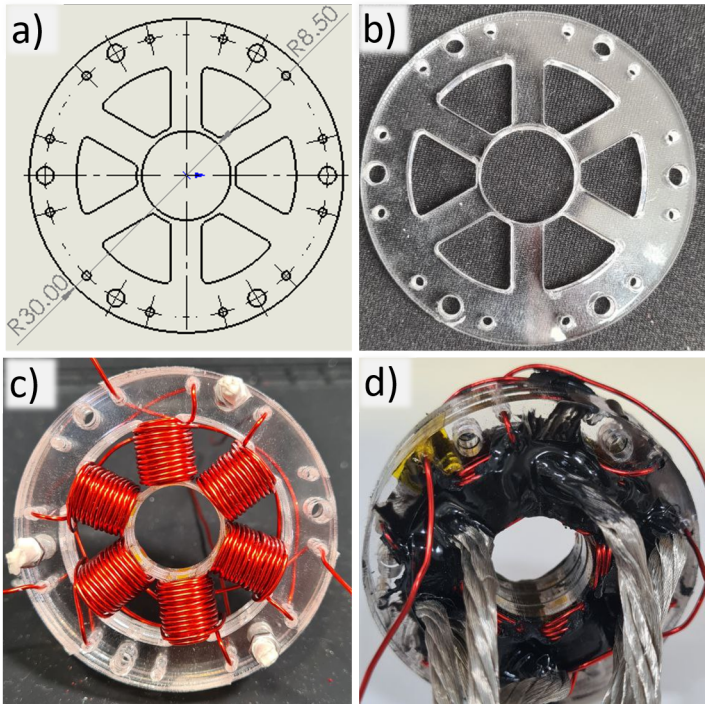

Figure 3.11: a) Design of the core pattern, b) One core piece, c) The stator made of a stack of core pieces shown in b and the copper winding, and d) The stator winding as used in the vacuum chamber.

because of its high thermal conductivity and low thermal expansion. This improves thermal stability of the stator during experiments in the vacuum chamber where convective heat transfer cannot happen.

A two-stage *Edwards T-Station 85* [125] vacuum system was used to maintain a pressure of 10^{-7} mbar inside a 0.228 m^3 (600 mm $\times$ 600 mm $\times$ 800 mm) stainless steel vacuum chamber. Because of the size of the vacuum chamber, an *Edwards nXDS 6i* vacuum pump [132] was employed to pump down from room pressure to the set point of the *Edwards T-Station 85* (5 mbar).

An *S950-SM* silicon diode sensor [117] mounted on the bottom end of the flexible thermal link is used as the temperature reference. The temperature of the driving system stator and YBCO bulks is measured by XP-100 sensors. The XP-100 sensors were calibrated using the same method explained in section 3.7.3. The temperature of the YBCO bulks is controlled by a *Cryocon-26* controller [118]. Another XP-100 sensor is bonded to the driving system winding, in order to monitor its temperature during operation. In order to mitigate the radiation heat transfer, the whole setup was enclosed in a plastic box covered with a shield made from multi-layer insulation (MLI). A *Monarch Instrument* remote optical sensor model *ROS-W* [128] mounted on the setup frame measures the rotational frequency of

the shaft. Sensor data was acquired using *National Instruments* CompactDAQ hardware and *LabVIEW* software.

4

A Non-Destructive Method for Estimating *E-J* Power Law Parameters in High-Temperature Superconducting Bulks

4.1 Introduction

Electromagnetic FE models can be used to simulate the key parameters of SMBs such as levitation force, stiffness, and losses prior to construction [32, 99, 133, 134]. Precise knowledge of the relation between electric field (E) and current density (J) in superconducting bulks is required to perform accurate FE simulations [98, 99, 109, 135]. Transport measurements on coated conductors show that the *E-J* relation can be approximated by a power law equation as $E = \alpha J^n$ [136]. However, unlike coated conductors, it is not possible to determine the *E-J* relation in large bulks using electrical transport measurements. Other researchers have attempted to measure the transport properties of bulk superconductors from trapped flux in bulks [137] or destructively by cutting I-shaped samples from a Gd-Ba-Cu-O bulk and performing transport measurements [138]. It may be possible to extend this destructive technique in order to measure the n-index of a bulk. An alternate way to extend this work is to calibrate the n-index predicted with the levitation force decay method.

This chapter covers the basic physics of estimating n-index and critical current density of high-temperature superconducting bulks via a non-destructive method. These two parameters can well describe the *E-J* power law in high-temperature superconductors. This chapter also explains experiments designed and performed to evaluate the method, and discusses the experimental results obtained from two test setups. Elaborated in this chapter is also the application of FBG sensors in SMBs to measure temperature and strain of the HTS bulk. The results of this chapter are partially published in [139].

4.2 Theory

Magnetic relaxation in type-II superconductors can be related to their *E-J* characteristics [136, 140–142]. This is based on the motion mechanism of Abrikosov

flux lines in type-II superconductors. Flux lines trapped at pinning centers in a type-II superconductor are not distributed evenly over the bulk volume. This density-gradient configuration of flux lines can cause flux lines to exert a force in the form of Lorentz force on each other [143]. When this force exceeds pinning force, flux lines can move inside the superconductor. This motion can create an electric field because each flux line contains a quantized magnetic flux Φ_0. The electric field induced by flux line motion is proportional to the velocity of flux lines in the direction of the Lorentz force. This velocity is a linear function of current density in normal materials, which results in a linear *E-J* relationship. In type-II superconductors, however, the velocity of flux lines is a nonlinear function of current density because of pinning [42]. This means that the *E-J* relationship in type-II superconductors is nonlinear.

According to the flux creep model, thermally activated flux motion which happens at a rate proportional to e^{-U/k_BT} results in flux lines' and their associated current loops' redistribution, thus changing the superconductor magnetization with time. Here, U is the activation energy, k_B is Boltzmann's constant, and T is temperature. In this model, the energy barrier U has been assumed to decrease linearly with current density J as:

$$U(J) = U_0\left(1 - \frac{J}{J_{c0}}\right) \tag{4.1}$$

Where J_{c0} is the self-field critical current density [42]. This linear dependence combined with time evolution of U described as [144]:

$$U(J) = k_BT\ln\left(t/t_0\right) \tag{4.2}$$

yields a logarithmic time dependence of current density as [42, 136]:

$$J = J_{c0}\left[1 - \frac{k_BT}{U_0}\ln\left(1 + \frac{t}{t_0}\right)\right] \tag{4.3}$$

where U_0 is the activation energy barrier in a non-penetrated sample, and t_0 is effective hopping time. Other models were proposed to describe the decay phenomenon in high-temperature superconductors, a detailed review of which can be found in [42]. Sun *et al.* assumed a power law *E-J* relation for a thin YBCO film in its critical state, and solved Maxwell's equations to derive the time dependence of current density as [136]:

$$J(t) = J_0\left(1 - \frac{1}{n}\ln\left(1 + \frac{t}{t_0'}\right)\right) \tag{4.4}$$

Compared to the flux creep model, $\frac{k_BT}{U_0}$ has been replaced with $1/n$ in Sun's model. They showed experimentally that the magnetization decay is inversely related to the n-index of *E-J* power law.

4.2.1 FBG Sensors Principle

The principles of FBG sensors are well described in [50]. These sensors are photo-inscribed into the core of an optical fibre by transversely exposing intense UV patterns or infrared femtosecond pulses [145]. An FBG reflects the incident light in the shape of a Gaussian-like spectrum at its Bragg reflection wavelength λ_B, which is dependent on the effective refractive index of the core (n_{eff}) and the periodic spacing of the gratings in a FBG (Λ):

$$\lambda_B = 2\Lambda n_{eff} \tag{4.5}$$

Several Bragg gratings can be inscribed in one fibre, each having a different λ_B. When a FBG experiences a change in temperature and/or strain, both the grating period (Λ) and the refractive index of the core (n_{eff}) will change. The sensitivity of a FBG to temperature and longitudinal strain can be described as [145]:

$$\frac{\Delta\lambda_B}{\lambda_B} = (\alpha + \xi)\Delta T + (1 + \rho_e)\epsilon \tag{4.6}$$

where, ρ_e is photo-elastic constant, α is the coefficient of thermal expansion, and ξ is the thermo-optic coefficient of the fibre material. ρ_e and ξ determine the change of refractive index due to longitudinal strain and temperature, respectively.

4.3 Results and Discussion

The relationship between decay parameters and superconductor characteristics was investigated by performing a parametric sweep study on n, J_c, and Z_{fin} using the FE model described in section 3.2. Figure 4.1 shows the simulation result for n-index = 21, $Z = 1$ mm (Z_{fin}), $J_c = 2.4 \times 10^8$ A/m^2, and $V = 1$ mm/s. It can be seen that the FE model adopted predicts the logarithmic levitation force decay while the PM is held at Z_{fin}. As the PM moves towards the superconductor, the levitation force increases and reaches a maximum at Z_{fin}. Then, the PM is held at this position and the levitation force starts to decay with time. The movement and decay sections are indicated in the figure with green arrows, and a logarithmic curve is fitted into the decay section.

Based on the linear relation between levitation force and current density (Eq. 3.3), the decay model proposed by Sun *et al.* [136] was adopted which results in an equation for levitation force decay as:

$$F(t) = F_{max}\left(1 - \frac{1}{n}\ln\left(1 + \frac{t}{t_0}\right)\right) \tag{4.7}$$

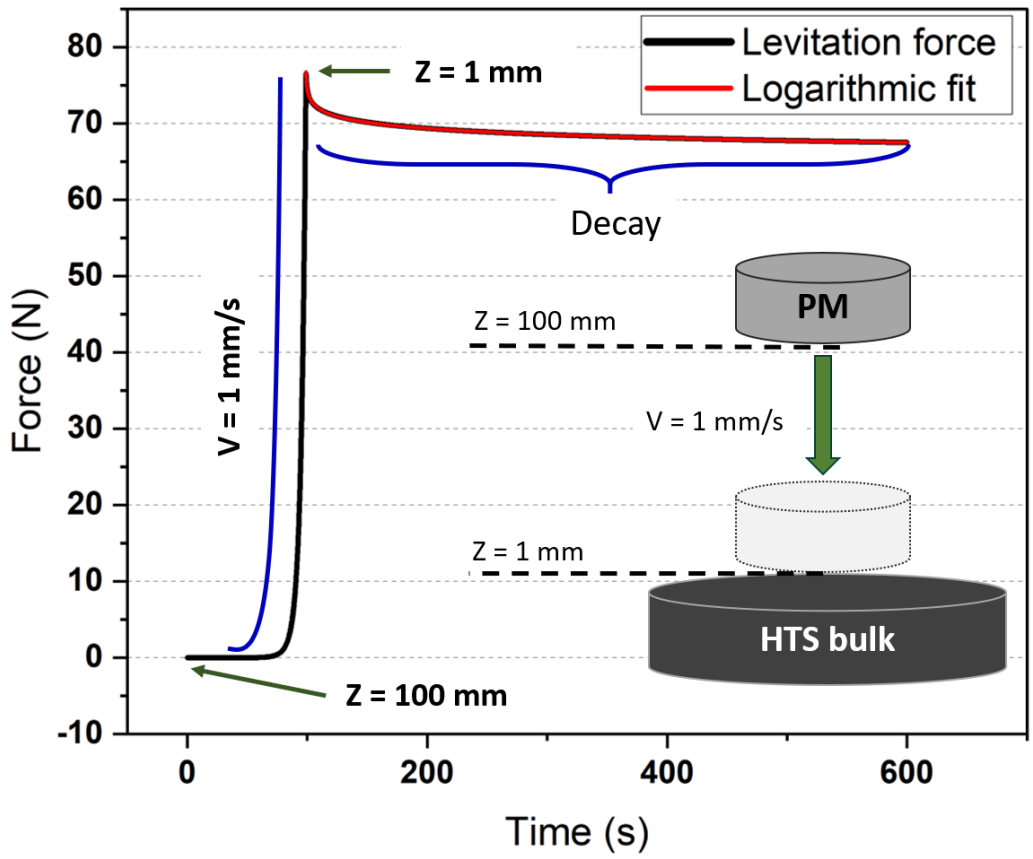

Figure 4.1: Simulated levitation force with respect to time for n-index = 21, Z = 1 mm, $J_c = 2.4 \times 10^8$ A/m^2, V = 1 mm/s. The red line shows the logarithmic curve fitted into the decay section with an R^2 value of 0.999. The inset shows the PM movement scenario.

Here, F_{max} is the maximum levitation force and n is the exponent of the E-J power law. Equation 4.7 was fitted to the data using *Origin* software [146] to determine parameters F_{max}, n, and t_0 (Fig. 4.1).

The extracted flux creep exponent n_{ex} was found to be independent of velocity. Therefore, for all simulations and measurements, a constant velocity of 1 mm/s was used. Figure 4.2 shows the relationship between the actual flux creep exponent and n_{ex} at different J_c and displacement values. A wide range of n-index was studied in order to explore the sensitivity of the method. This wide range covers the realistic values of n-index (10-50) as well as large values (100 and 200) to explore the sensitivity when it tends toward the Bean's model ($n = \infty$).

A linear relationship between the actual n-index and the values extracted from the fits can be observed. However, the slope of the fit values versus the actual flux creep exponent is not universal. Although Eq. 4.4 was proposed for fully penetrated films, this method is still applicable for partially penetrated samples. The levitation force still decays logarithmically, but at a rate different to that of the shielding

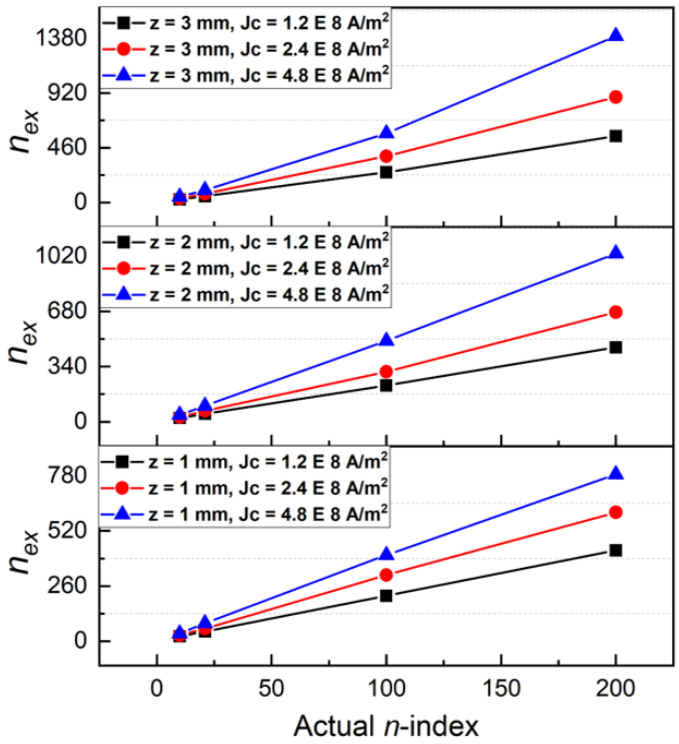

Figure 4.2: The extracted flux creep exponent n_{ex} with respect to the actual n-index in simulations. Each subplot shows the results for a different Z value, and each line represents a different J_c value. Error bars do not show in this scale. © 2021 IEEE [139].

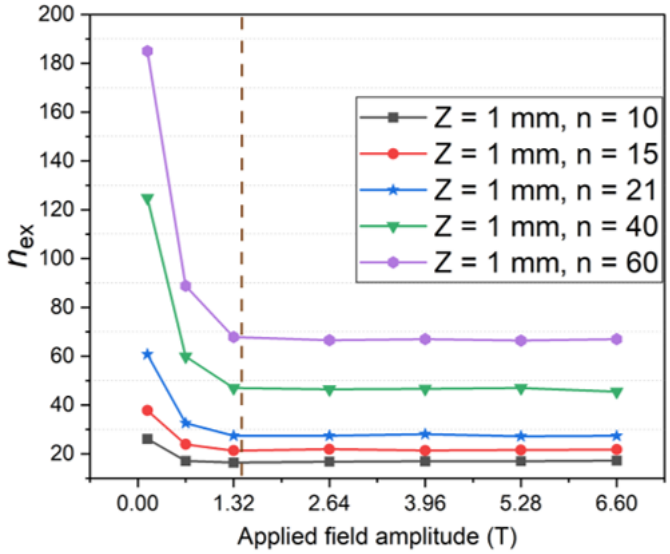

Figure 4.3: Extracted n-index vs the applied field magnitude for various n-values input to the model. Parameter Z indicates the vertical separation and $J_c = 2 \times 10^7$ A/m^2. The dashed line indicates the full penetration field. Error bars do not show on this scale. © 2021 IEEE [139].

current [110]. This can cause a deviation between the extracted creep exponent and the true n-index of the model. This deviation is due to incomplete penetration of the bulk. The effect of the amount of field penetration on the extracted n-index was investigated. Figure 4.3 shows the extracted n-index with respect to the applied magnetic field for different actual n-indexes used in the model. The applied magnetic field refers to the remanent magnetization of the PM in A-formulation. As can be seen, all curves become constant beyond a certain applied field (roughly indicated by the dashed line) at which point the shielding current occupies the entire volume of the bulk. The deviation between the actual and extracted n-indexes is significantly reduced when the bulk is fully penetrated. However, there is still a constant offset between them, which can be investigated in the future studies.

The levitation force decay measured in the experimental rig described in section 3.4 is shown in figure 4.4. In general, the levitation force behaviour was as expected. However, a restoration of the observed levitation force (highlighted in figure 4.4) can be seen which may be due to a decrease in the PM temperature. The results show a force increase of around 1.6 %. This is consistent with the expected increase in magnetization caused by the PM cooling to at least 220 K [147].

To determine J_c from the data, a parametric sweep study of maximum force vs J_c was carried out for n-index = 21, Z = 1 mm, and V = 1 mm/s. The measured maximum force (42.61 N) matched for a J_c of 6.46×10^7 A/m^2. J_c can also be estimated using trapped field measurements, where $B_{trap} = K\mu_0 J_c a$. Here, a is the sample radius, and K is a geometric factor [137, 148]. According to the data provided by the manufacturer, this bulk is capable of trapping a magnetic field of 0.9 T in an applied field of 1.9 T in FC condition at liquid nitrogen temperature (77 K). This method implies a self-field J_c of 1.28×10^8 A/m^2. In the experiments carried out the average flux density at the surface is 0.36 T (figure 4.5) which would reduce the in-field J_c. According to J_c(B, θ, T) data for REBCO in the HTS wire database [149] a 0.36 T applied field can reduce J_c to 48 % of the self-field value. This gives a J_c (0.36 T) of 6.13×10^7 A/m^2 which is in close agreement with the inferred J_c of 6.46×10^7 A/m^2. A similar J_c(B) behaviour has also been reported for GdBCO [150, 151] and YBCO [152, 153] bulks. Some discrepancies might be due to differences in the J_c(B) behaviour between bulks and wires, the impact of surface degradation of the bulk on the trapped field characteristics, and the angle of the applied magnetic field with respect to the surface of the superconductor. Next, a parametric sweep using this J_c with n-indexes of 10, 21, 40, 60, 100, and 200 was carried out, allowing a comparison to be made with the experimental results in figure 4.6. These results imply a flux creep exponent of between 40 and 60. It should be noted that there is some uncertainty in fitting the force decay curve due to the previously mentioned impact of temperature on the remanent magnetization of the PM.

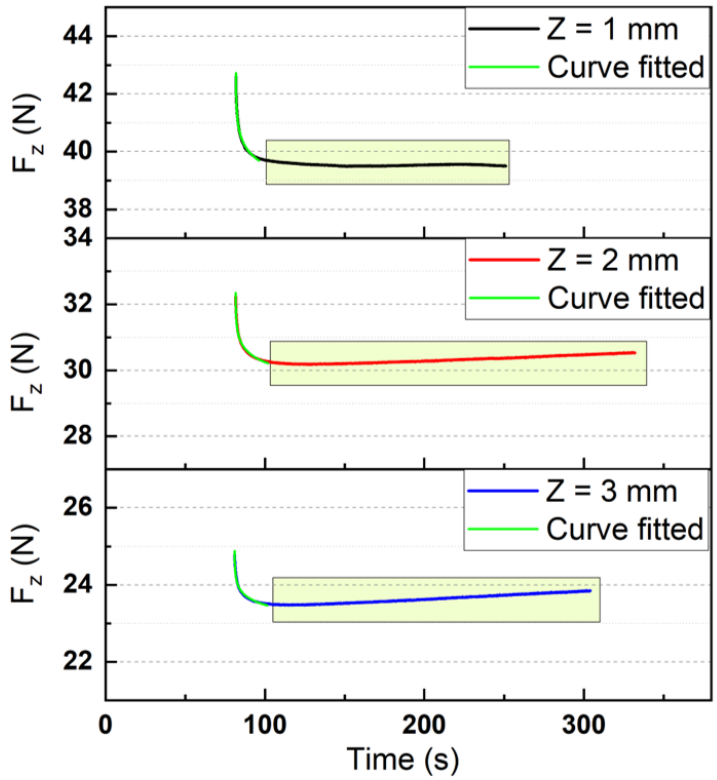

Figure 4.4: Experimental results of levitation force decay measured at $Z = 1$ mm, 2 mm, and 3 mm. Equation 4.7 was fitted into the initial decay stage of all curves. Highlighted boxes show the levitation force restoration.

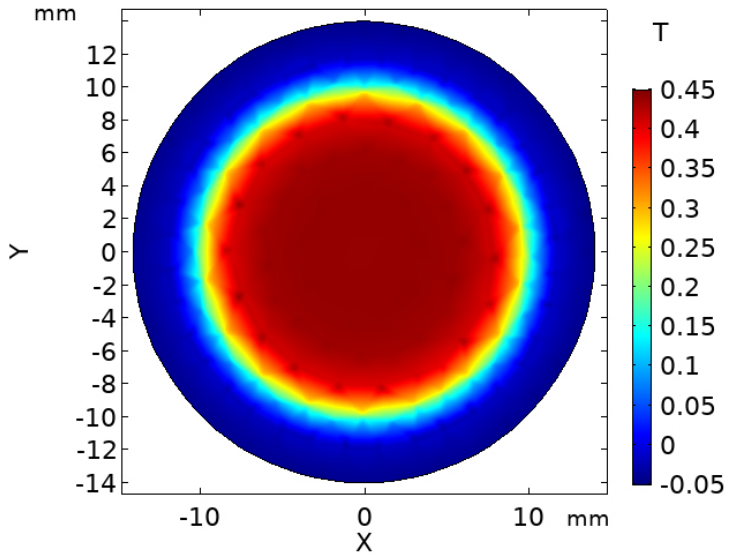

Figure 4.5: Vertical component of magnetic flux density (B_z) experienced by the top surface of the superconductor bulk for $Z = 1$ mm.

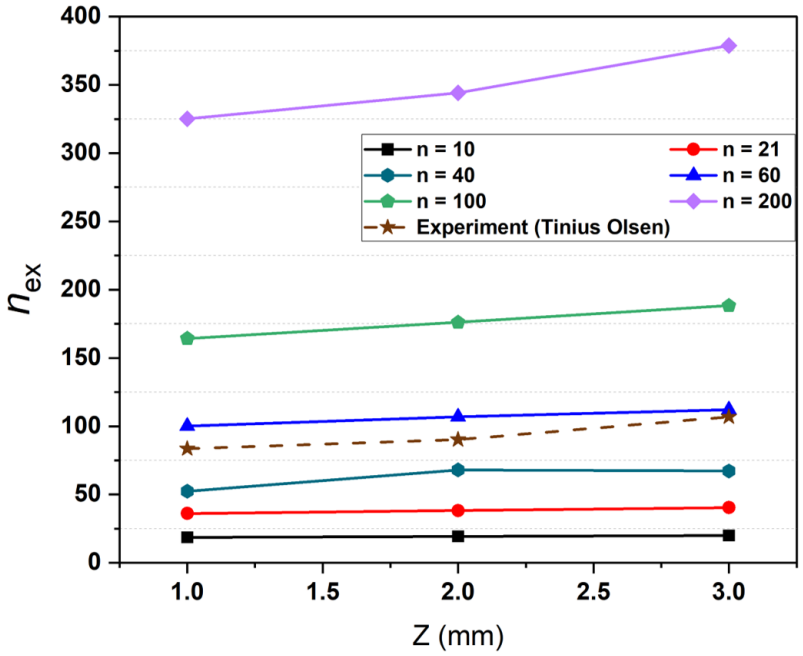

Figure 4.6: Extracted flux creep exponent (n_{ex}) versus displacement obtained from simulations (solid lines) and measurements (dashed line). The critical current density in simulations is 6.46×10^7 A/m^2. Error bars do not show in the graph scale.

4.4 Levitation Force Decay in Conduction Cooled Disc-Shaped Bearing

In the previous section, the impact of temperature on levitation force decay behaviour was observed and discussed. In this section, levitation force decay is studied in a cryo-cooled SMB housed in a vacuum chamber. This section also describes implementation of FBG sensors in superconducting bearing environment for temperature and strain measurements.

In order to mitigate thermal variation impact on PM magnetization and consequently on levitation force decay, experiments were carried out on the disc-shaped SMB in the dry cryo-cooled experimental rig described in section 3.5. As the PM is not exposed to cold nitrogen gas, it is expected that its magnetization will remain constant.

Ideally, HTS bulk should be in an isothermal condition during levitation force decay experiments, because temperature fluctuations may disrupt flux line distribution in the bulk which can change decay behaviour. In experiments performed in the *Tinius Olsen* rig described in section 3.4, isothermal conditions were achieved by using liquid nitrogen. The temperature of the top surface of HTS bulk in the cryo-cooled rig described in section 3.5, however, may be different to

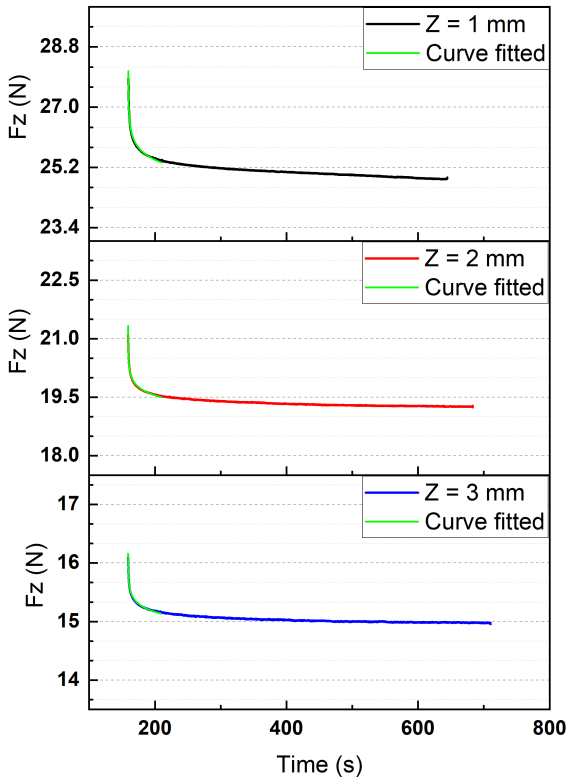

Figure 4.7: Experimental results of levitation force decay measured at Z_{fin} = 1 mm, 2 mm, and 3 mm in the disc-shaped bearing. Equation 4.7 was fitted into the initial decay stage of all curves. No force restoration was observed during these experiments.

the temperature read by the diode sensor, due to the thermal resistance and time constant between the HTS bulk and the sensor.

Conventional electronic sensors such as PT100 and diode could be employed to monitor the HTS bulk top surface temperature. The output signal of these sensors, however, may be affected by the varying magnetic field created by PM movement in levitation force decay experiments. In order to prevent any electromagnetic interference, an FBG sensor was used to measure the top surface temperature of the HTS bulk in this experimental rig (section 3.6).

Levitation force decay measurements were performed on the disc-shaped SMB. The PM was 48 mm from the HTS bulk (along Z axis) during the cooling process to achieve ZFC condition. The PM was then moved towards the HTS bulk at a velocity of 1 mm/s. Figure 4.7 shows the results of levitation force decay for Z_{fin} = 1 mm, 2 mm, and 3 mm. The levitation force increases and reaches a peak at Z_{fin}, before decaying logarithmically from f_{max} with time. As can be seen, levitation force does not restore while the PM is held at Z_{fin}. Under ideal conditions, forces in x

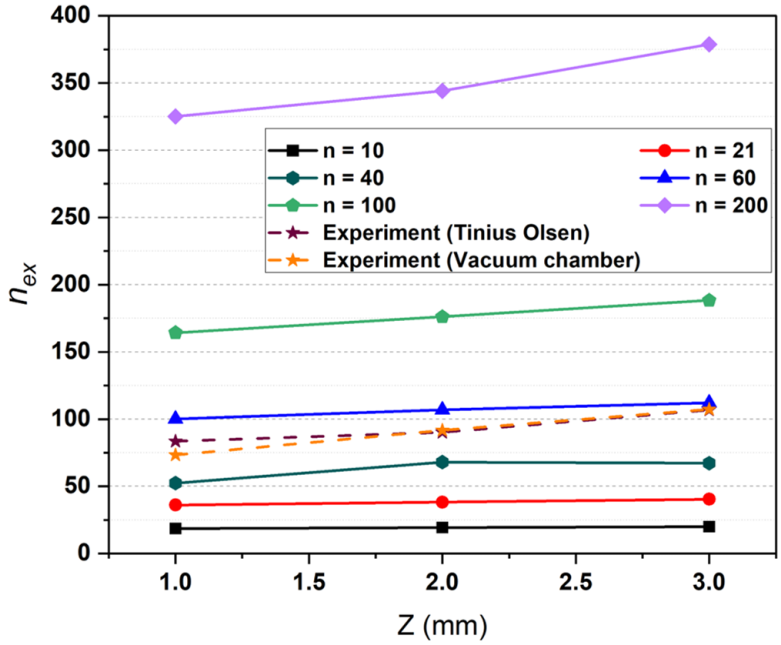

Figure 4.8: Extracted flux creep exponent (n_{ex}) versus displacement obtained from simulations (solid lines) and two sets of experiments (dashed lines). The critical current density in simulations is 6.46×10^7 A/m^2.

and y directions should be zero. However, a finite force was measured in x and y directions which could be caused by PM-HTS misalignment or inhomogeneities in HTS bulk and/or PM [111]. Although the same PM and a different HTS bulk with the same dimensions as described in section 3.4 were used, the maximum levitation force measured in the vacuum chamber is smaller than that measured in section 4.3. Possible causes include the PM-HTS bulk misalignment along X and Y axis, an HTS bulk of lower quality with smaller J_C, or deflection-induced miscalculation of displacement along the Z axis in the vacuum chamber.

Figure 4.8 shows that the extracted flux creep exponent versus displacement obtained from both experimental rigs are in good agreement. Compared to simulations, the new results also suggest a flux creep exponent between 40 and 60 for the bulk used in this experiment.

Figure 4.9 shows the FBG sensor readings associated with levitation force decay experiments in the disc-shaped bearing shown in figure 4.7. In each case, λ_B at the isothermal condition before moving the PM (at 77 K) was considered as λ_0. The spectrum centroid wavelength decreases and then becomes constant during levitation force decay measurements. The decrease in spectrum centroid wavelength could be caused by a temperature-dependent strain and/or magnetostrictive strain. Figure 4.10 shows the calibration curve during a natural warm up process in the rig. In the calibration curve, λ_0 is λ_B at 77 K (1537.28 nm). The diode sensor

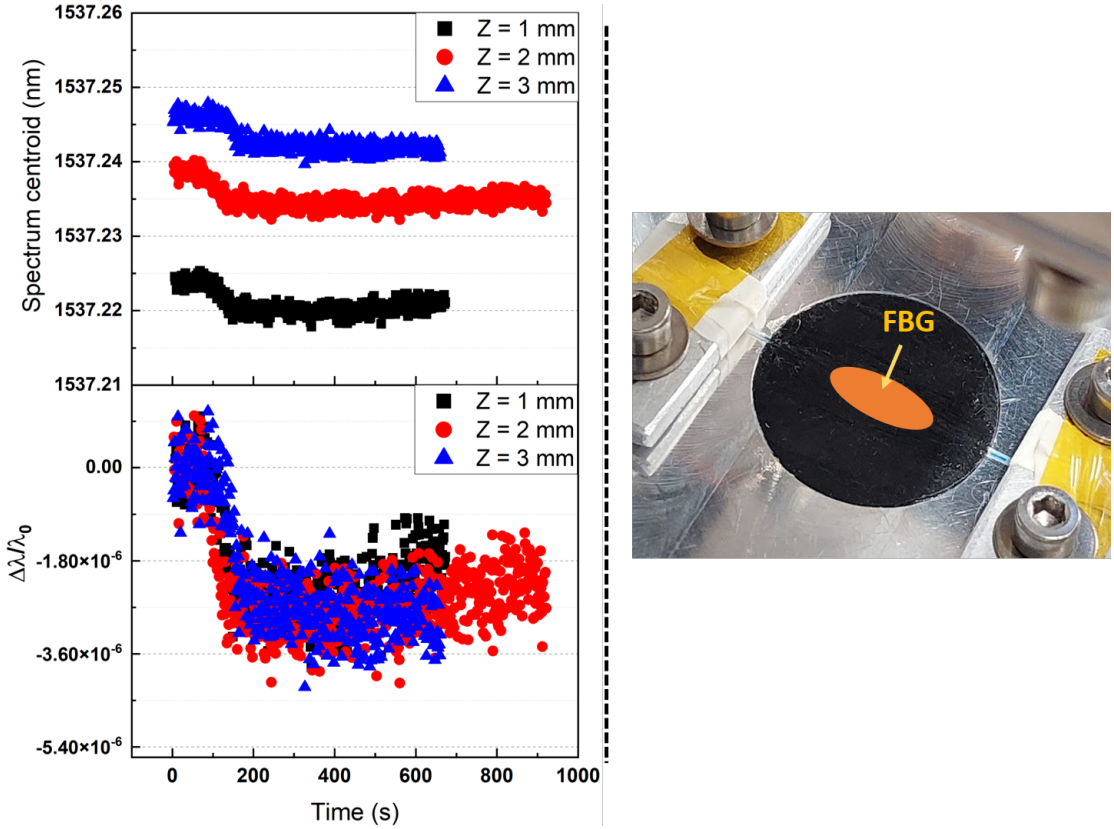

Figure 4.9: Left: spectrum centroid wavelength in levitation force decay experiments for 3 different displacements. Right: The sensor was bonded to the center point of the HTS disc with *Apiezon N* grease.

was used as the temperature reference. According to the data presented in figures 4.9 and 4.10, a $\frac{\Delta\lambda}{\lambda_0}$ of 2.7×10^{-6} could imply a temperature decrease of almost 0.7 K. However, during the levitation force decay experiments, the temperature was controlled by a PID loop and it was expected to increase slightly by radiative heat from the PM and/or Joule heat created by shielding currents. As a result, temperature was unlikely to decrease in these experiments.

The wavelength drop in figure 4.9 indicates the fibre was subjected to contraction. This contraction could be the flux-pinning-induced tensile stress in the bulk [154]. The applied magnetic field in these experiments (0.36 T at $Z_{fin} = 1$ mm) was smaller than the penetration field ($B_p = \mu_0 J_c r \approx 1.14$ T); thus, according to Bean model the Lorentz force acting on flux lines would be towards the center of the HTS disc [57, 154]. This contracting force, however, was not properly read by the FBG sensor because it was bonded to the HTS disc center point, where the magnetic field has not penetrated. Figure 4.11 shows the flux-pinning-induced tensile stress mechanism in a partially penetrated HTS disc in a longitudinal magnetic field. As the magnetic field has partially penetrated the HTS disc from its circumference to a depth r_p, it

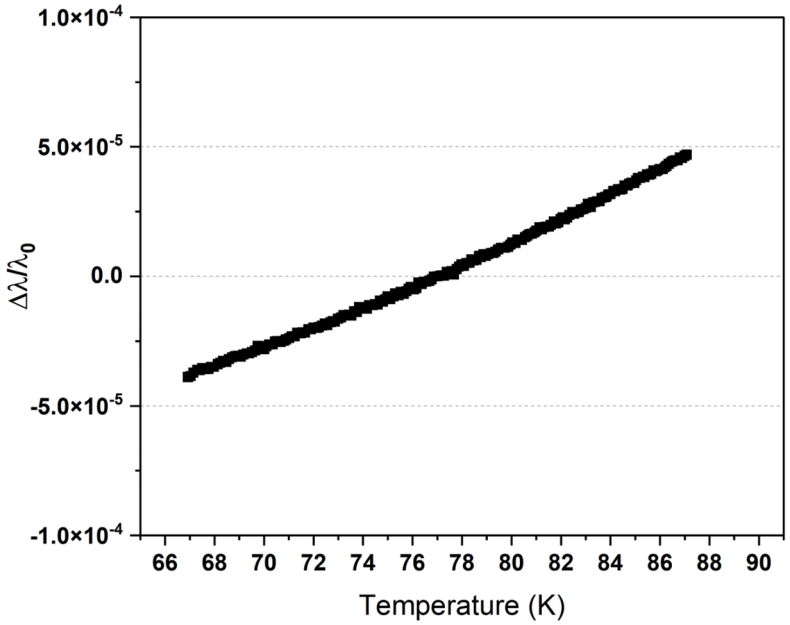

Figure 4.10: Calibration curve of the FBG sensor employed in levitation force decay experiments. λ_B at 77 K (1537.28 nm) was considered as λ_0.

is expected that the flux-pinning-induced strain would be distributed over the disc radius [57, 154]. In order to investigate this, the fibre was bonded to the HTS disc surface with *Apiezon N* grease at two points almost 20 mm apart, along the disc diameter. No adhesive was applied between the FBG sensor (the sensing length of the fibre) and the disc. The same decay experiments were performed on the bearing and the results are shown in figure 4.12. The $\frac{\Delta\lambda}{\lambda_0}$ measured in this method is larger by almost two orders of magnitude than those shown in figure 4.9. This implies that the fibre may have been bonded to the region where magnetic field penetrated and hence it could pick up the flux-pinning-induced tensile stress. As the applied magnetic field increases (or Z_{fin} decreases), more flux lines are trapped inside the disc, which increases the flux-pinning-induced tensile stress in the disc. This is consistent with the results reported in [57, 154, 155].

In order to map the flux-pinning-induced stress distribution across the HTS surface, two individual FBG sensors were bonded to the top surface of the HTS bulk along its diameter by *Apiezon N* grease (see figure 4.13). The same levitation force decay experiment at $Z_{fin} = 1$ mm and v = 1 mm/s was carried out. Figure 4.13 shows the response of the FBG sensors. As can be seen, the amplitude of $\frac{\Delta\lambda}{\lambda_0}$ is of the same order of magnitude as those shown in figure 4.9, where the sensor was bonded to the center point of the bulk. This implies that almost no stress distribution was recorded during decay experiments. The larger magnitude of $\frac{\Delta\lambda}{\lambda_0}$ reported in figure 4.12 might be caused by the difference between bonding

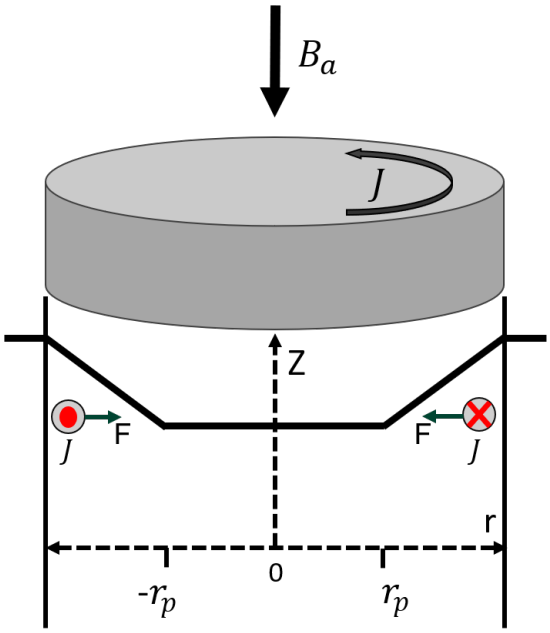

Figure 4.11: Magnetic field penetration pattern and Lorentz force mechanism in a superconductor disc subjected to axial (Z direction) magnetic field

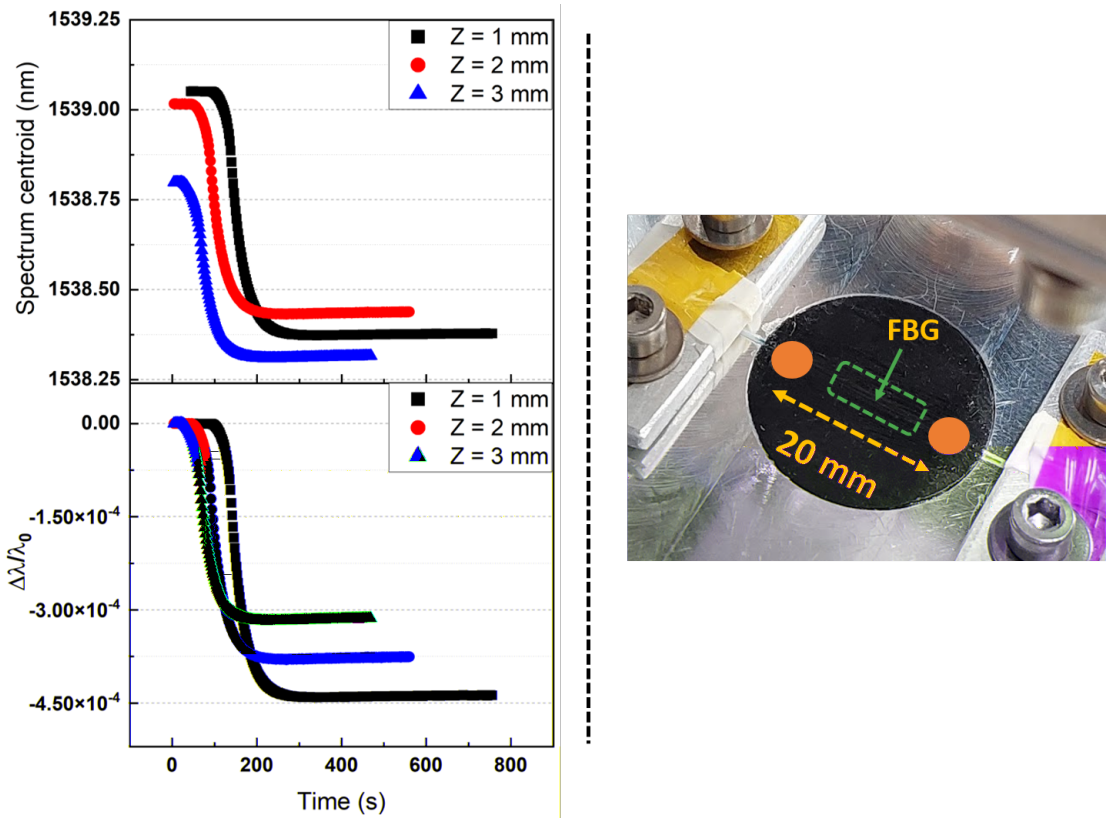

Figure 4.12: Left: spectrum centroid wavelength in levitation force decay experiments for 3 different displacements. Right: the sensor was not bonded to the HTS disc. fibre was bonded with *Apiezon N* grease to the HTS bulk at two points close to the bulk circumference along its diameter.

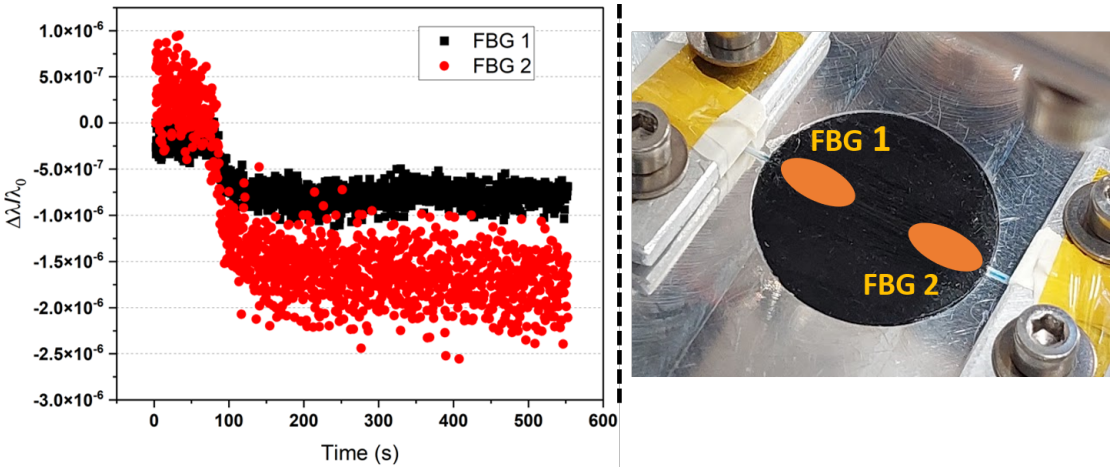

Figure 4.13: Left: spectrum centroid wavelength in levitation force decay experiment for at v = 1 mm/s and Z = 1 mm. Right: 2 sensors were bonded to the HTS disc surface near its circumference.

methods in the two experiments. The FBG sensor (the sensing length of the fibre) in figure 4.12 was not bonded to the HTS bulk and the fibre was bonded to the bulk at two points near the bulk circumference by *Apiezon N* grease. This can make the sensor susceptible to three-point bending caused by the levitation force, which can contract the fibre and the sensor.

In this section, the importance of monitoring the temperature of HTS bulk surface facing the PM, and the issues of employing electronic sensors for this temperature monitoring were discussed. In order to overcome these issues, FBG sensors were successfully implemented into an actual SMB environment. The results show that the temperature at the surface of interest was accurately measured, and did not change over the course of the experiment. However, an unexpected behaviour was seen in the output signal of the FBG sensor, which was believed to be created by flux-pinning-induced tensile stress. The output signal also appeared to be influenced by bonding methods, which can be investigated in future studies.

The non-destructive method, introduced in this section, will be applied on a novel SMB configuration in the next section.

4.5 Levitation Force Decay in a Trapezoidal Toroid-Shaped Bearing

4.5.1 Introduction

Paihau-Robinson Research Institute has been developing an HTS motor for a hybrid aircraft propulsion system [156]. High-speed low-loss superconducting bearings seem

to be a solution to overcome speed limits and increase the power-to-weight ratio of hybrid propulsion systems. Since the main disadvantage of SMBs is their low stiffness compared to mechanical bearings, a novel thrust SMB was designed and built at the Institute aiming at enhancing bearing stiffness. Levitation force and stiffness of this SMB have been studied before [100, 111]. In order to estimate the flux creep exponent (n-index) of the trapezoidal toroid HTS assembly in this bearing (described in section 3.5), levitation force decay experiments were performed and results are presented in this section.

4.5.2 Results and Discussion

In these experiments, the HTS assembly was cooled to 68 K, with the PM far enough to achieve ZFC condition. The displacement Z represents the vertical distance between the bottom surface of the PM and the top surface of the small HTS disc. The minimum achievable displacement with this test setup is 2.2 mm to avoid physical contact between PM and HTS bulk. After reaching the desired temperature and performing zeroing of the load cells, the PM which was initially at a displacement of $Z = 45$ mm above the HTS, was moved downwards to a minimum displacement of $Z_{fin} =$ 2.6 mm, 3.7 mm, and 5 mm at the velocity of 1 mm/s. Then, it was held at Z_{fin} until the first derivative of the levitation force with respect to time fell below the load sensor noise level. Figure 4.14 shows the results of decay experiments performed on this SMB. Equation 4.7 was fitted to the decay curves.

An unexpected two-stage decay was observed in the data which is not seen in simulations (see figure 4.15). In order to investigate this behaviour further, levitation force decay experiments were performed at different velocities for $Z_{fin} = 5$ mm. Figure 4.16 shows the experiment results at velocities of 0.05, 0.1, 0.5, 1, 5, and 10 mm/s. The maximum levitation force becomes larger and levitation decay occurs faster as the velocity increases. After a sufficient time, all curves converge to the same force. Although this may lead us to think that higher movement velocity could lead to higher levitation force, there is a threshold of velocity above which the levitation force plateaus out. These results agree with those reported in [38]. This can be discussed from two points of view. First, as the velocity increases, the induced current in the HTS bulk will increase, which, based on the $E - J$ power law, leads to an increase of superconductor resistivity. The increased resistivity, in turn, suppresses the rise in current. As a result, the levitation force which is dependent on the induced current inside the HTS bulk can not be raised without limitation. Second, when the current inside the HTS bulk increases, it helps trapped flux lines leave the pinning centres. In other words, increasing the

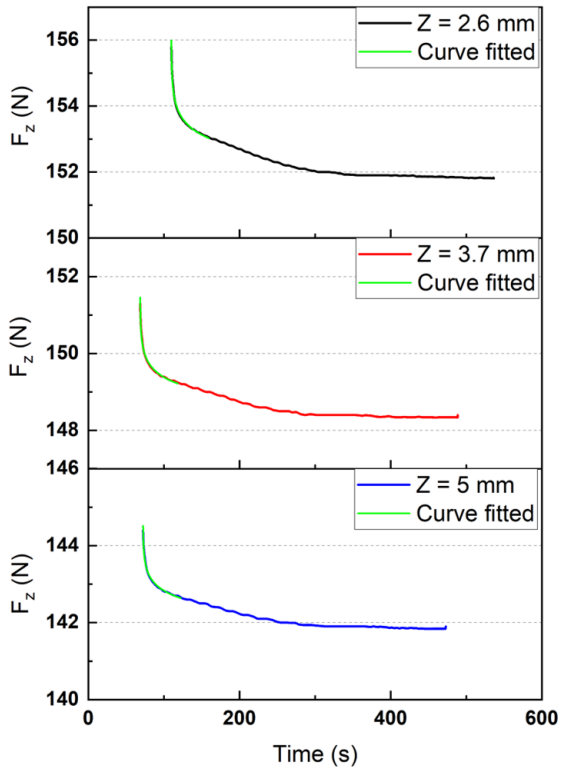

Figure 4.14: Experimental results of levitation force decay measured at Z = 2.6 mm, 3.7 mm, and 5 mm in the trapezoidal toroid-shaped bearing. Equation 4.7 was fitted into the initial decay stage of all curves. A two-stage decay can be seen in all cases.

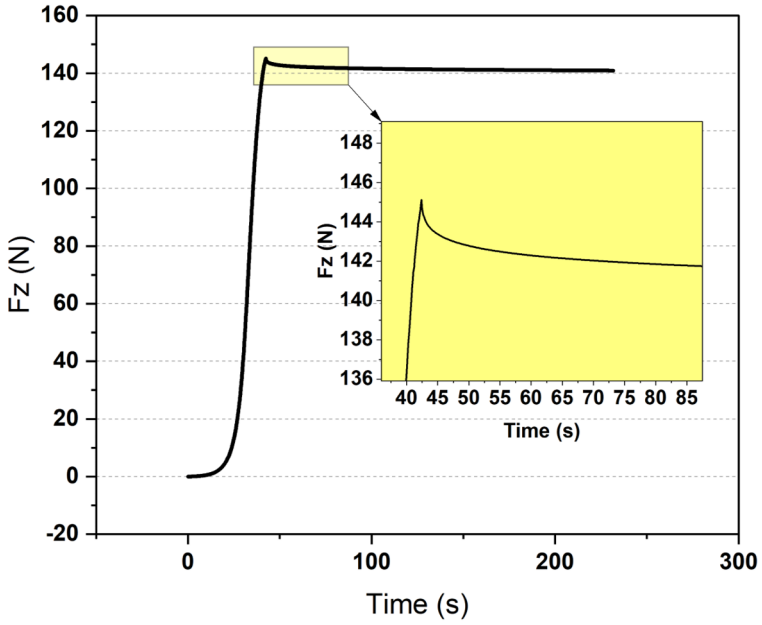

Figure 4.15: Levitation force decay simulation in the trapezoidal toroid-shaped bearing for $Z_{fin} = 2.6$ mm, $v = 1$ mm/s, $J_c = 21.6 \times 10^8$ A/m^2, and $n = 40$. The two-stage decay is not seen in the simulations.

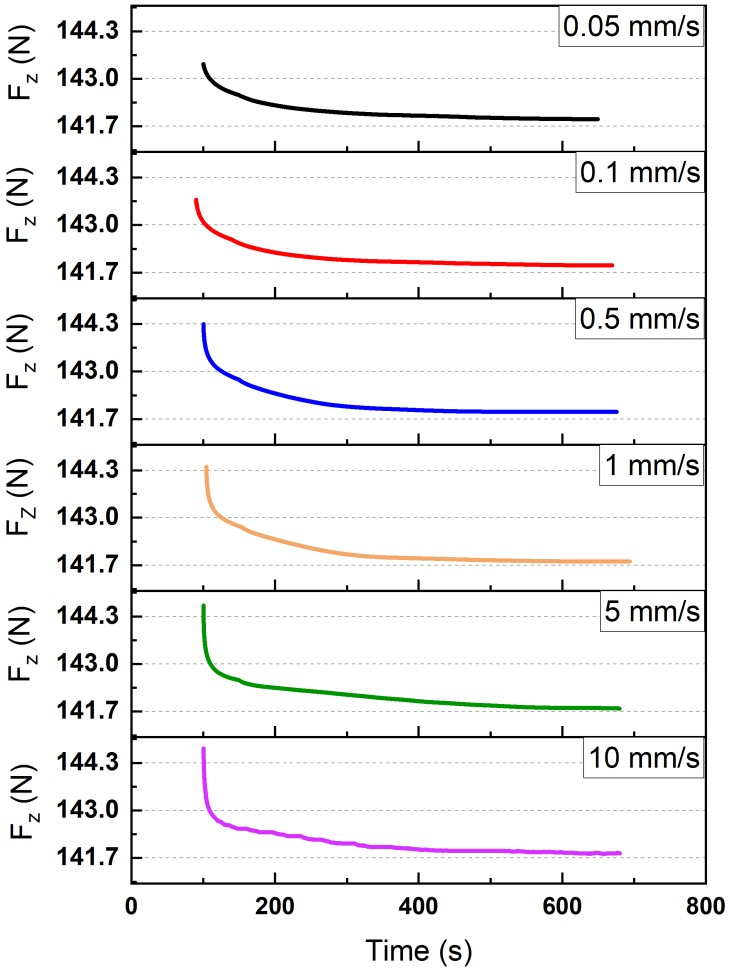

Figure 4.16: Levitation force decay from the maximum to the steady state at different velocities and $Z_{fin} = 5$ mm. The two-stage behaviour becomes more intense at velocities above 1 mm/s.

velocity enhances the flux flow which decreases the shielding current. This can limit the increase in the maximum levitation force [38].

The two-stage behaviour appeared at all velocities, but it was more intense at velocities above 1 mm/s. This two-stage decay was not observed in the disc-shaped SMB configuration, nor in the simulations of the trapezoidal toroid-shaped puck. This might be a temperature related effect which is not modelled in simulations. The trapezoidal toroid HTS assembly is not recessed in the aluminium plate. Considering the thermal conductivity of YBCO, thermal resistance and time constant between the feedback sensor on the outer side of the toroid and the cryocooler coldhead, the temperature at the inner surface of the toroid may be different to that read by the

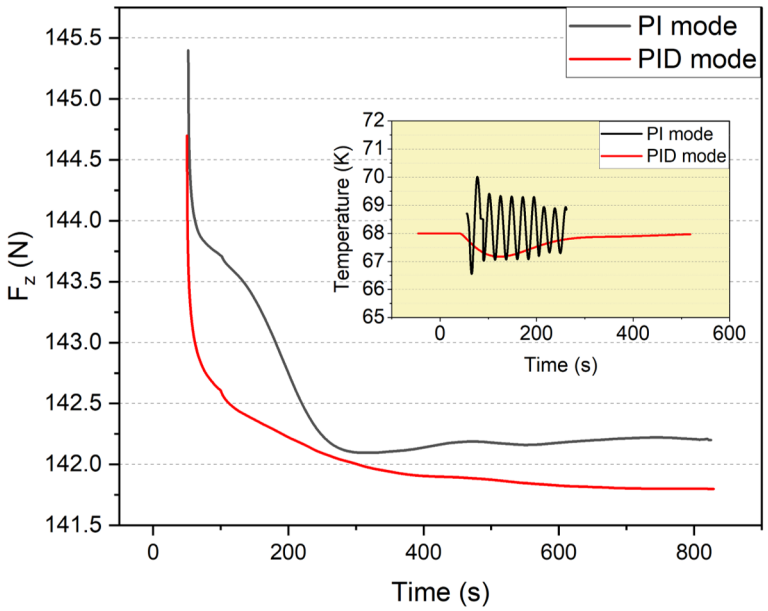

Figure 4.17: Levitation force decay measurement at $Z_{fin} = 5$ mm and $V = 10$ mm/s in the trapezoidal toroid-shaped SMB with the controller in PI and PID modes. The inset shows the temperature measured by feedback sensor mounted on the toroid outer side.

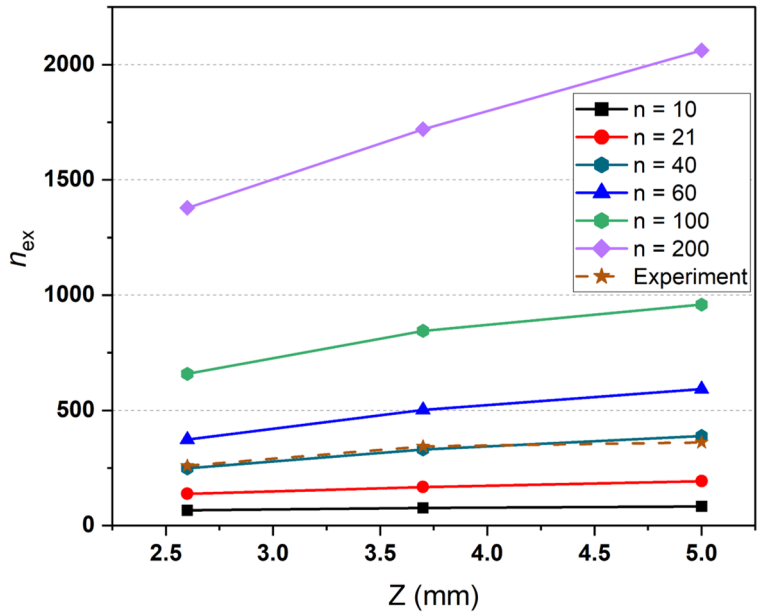

Figure 4.18: Extracted flux creep exponent (n_{ex}) versus displacement obtained from simulations (solid lines) and experiment(dashed line) performed on the shaped bearing. The critical current density in simulations is 21.6×10^8 A/m^2.

feedback sensor. In order to test this possibility, figure 4.17 shows the levitation force decay measured at $Z_{fin} = 5$ mm and $V = 10$ mm/s with temperature controller operating in PI and PID modes. The isothermal condition was not achieved in either case, but temperature fluctuation and the two-stage decay behaviour are more intense when the controller operates in PI mode. As a result, the two-stage decay is shown to be due to non-isothermal conditions of the bulk, most likely from heating of the upper surfaces of the HTS due to the nearby room-temperature magnet and/or dissipative shielding currents.

A parametric sweep using $J_c = 21.6 \times 10^8$ A/m^2 with n-indexes of 10, 20, 40, 60, 100, and 200 was carried out, allowing a comparison to be made with experimental results. This J_c was calculated before by our group [111]. According to the data shown in figure 4.18, the n-index of the HTS assembly in this bearing matches with the simulation data for n-index of 40.

4.6 Summary

The nonlinear E-J characteristics of a bulk superconductor can be identified through levitation force decay measurements. Linking an FE model of levitation force with a simple flux creep model should allow superconducting critical current and flux creep exponent (n) to be extracted from a physical measurement of force vs time. In section 4.3 the deviation between the actual and extracted n-indexes was found to be a function of the amount of field penetration experienced by the superconductor. This technique was applied to experimental force decay and obtained a flux creep exponent between 40 and 60 for the HTS bulks used in decay experiments performed in liquid nitrogen and in the cryo-cooled chamber. The same non-destructive method was applied to estimate the n-index in a trapezoidal toroid-shaped SMB, which resulted in an n-index of 40 for the HTS assembly in this configuration. The results, however, appeared to be affected by the temperature-dependent magnetization of PMs and by semi-iso-thermal condition of the HTS assembly.

The temperature of the top surface of HTS bulk in cryo-cooled SMBs may be different to the temperature of the cold head, due to the thermal resistance and time constant between the HTS bulk and the cold head. Measuring the temperature of the HTS surface facing rotating PM is challenging with conventional sensors due to limited mounting space, electromagnetic interference, and poor thermal insulation of electronic sensors. FBG sensors seem to be a potential solution for these issues. The implementation of FBG sensors in a cryo-cooled SMB environment was explained in this chapter. The data gathered by FBG sensor

during levitation force decay measurements showed a decrease in $\frac{\Delta\lambda}{\lambda_0}$ which was unlikely to be caused by thermal variation. Flux-pinning-induced tensile stress in the HTS bulk, whose amplitude was dependent on the sensor bonding method, was believed to be the source of $\frac{\Delta\lambda}{\lambda_0}$ decrease.

In this chapter, a significant phenomenon in SMBs and its relationship to HTS *E-J* characteristics was studied. It was shown that creep exponent, n-index, of HTS assembly in a superconducting bearing can be estimated non-destructively through levitation force relaxation experiments. This parameter is of great importance in simulating HTS electromagnetic behaviour. In the next chapter, AC loss phenomenon in SMBs will be explored, both analytically and experimentally. The analytical formulation of hysteresis loss and the impact of the periodicity of the magnetic field as well as the impact of the distribution of AC loss over the bearing surface will be investigated by using the experimental data gathered using the setups described in sections 3.3 and 3.7.

5

AC Loss in Superconducting Magnetic Bearings: Vertical Bearing

5.1 Introduction

AC loss mechanisms in bulk high-temperature superconductors have been studied since the discovery of HTS. Hysteresis loss as one of the main components of AC loss has been formulated from a macroscopic point of view based on Bean's critical state model. The main parameter in the hysteresis loss formulation is said to be magnetic field inhomogeneity. This chapter investigates other contributing parameters of the magnetic field such as periodicity and its distribution over the bearing surface, and introduces an updated formulation for hysteresis loss in SMBs. This chapter also covers the spin-down measurements performed in an actual rotating SMB, studies the relationship between magnetic field inhomogeneity and AC losses created in the SMB, and explores the impact of magnetic field inhomogeneity on the dynamic behaviour of the SMB. The design, build, and early spin-down measurement results of the experimental rig used in this chapter can be found in [157]. Extensive AC loss studies and results in this chapter have been published in [158].

5.2 Theory

Azimuthal inhomogeneity in the applied magnetic field has been said to be the main source of AC losses in SMBs [4]. This magnetic field inhomogeneity can cause two loss mechanisms to happen in SMBs, namely eddy current loss and hysteresis loss. The rotating inhomogeneous PM induces dissipative eddy currents in all conductive parts in its vicinity. On the other hand, the PM rotates in an inhomogeneous magnetic field trapped in the HTS bulk. This can induce eddy currents in conductive rare earth PMs. When an inhomogeneous magnet rotates above the HTS surface, the superconductor experiences a steady (DC) magnetic field with an alternating (AC) component [89]. This AC component can create

hysteresis loss, which according to the Bean model for a long superconducting disc in the critical state, can be analytically described as [72]:

$$Q = \frac{B_m^2}{2\mu_0}\left(\frac{2\beta}{3} - \frac{\beta^2}{3}\right) \quad \text{for} \quad \beta < 1 \tag{5.1}$$

$$Q = \frac{B_m^2}{2\mu_0}\left(\frac{2}{3\beta} - \frac{1}{3\beta^2}\right) \quad \text{for} \quad \beta > 1 \tag{5.2}$$

Where $\beta = \dfrac{B_m}{B_p}$, with B_m being the peak-to-peak amplitude of AC component of the magnetic field and $B_p = 2\mu_0 J_c r$ being the penetration field. For disks of finite length, equations 5.1 and 5.2 are multiplied by a geometry factor of the order of unity.

According to equations 5.1 and 5.2, the hysteresis loss in a SMB is not dependent on the rotational frequency of the bearing, but the periodicity of the magnetic field in one complete (2π) rotation has not been taken into account in these equations. In other words, the frequency of the AC component of the magnetic field (B_m) has been assumed to be $f_m = 1$. In order to take the magnetic field periodicity into account, the magnetic field of the PM was measured circumferentially by the magnetic field mapper described in section 3.3 along the Z-axis for $r = r_i$ mm to $r = r_f$ mm in 1.8° and 1 mm intervals along the azimuthal and radial directions, respectively. Discrete Fourier transform analysis was performed on $B - B_{mean}$ measured along each radius to derive the amplitude (A_i) and frequency (f_i) of its components. Using the Fourier transform results, equation 5.1 can be re-written as:

$$Q = \frac{1}{n_r}\sum_{r_i}^{r_f} Q_r \quad \text{with} \quad Q_r = \sum_i f_i \times \left(\frac{B_{mi}^2}{6\mu_0}(2\beta_i - \beta_i^2)\right) \tag{5.3}$$

where, Q_r is the hysteresis loss along each radius, n_r the number of radii along which the magnetic field has been measured, $B_{mi} = 2A_i$, and $\beta_i = \dfrac{B_{mi}}{B_p}$. The total inhomogeneity of the PM, ϕ, is given by:

$$\phi = \frac{\sum_{nr} 2A_{max,r}}{n_r} \tag{5.4}$$

Where, $A_{max,r}$ is the maximum component of the magnetic field measured along each radius.

As a first-order approximation, the frequency of the magnetic field along each radius can be assumed as $f_m = 1$ and the peak-to-peak ΔB along each radius can be taken as B_m. Applying these assumptions, equations 5.3 and 5.4 can be written as:

$$Q = \frac{1}{n_r}\sum_{r_i}^{r_f} Q_r \quad \text{with} \quad Q_r = \frac{\Delta B_{r(p-p)}^2}{6\mu_0}\left(2\beta_r - \beta_r^2\right) \tag{5.5}$$

$$\phi = \frac{\sum_{nr} \Delta B_{r(p-p)}}{n_r} \tag{5.6}$$

where, $\Delta B_{r(p-p)}$ is the peak-to-peak amplitude of the AC component of the magnetic field measured along each radius, and $\beta_r = \frac{\Delta B_{r(p-p)}}{B_p}$.

The best PMs have been reported to have an AC component of almost 1% of the average field at a fixed radius above the rotating surface [4]. This magnetic field inhomogeneity acts as a drag force on the rotating body in a superconducting bearing, causing a gradual deceleration. The stored energy in the rotating PM is given by:

$$E = \frac{1}{2} I \omega^2 \tag{5.7}$$

where $I = mR_\gamma$ is the moment of inertia, $\omega = 2\pi r f$ is the angular velocity. Here, m is the mass of rotor, R_γ is the radius of gyration, and f is the rotational frequency. The energy loss per cycle is given by:

$$P_{cycle} = -\frac{1}{f}\frac{dE}{dt} = -2mR^2\pi^2\frac{df}{dt} \tag{5.8}$$

Here, R is the outer radius of the rotor.

Equations 5.1, 5.3, and 5.5 can be used to calculate the hysteresis loss per cycle per unit volume. According to equation 5.8, the AC loss (hysteresis loss + eddy current loss) per cycle in a superconducting bearing can be determined by measuring the deceleration rate (df/dt) of the freely spinning PM.

The coefficient of friction (COF), which characterises the deceleration rate of the rotating PM, has been used as a figure of merit when studying rotational loss in SMBs and is given by [58]:

$$COF = \frac{F_D}{F_L} = -\frac{2\pi R_\gamma^2}{g R_D}\frac{df}{dt} \tag{5.9}$$

where, F_D is the drag force, F_L is the levitation force, R_γ is the radius of gyration, g is the acceleration due to gravity, and R_D is the mean radius at which the drag force acts. R_D has been usually taken to be the outer radius of the rotating part of the SMB, because the AC loss mechanism and its distribution over the bearing radius has not been fully explored [4, 58].

5.3 Experimental Evaluation

AC losses in HTS bulks have been studied before, but only a few reports are directly related to an actual superconducting bearing environment, where a PM rotates freely in the vicinity of an HTS assembly. In order to study the relationship

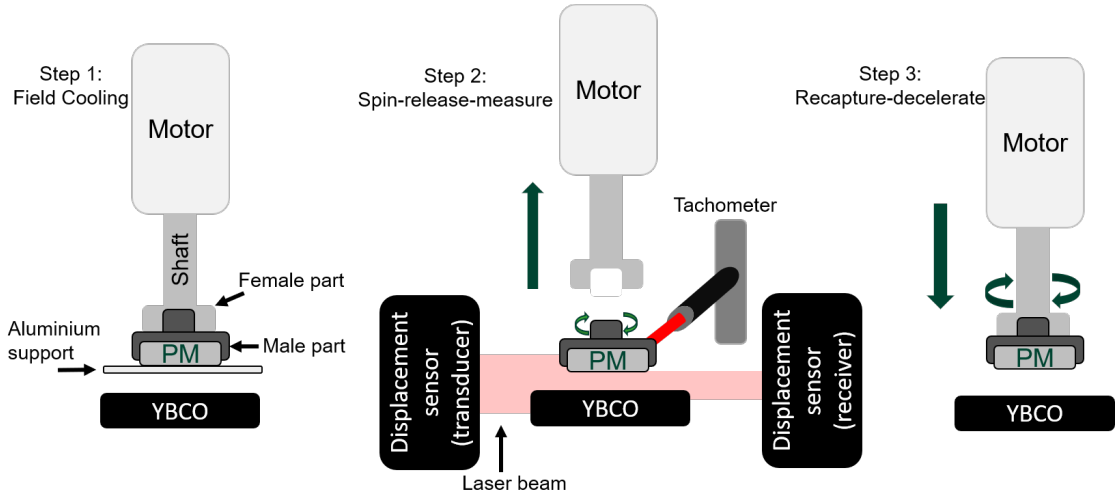

Figure 5.1: Spin-down experiment steps.

between AC losses and magnetic field inhomogeneity of the PM, spin-down tests were performed in the vertical levitation rig described in section 3.7 with 6 PMs of different levels of inhomogeneity.

Figure 5.1 shows the experiment steps. First, the PM was placed on the aluminium support and was coupled to the shaft. The male and female sides of the PM coupling slid and mated due to their chamfered structure. Next, both vertical linear stages moved the aluminium support and the driving system towards the HTS bulk, at a common velocity, to the cooling height. The HTS was then cooled down to the desired temperature with the PM in its vicinity (FC condition). In the next step, the support was moved down and then aside, allowing the driving motor to be spun up. After reaching the desired speed, the motor and the shaft were moved upward and released the PM to be freely levitated and rotating above the superconductor. The rotation speed of the PM decreased gradually due to AC losses. During the spin-down period, rotation speed, vibrations, and temperature were measured and recorded. Once the experiment was complete and the PM was stopped, the aluminium support was moved back into position between the PM and the HTS bulk. This coupling mechanism allows the user to change the speed of the PM or to stop it at a certain speed. For this purpose, the motor speed can be adjusted to just below that of the spinning PM, then the coupling mechanism can be moved downward slowly. When the male and female parts of the PM coupling mate, the PM rotation speed can be decreased or increased to another spinning rate by changing the motor speed.

5.4 Results and Discussion

The magnetic field of the PMs was measured circumferentially by the magnetic field mapper described in section 3.3 along Z-axis for $r = 1$ mm to $r = 12$ mm in 1.8° and 1 mm intervals along azimuthal and radial directions, respectively. All PMs were N45-grade *NdFeB*, 17 mm in diameter and 10 mm thick. The vertical separation between the PM and the Hall sensor was 2.7 mm, equal to the vertical separation between the PM and the HTS bulk during spin-down measurements. Figure 5.2 shows the magnetic field of PM number 6 measured along 12 discrete radii, and the associated Fourier analysis. A threshold of 1×10^{-4} T was defined to determine the data points that contribute to equation 5.3. Because of the 3^{rd} and the 4^{th} power of B_{mi} in equation 5.3, the contribution of components with amplitudes smaller than the threshold is negligible. The same technique was applied to all magnets. Figures of the magnetic field of magnets 1 to 5 and their associated Fourier transform analysis are presented in appendix A.

In order to compare AC loss measurements with analytical values, equations 5.1, 5.3, and 5.5 were used to calculate hysteresis loss from magnetic field inhomogeneities, and equation 5.8 was used to calculate AC loss from deceleration rates below resonance, because AC losses in SMBs are mainly dominated by hysteresis loss below the resonance frequency of the rigid body. AC losses measured below resonance were used because AC losses above resonance are believed to be influenced by additional factors excited by external vibrations. In this comparison, the value of $J_c = 6.46 \times 10^7$ A/m^2, estimated from levitation force decay measurements, was used to calculate B_p (see section 4.3). Figure 5.3 shows the AC loss measured in spin-down tests below resonance frequency in comparison with hysteresis loss calculated with equations 5.1, 5.3, and 5.5. In figure 5.3a, PM inhomogeneities on the X-axis were considered as the maximum peak-to-peak ΔB_i.

In all graphs, experimental values are in a good agreement with those calculated analytically, but the order of magnets on the graphs varies because the values of inhomogeneity are not the same. In 5.3a, the theoretical values are larger than the experimental data points for PM6, PM5, and PM3. This is inconsistent with the nature of spin-down experiments. Other factors of magnetic field inhomogeneity (radial (ΔB_r) and vertical (ΔB_z)) are involved by the experimental procedure and contribute to the total loss, whereas in analytical calculations these factors are ignored and only the azimuthal magnetic field inhomogeneity has been considered. As a result, the experimental data points are more likely to be larger than theoretical values. Furthermore, equation 5.1 does not completely capture the physics of

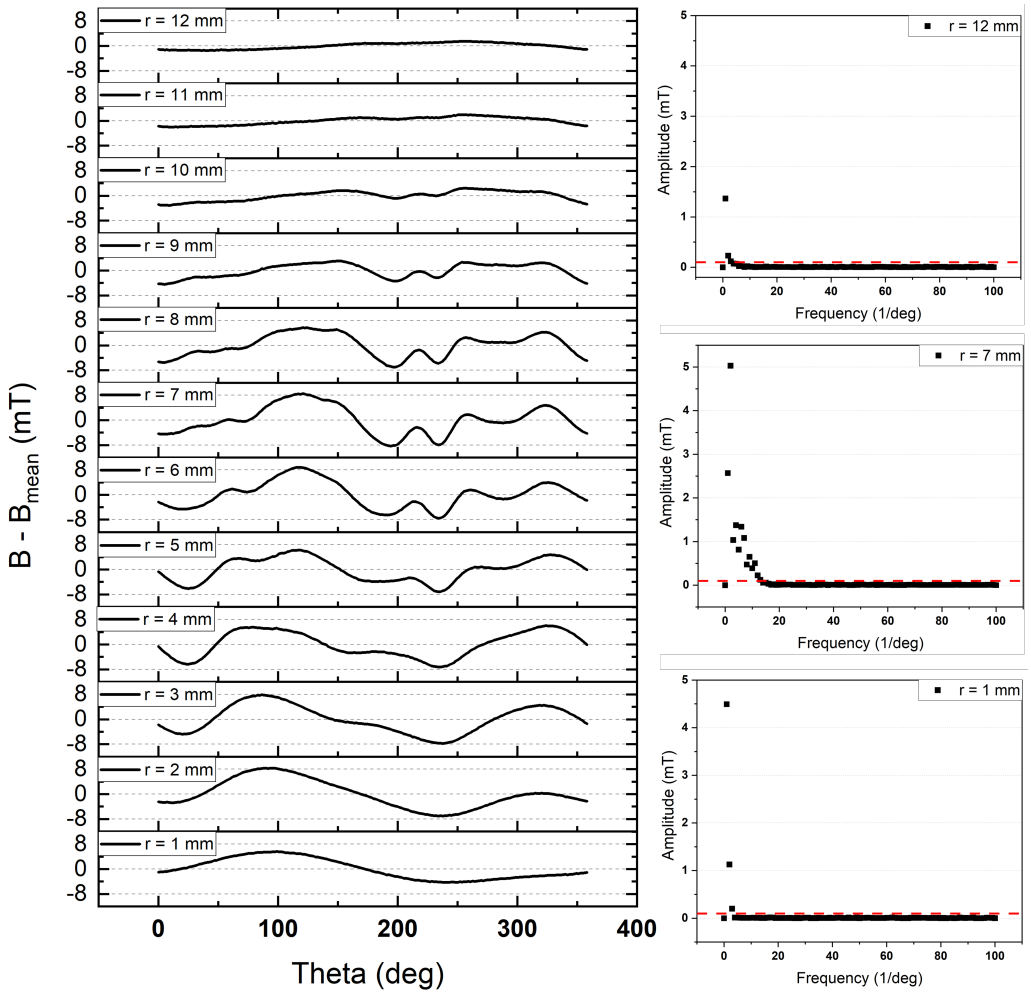

Figure 5.2: Left: magnetic field (in the Z-direction) of PM6 measured azimuthaly over its surface with r= 1 mm being the innermost radius. Radius of the magnet is 8.5 mm. Right: the discrete Fourier transform of $B - B_{mean}$ over three radii. The red dashed line indicates the 1×10^{-4} T threshold, above which the data points are included in equation 5.3.

hysteresis loss because it ignores the periodicity of the magnetic field and the distribution of the magnetic field inhomogeneity over the surface of the bearing. In figures 5.3b and 5.3c, however, all experimental data points are larger than theoretical values, which is consistent with the physics and nature of the experiments. In figure 5.3b, although PM6 has the lowest inhomogeneity level, it generates a larger AC loss than PM4 and PM1. This can be explained by equation 5.3 which captures the physics of hysteresis loss by considering the impact of magnetic field periodicity and the distribution of AC loss over the surface. PM6 shows that a magnet with a smaller level of inhomogeneity, but a more periodic magnetic field, can generate a larger AC Loss. Figure 5.3c shows that equation 5.5 which is the

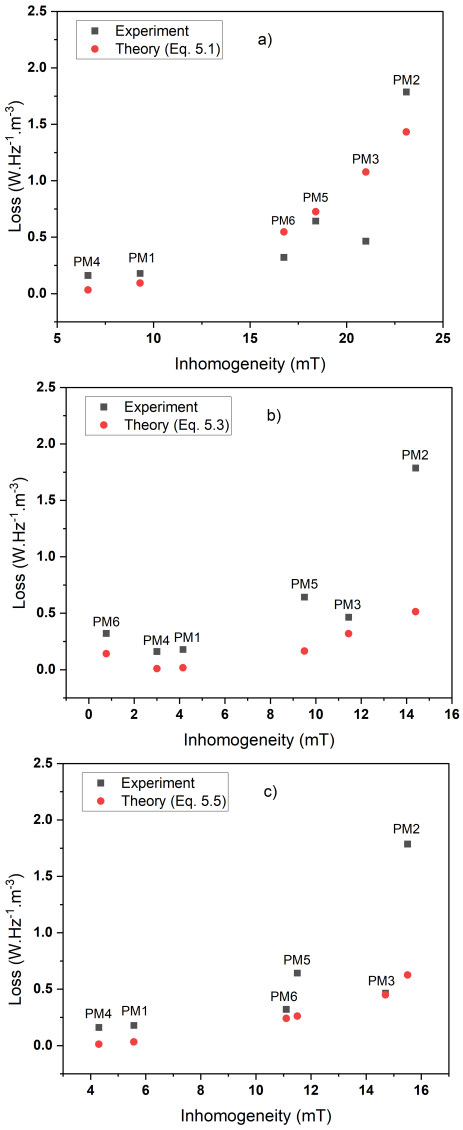

Figure 5.3: AC loss generated in an HTS bulk 28 mm in diameter and 10 mm thick versus magnetic field inhomogeneity calculated analytically and measured in spin-down experiments.

first order approximation of equation 5.3, can still provide an acceptable prediction of AC loss by only considering the distribution of magnetic field inhomogeneity.

The largest discrepancy is seen for PM3 and PM2 in figure 5.3a, but this discrepancy happens for PM2 and PM5 in figures 5.3b and 5.3c. Considering the more comprehensive definition of hysteresis loss by equations 5.3 and 5.5, the discrepancy for PM3 in figure 5.3a can be caused by equation 5.1 itself. The discrepancy for PM2 and PM5 in figures 5.3b and 5.3c, however, might be caused by the challenging experimental procedure and the PM coupling system.

Figure 5.4 shows the COF as a function of rotational frequency for the 6 PMs of the same size but with different levels of inhomogeneity. PM5 could not be released

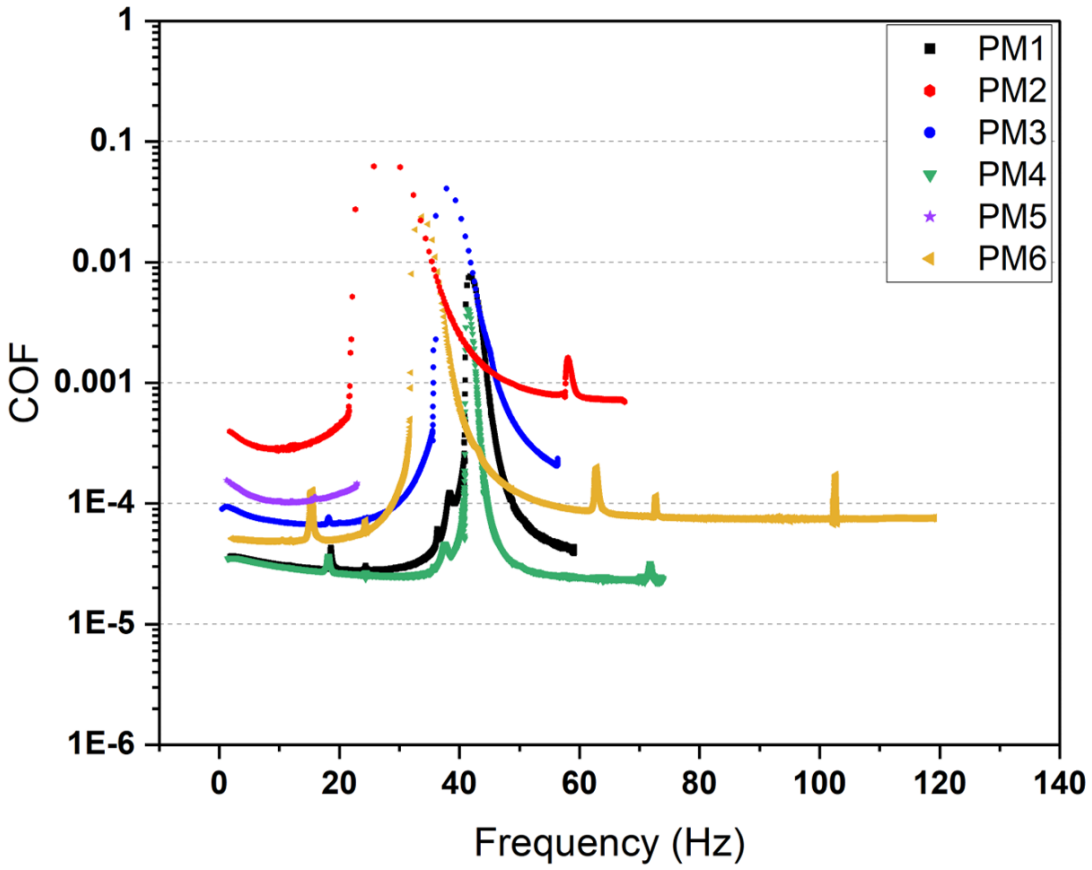

Figure 5.4: COF versus rotational frequency for 6 PMs of the same size but with different levels of inhomogeneity. The separation between PM and HTS was 2.7 mm.

at frequencies well above the resonance frequency, due to coupling imbalance and vibrations at higher frequencies. Comparing figure 5.3 and figure 5.4, it can be seen that although PM3 generates a larger loss by all definitions (equations 5.1, 5.3, and 5.5), it has a smaller COF than PM5. This can be explained by the definition of COF. In COF calculations R_D is usually taken as the outer radius of the rotating PM [4, 58]. This assumption simply ignores the distribution of inhomogeneity and AC loss over the surface of the PM. Figure 5.5 shows the hysteresis loss distribution over PM3 and PM5 surface calculated by equations 5.3 and 5.5. This figure shows that the distribution of hysteresis loss is more towards the center of PM3, whereas it is more towards the outer radius of PM5.

The radius of drag force, R_D, is given by [159]:

$$R_D = \frac{\sum r_i \Delta B_i^3}{\sum \Delta B_i^3} \tag{5.10}$$

where, r_i is the i^{th} radius over which the magnetic field is measured circumferentially, and ΔB_i is the peak-to-peak AC component of magnetic field over radius r_i. This

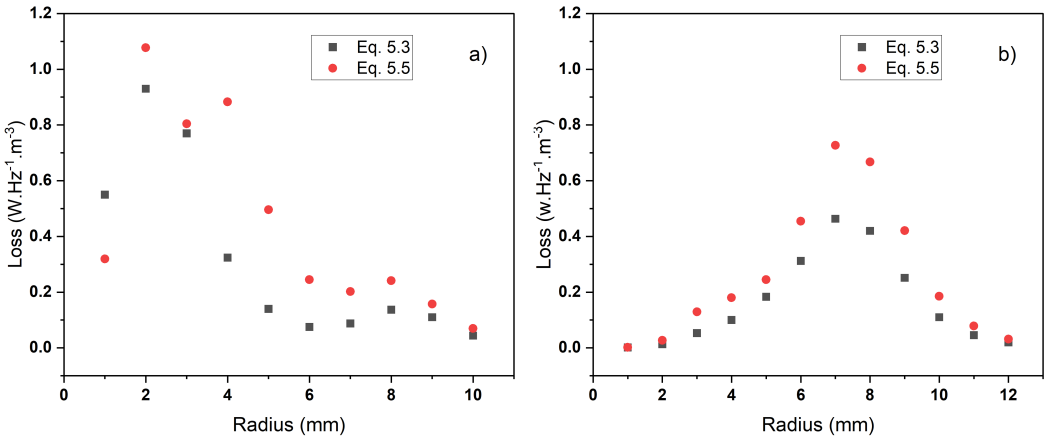

Figure 5.5: Hysteresis loss distribution over the surface of PM3 (a) and PM5 (b) calculated by equations 5.3 and 5.5.

equation is also missing the periodicity of the magnetic field over radius r_i. In order to take the periodicity of the magnetic field into account, equation 5.10 can be updated by using equation 5.3 as:

$$R_D = \frac{\sum r_i Q_i}{\sum Q_i} \tag{5.11}$$

where Q_i is the hysteresis loss over r_i calculated by equation 5.3. Figure 5.6 shows the COF values calculated by using the updated values of R_D. As can be seen, by taking the AC loss distribution and magnetic field periodicity into account, the COF curves are updated in an order matching the AC loss order shown in figure 5.3.

The dynamic behaviour shown in figure 5.6 has been widely reported for disc shaped SMBs [4]. The COF shows a major resonance behaviour in all cases and is almost independent of rotational frequency below and above the resonance region. This main resonance mode has been said to be the radial resonance frequency for disc shaped bearings [4]. The large COF value in the resonance region is due to radial vibrations of large amplitude. The COF is generally larger at frequencies above resonance than below resonance. This can be explained by the transition of the center of rotation. Below resonance the PM rotates around its center of magnetism (or center of geometry), and above resonance, it rotates around its center of mass. This can add a radial factor to magnetic field inhomogeneity [4]. Other vibration modes can be induced by the coupling mechanism which consequently add to the hysteresis loss. As can be seen in PM2, PM4, and PM6 graphs, the COF is mostly independent of frequency below and above the resonance region. In all graphs, a slight increase in the COF was observed below the resonance region at very low frequencies which might be caused by cogging torque created by magnetic field inhomogeneity [159].

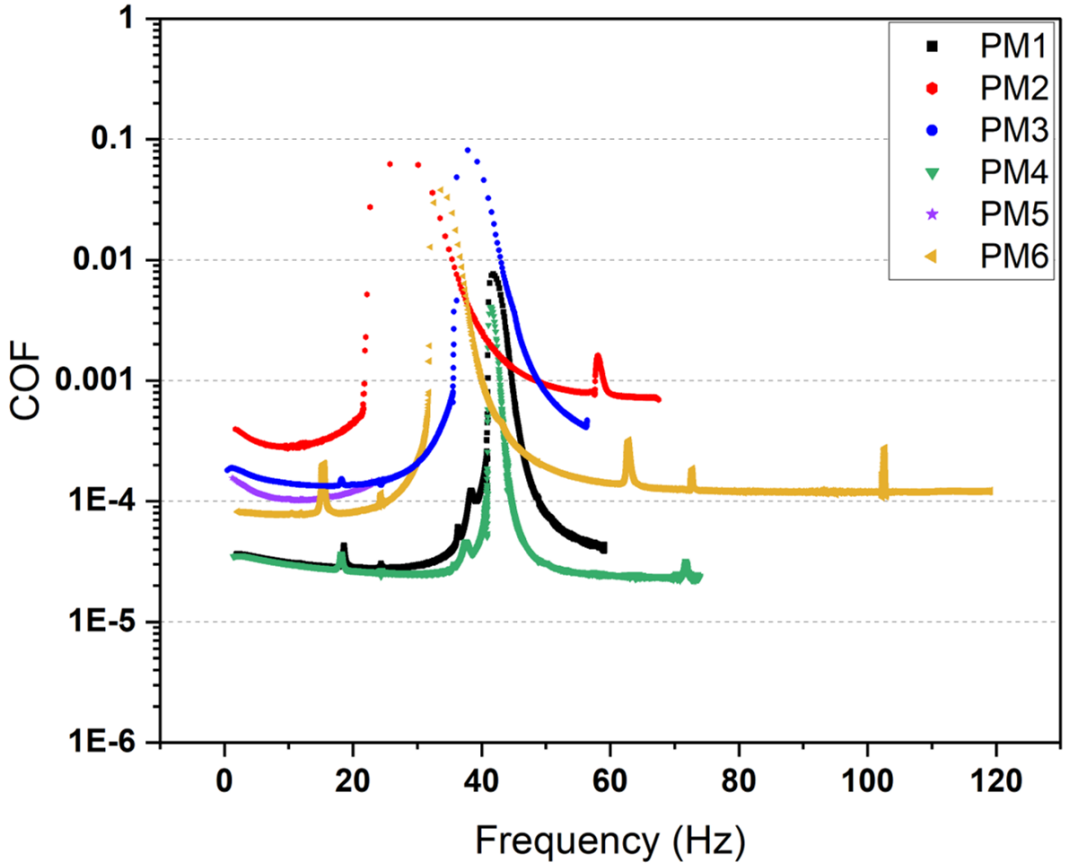

Figure 5.6: COF versus rotational frequency updated by using equation 5.11 to calculate R_D values.

As shown in figure 5.6, the resonance region widens and the peak rotational frequency decreases with AC loss generated by the magnets. This means that the bearing dynamic stiffness, which is related to the resonance frequency by $K = m\omega_n^2$, decreases with magnetic field inhomogeneity. Here, m is the mass of the rotor, $\omega_n = 2\pi f_n$ is the resonance angular velocity, and f_n is the resonance frequency. The larger the inhomogeneity, the deeper the AC component penetrates into the HTS bulk and the more flux lines are influenced. This AC component helps flux lines escape from pinning centers which in turn decreases bearing stiffness. This is consistent with the work reported in [160], [161], and [162] where the resonance frequency of a levitated PM was found to be inversely proportional to the amplitude of excited vibrations. Lower levels of inhomogeneity can result in higher stiffness, but passing through higher resonance frequencies in practical applications requires extra safety measures. Other local peaks can be observed (mainly 15 Hz – 20 Hz, and 70 Hz – 80 Hz regions) in the COF graphs which might be attributed to vertical, whirling, and other modes of motion excited externally. PM6 shows more local

resonance modes than the other magnets. These modes might have been excited by external vibrations during an imbalanced release process.

5.5 Summary

AC losses in superconducting magnetic bearings are said to be generated by magnetic field inhomogeneity. Analytical models based on the Bean model for the critical state have been developed to calculate AC losses at low frequencies in superconducting bulks. However, these models do not take the magnetic field periodicity, nor the distribution of AC loss into account. Furthermore, no data has been reported about the relationship between AC losses and magnetic field inhomogeneity in an actual superconducting bearing environment. In this chapter, the analytical hysteresis loss model in HTS bulks was updated which, now, takes the distribution of AC loss and the frequency of the magnetic field during one complete rotation into account. The relationship between magnetic field inhomogeneity and AC loss was studied experimentally in spin-down measurements by using permanent magnets of the same size but with different levels of inhomogeneity. The results show that the relationship measured experimentally was consistent with the updated analytical calculations. The data reported in this chapter also reveals a relationship between magnetic field inhomogeneity and the dynamic behaviour of the superconducting bearing. The resonance region widens and the resonance frequency of the rigid body, and hence the bearing stiffness, decreases with inhomogeneity. This is of further importance when designing and building superconducting bearings for practical applications.

In the next chapter, the high-speed spin-down experiment performed in [64] will be repeated with some improvements in the experimental setup. The main purpose of this replication is to design, build and test a prototype high-speed motor/generator for projects being currently developed in New Zealand. Furthermore, the AC loss mechanism at kHz-rated rotational frequencies will be discussed in the next chapter.

6

AC Loss in Superconducting Magnetic Bearings: Horizontal Bearing

6.1 Introduction

The contactless motion and the ability to overcome speed limits have attracted attention to high-speed applications of SMBs. High-speed spin-down measurements (deceleration rate) in actual bearings and their relationship with rotational frequency widens our understanding about the AC loss mechanism in HTS bulks, which is of crucial importance when designing SMBs for high-speed applications. Studied in this chapter is a kHz-rated benchtop motor/generator demonstration where a pair of SMBs are employed to levitate the shaft in a horizontal configuration.

6.2 Theory

As predicted by the Bean model, AC losses in superconducting bearings show no rotational frequency dependence at low rotational frequencies where AC losses are mainly dominated by hysteresis losses. Studies, however, show that rotational frequency dependent terms appear in AC loss measurements at rotational speeds well above the rigid body resonance frequencies. This behaviour, which can be explained by magnetic diffusion phenomenon, has been observed in both deceleration rate measurements [64, 96] and AC susceptibility measurements [89, 96].

6.3 Experimental Evaluation

The horizontal bearing setup described in section 3.8 was used as a prototype motor/generator demonstration to prove the principle of application of high-temperature superconductor magnetic bearings in electrical machines. Several test runs were first performed in a benchtop bell jar vacuum chamber to examine the driving and control systems. Having validated the design, spin-down tests were performed in the vacuum chamber setup.

In order to increase the air gap between levitation PMs and HTS bulks, another rotor with the same configuration as described in section 3.8.1 was built. The airgap

was increased to avoid mechanical friction between the shaft and HTS bulks. The new rotor shaft was 2 mm shorter in length. The air gap between each HTS bulk and its associated levitation PM was adjusted to 1 mm for the 148 mm shaft and 2 mm for the 146 mm shaft. The shafts, the HTS bulks, and the stator were aligned axially with an accuracy of 10 μm. Air drag was minimized by performing the experiment at a pressure of approximately 1×10^{-6} mbar. The temperature of the HTS bulks was controlled at 60 K for the 148 mm shaft, and at 59 K for the 146 mm shaft. At operating temperature, the shaft supports were removed and speed was controlled using a PWM signal generated by a commercial controller and *LabVIEW* software.

6.4 Results and Discussion

A challenging issue was to cool the HTS bulks in the vacuum chamber. The cryogenic performance of the flexible thermal link described in section 3.8.3 is shown in figure 6.1. According to the data provided by the manufacturer, the cryocooler provides $\approx$ 12 W of cooling power at 60 rpm at the minimum coldhead temperature of 31 K. Heat flux for a homogeneous, isotropic solid whose thermal conductivity is independent of direction is given by Fourier's law [163]:

$$\mathbf{q} = -k\nabla T \tag{6.1}$$

where $\mathbf{q}$ is heat flow per unit volume, ∇T is temperature gradient, and k is thermal conductivity. For the flexible thermal link equation 6.1 can be written as:

$$P = \frac{kA\Delta T}{l} \tag{6.2}$$

where P is the heat flow rate, A is the material cross section, and l is the path length. According to the temperature difference between the cryocooler coldhead (31 K) and the HTS bulks (55 K) shown in figure 6.1, $\approx$ 5 W of heat power was transferred by the thermal link. The rest of the heat load (12 W $-$ 5 W $=$ 7 W) could be generated by radiation.

Spin-down experiments were performed on both shafts to study the AC loss in SMBs at high rotational frequencies. At a rotational frequency of 1916 Hz, mechanical friction was observed between the shafts and stator, so the rotational frequency was not increased beyond this level. This maximum rotational frequency is 130 Hz faster than that achieved by Hull *et al.* [64]. This horizontal bearing setup is believed to be the fastest superconducting bearing made in New Zealand. The rotational frequency was then decreased to 1500 Hz to avoid friction. Figure 6.2 shows the spin-down results for both shafts from $\approx$ 1.5 kHz. At this rotational

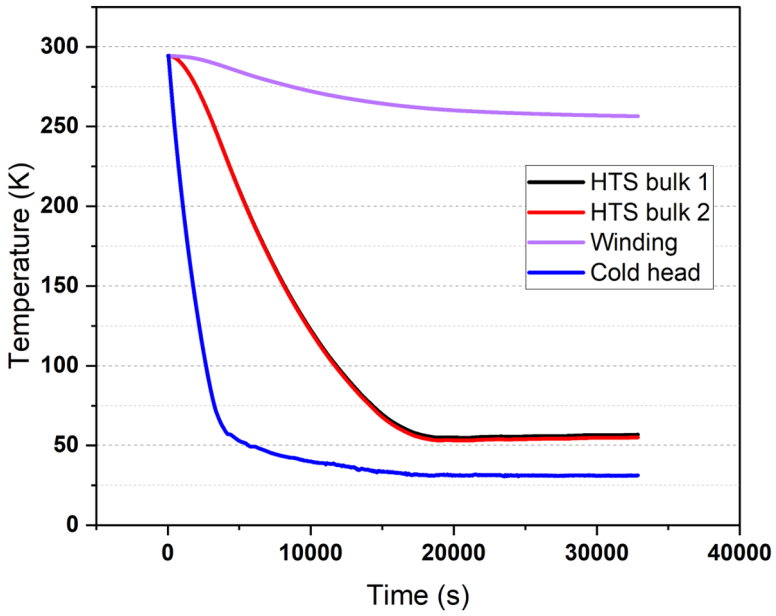

Figure 6.1: Temperature of HTS bulks, stator winding, and coldhead versus time during cool down from room temperature. The pressure inside the vacuum chamber was of the order of 10^{-6} mbar.

frequency, the stator windings were switched into open circuit mode and the rotational frequency of each shaft was recorded as a function of time. The output power of the prototype motor is given by:

$$P = \tau\omega \tag{6.3}$$

where τ is the axial torque and $\omega = 2\pi f$ is the angular frequency of the shaft. At $f =$ 1500 Hz, the mechanical power of the motor was ≈ 3 W. This operational frequency was maintained with an input voltage of 12 V at a duty cycle of 0.5 and phase current of 0.18 A rms, which provided ≈ 3.24 W of input power. Considering the phase resistance of $0.2\,\Omega$ and wiring resistance of $0.3\,\Omega$, the power dissipated by Joule heating in the stator windings and cables was 0.02 W and 0.03 W, respectively. The remaining power loss might have occurred in the switching circuit of the controller.

The magnetic field of the levitation PMs embedded in the shafts used in spin-down experiments (see table 3.2) was measured circumferentially by the magnetic field mapper described in section 3.3 along Z-axis for $r = 1$ mm to $r = 10$ mm in 1.8° and 1 mm intervals along azimuthal and radial directions, respectively. The separation between the magnet surface and the Hall probe was set at 3 mm due to physical limitations of the setup. Figures 6.3 and 6.4 show the $B - B_{mean}$ measured over the levitation magnets of the 146 mm shaft and the 148 mm shaft, respectively. Discrete Fourier transform was performed and a threshold of 1×10^{-4} was applied to

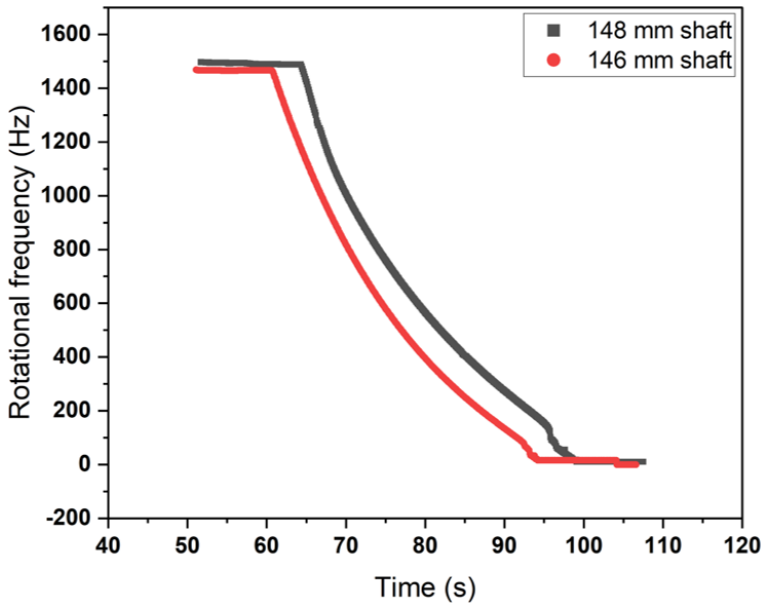

Figure 6.2: Rotational frequency of the two rotors as a function of time.

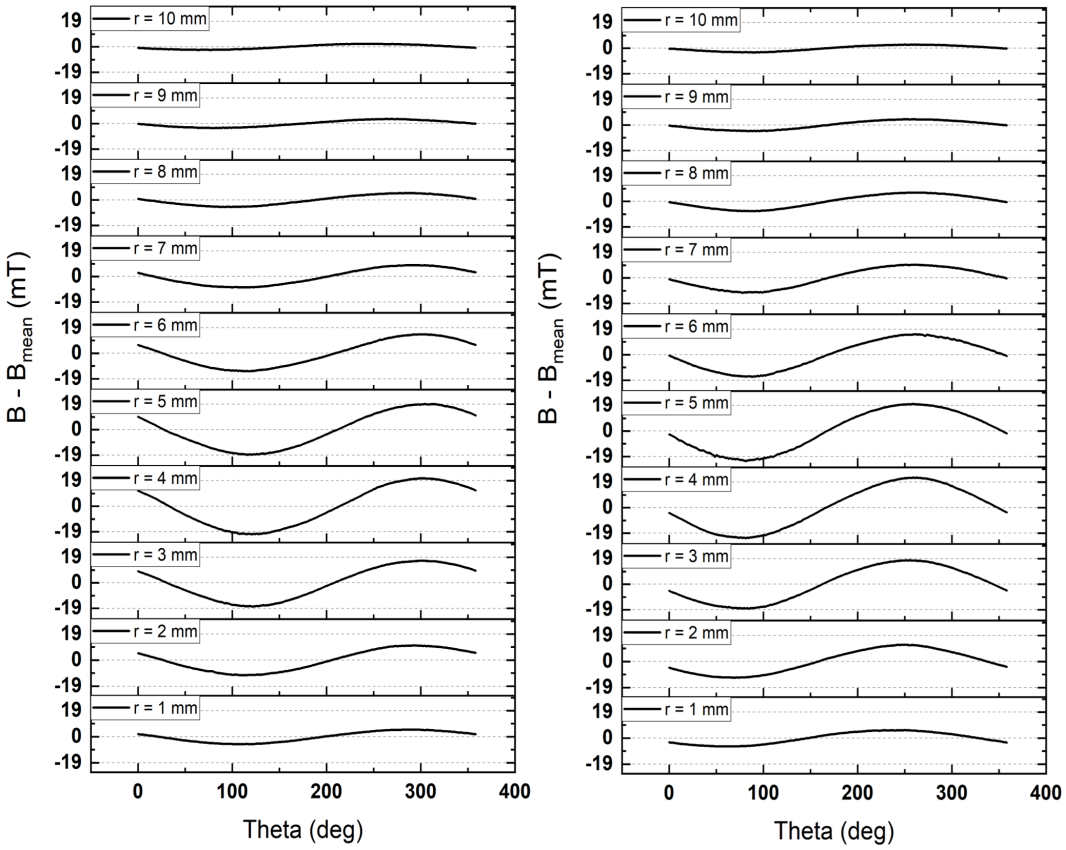

Figure 6.3: Magnetic field (z-axis) of the levitation magnets used in the 146 mm shaft. The field was measured circumferentially at a distance of 3 mm above the magnets.

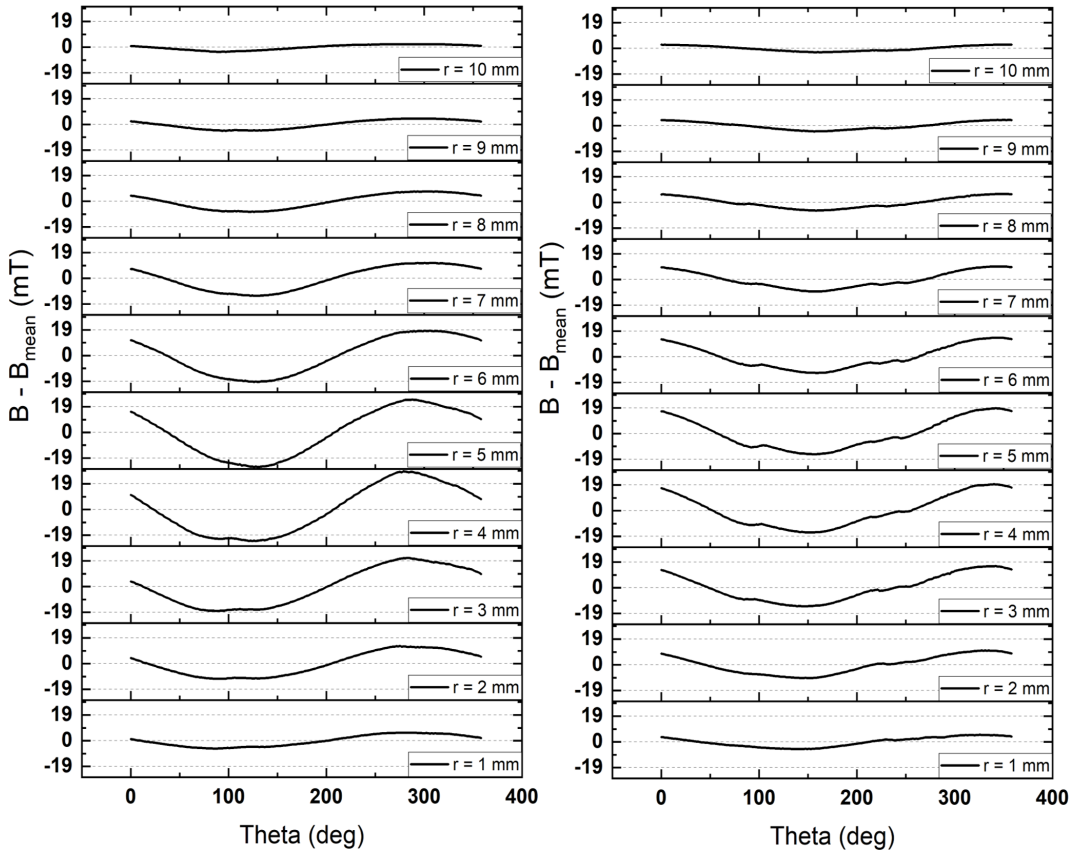

Figure 6.4: Magnetic field (z-axis) of the levitation magnets used in the 148 mm shaft. The field was measured circumferentially at a distance of 3 mm above the magnets.

determine the components that contribute to AC loss and inhomogeneity calculations. The magnetic field inhomogeneity of the PMs in the 148 mm shaft was 27 mT and 17.25 mT, and for those in the 146 mm shaft was 18 mT and 20.5 mT. These numbers were calculated from equation 5.4.

The deceleration rate of the shafts is shown in figure 6.5. A detailed analysis of AC losses in these experiments is complex, because two superconducting bearings with two different levels of inhomogeneity are mechanically coupled through a shaft and contribute to the total AC losses. However, some noticeable behaviour can be seen in the graphs. Both graphs show a resonance behaviour at low rotational frequency, with the resonance frequency of the 148 mm shaft being almost twice as large as that of the 146 mm shaft (shown in figure 6.6). This can be explained by the airgap between the levitation PMs and HTS bulks, which is 1 mm for the 148 mm shaft and is 2 mm for the 146 mm shaft. At a smaller airgap, more flux lines are pinned in the HTS bulks, which increases the bearing stiffness. The larger the stiffness, the larger the resonance frequency.

In both experiments, apart from near resonance, the deceleration rate is independent of rotational frequency up to $\approx$ 250 Hz for the 148 mm shaft, and

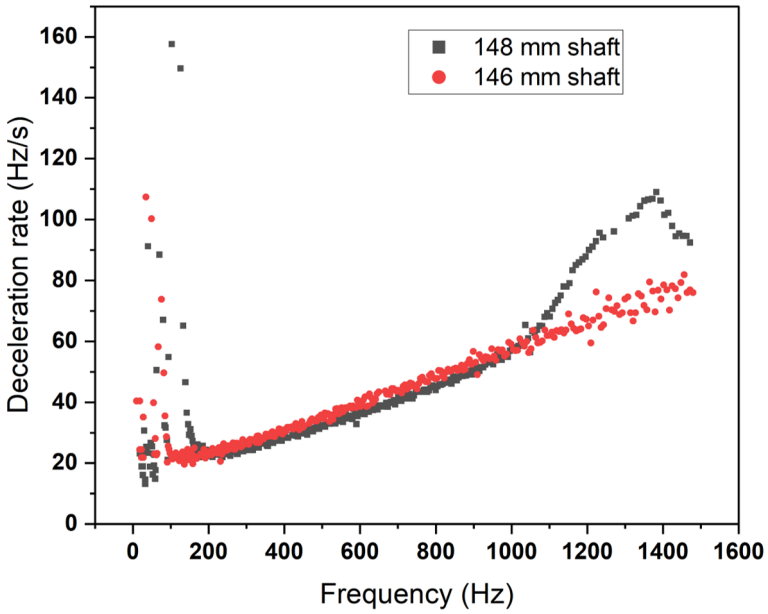

Figure 6.5: Deceleration rate of the two shafts versus rotational frequency.

$\approx$ 125 Hz for the 146 mm shaft. This is because in that region, losses are mainly dominated by hysteresis loss intrinsic to HTS bulks. Deceleration rates below and above resonance are almost equal in both experiments, which can be attributed to an accurately balanced rotor [4]. The deceleration rate increases gradually with rotational frequency and reaches a peak which is followed by a decrease for the 148 mm shaft. This behaviour is consistent with what has been reported for high frequency measurements [64, 89, 96] and will be discussed presently. For the 146 mm shaft, however, the peak in deceleration rate was not observed up to 1500 Hz.

The dependence of the deceleration rate on rotational frequency can be explained by flux line motion in HTS bulks. As frequency increases, HTS bulks experience a variation in the applied magnetic field, caused by the intrinsic azimuthal inhomogeneity of the magnets. This AC magnetic field induces an electric field, $\boldsymbol{E}$, whose magnitude is dependent on frequency and can make flux lines escape from their pinning sites in the HTS bulks. This electric field creates dissipative normal currents in an eddy-current-like mechanism, and drives HTS bulks from the flux creep regime ($E < E_c$) to the flux flow regime ($E > E_c$) (see figure 6.7).

From Maxwell's equations:

$$\nabla \times \mathbf{E} = -\frac{\partial \mathbf{B}}{\partial t} \tag{6.4}$$

$$\nabla \times \mathbf{B} = \mu_0 \mathbf{J} \tag{6.5}$$

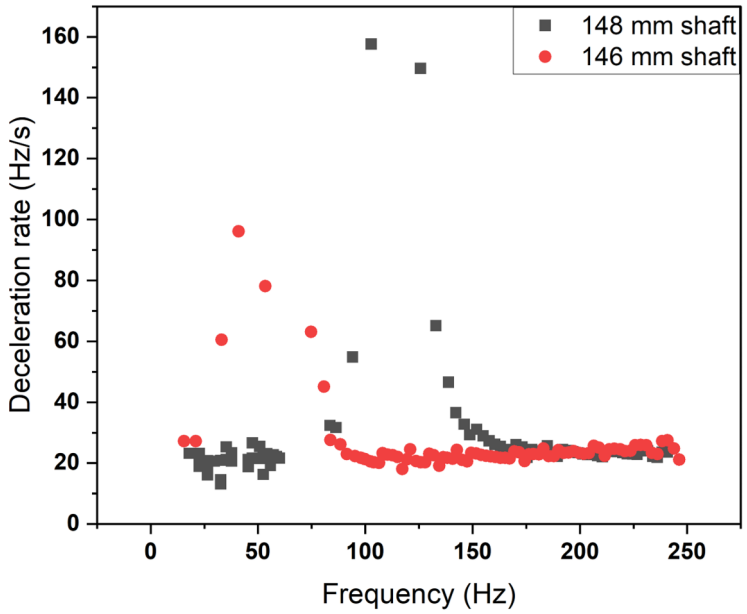

Figure 6.6: Deceleration rate of the two shafts at low rotational frequency. The deceleration rate increases in the resonance frequency region.

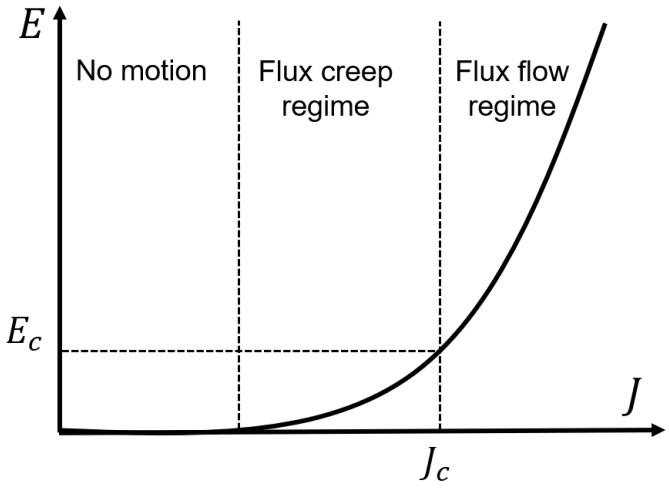

Figure 6.7: Qualitative representation of E-J relationship in a typical type-II superconductor showing the flux creep and flux flow regimes.

and assuming a power-law ***E*-*J*** relationship, the following equation of non-linear magnetic diffusion in superconductors can be derived:

$$\nabla \times (\rho \nabla \times \mathbf{B}) = -\mu_0 \frac{\partial \mathbf{B}}{\partial t} \tag{6.6}$$

where $\rho(\mathbf{J})$ is given by:

$$\rho = \frac{E_c (J/J_c)^n}{J} \tag{6.7}$$

For a slab of width $2a$ along the x-axis and infinitely long in the y and z directions, equation 6.6 can be written as:

$$\frac{\partial}{\partial x}(D_m \frac{\partial B_z}{\partial x}) = \frac{\partial B_z}{\partial t} \tag{6.8}$$

Where D_m is the magnetic diffusion coefficient and is given by:

$$D_m = \frac{\rho(J)}{\mu_0} \tag{6.9}$$

According to the theory of magnetic diffusion in type-II superconductors, as frequency increases, the penetration depth decreases to a thin region near the surface of the HTS bulk [164]. The penetration depth (skin depth) is given by [164]:

$$\delta = \sqrt{2D_m/\omega} \tag{6.10}$$

Equation 6.10 is highly nonlinear because of the strong dependence of ρ on current density, temperature, and magnetic field in single-domain high-temperature superconductors. Since the HTS bulks were pushed into the flux flow regime, AC losses would be in the form of Joule heating ($\propto \rho \boldsymbol{J}^2$). This AC loss would result in a temperature gradient across the HTS bulk due to the finite specific heat and thermal conductivity of YBCO. In the spin-down experiments reported in this chapter, however, the temperature of the bulks was continuously monitored and controlled at a constant set point. This means the cryogenic system had enough time to remove the heat generated in HTS bulks, especially in the regions near their circumference. As a result, the flux flow resistivity and hence the magnetic diffusion coefficient can be considered constant in these experiments. At the peak frequency ($1382Hz$) of the 148 mm shaft, the skin depth δ is $\approx$ 4.3 mm, which is almost the radius with the maximum ΔB, over which the AC component of the applied magnetic field acts. Beyond this frequency, the magnitude of the shielding currents become large enough to prevent AC magnetic fields from penetrating the bulk, and the skin depth becomes smaller [64, 164–167]. As a result, the deceleration rate which is a measure of AC losses in SMBs, decreases with frequency.

A similar loss mechanism can happen in conductive PMs. The magnetic field trapped in superconductors may be inhomogeneous due to magnetic field inhomogeneity of the PMs and/or structural impurities of the HTS bulk lattice [89]. When the conductive *NdFeB* PM rotates in the magnetic field trapped in the superconducting bulk, it experiences an AC field component which can cause a similar eddy-current-like loss mechanism in the PM. Rare earth PMs have shown metallic behaviour in AC susceptibility measurements, but their peak frequency is in the order of 10^4 Hz due to their poor electrical conductivity [89].

6.5 Summary

The principle of application of high-temperature superconducting magnetic bearings for high-speed motors/generators was proved by designing, building, and testing an experimental rig. The maximum rotational frequency achieved by Hull *et al.* [64] was increased to a new record of 1916 Hz, which is believed to be the fastest superconducting bearing made in New Zealand. A rotational frequency of 1500 Hz was maintained with an input power of 3.24 W. The cryogenic performance of a flexible thermal link was evaluated. It proved to be capable of removing excessive Joule heating created at kHz-rated operational frequencies. Spin-down measurements performed on two shafts showed that at higher rotational frequencies, well above the resonance frequency of the rigid body, another mechanism of AC loss is present which cannot be explained by the Bean critical state model. At higher rotational frequencies, although hysteresis loss still exists, AC losses are mainly dominated by an eddy-current-like mechanism and are dependent on rotational frequency, which can be explained by nonlinear magnetic diffusion in high temperature superconductors.

7 Conclusion & Future Work

7.1 Conclusion

High-temperature superconducting bearings seem to be a potential solution to speed limits imposed by conventional bearings in rotating machinery. Although SMBs have significant advantages over mechanical bearings, there are some issues that should be addressed, among which the relaxation of levitation force and AC loss mechanisms are of great importance.

7.1.1 Levitation Force Decay

Levitation force decay measurements allow the nonlinear E-J characteristics to be identified in HTS bulks non-destructively. This non-destructive method was developed by linking a FE model of levitation force with a simple flux creep model, allowing the superconducting critical current and flux creep exponent (n) to be extracted from a physical measurement of levitation force. The deviation between the actual and extracted n-indexes was found to be a function of the amount of field penetration experienced by the superconductor. This technique was applied to a disc-shaped thrust SMB and a flux creep exponent between 40 and 60 for the HTS bulk was obtained. The same non-destructive method was applied to estimate the n-index in a trapezoidal toroid-shaped SMB, which resulted in an n-index of 40 for the HTS assembly in this configuration. The results, however, appeared to be affected by temperature dependence of the PM magnetization and the semi-isothermal condition in bearings.

7.1.2 Application of FBG Sensors in SMBs

The temperature of the top surface of an HTS bulk in cryo-cooled SMBs may be different to the temperature of the cold head, due to thermal resistance and time constant between the HTS bulk and the cold head. Measuring the temperature of the HTS surface facing a rotating PM with conventional sensors is challenging due to limited mounting space, electromagnetic interference, and poor thermal insulation of electronic sensors. In this thesis, FBG sensors were implemented

in an actual SMB environment as a solution to overcome the issues imposed by electronic sensors for temperature and strain measurement. Levitation force decay measurements were performed on a dry cryo-cooled SMB, and the temperature of the top surface of the HTS bulk was successfully measured by an FBG sensor during the decay experiments. Furthermore, a flux-pinning-induced tensile stress was detected by FBG sensors during levitation force decay measurements. The results, however, appeared to be sensitive to the sensor bonding method.

These studies were conducted to address the first research goal:
Developing a non-destructive method based on levitation force relaxation mechanism to estimate HTS assembly parameters in SMBs.

7.1.3 AC loss

AC losses in SMBs are said to be generated by magnetic field inhomogeneity. Analytical models based on the Bean model show that the hysteresis loss in HTS bulks is proportional to the cube of magnetic field inhomogeneity. However, in these models, neither the frequency of magnetic field in one complete rotation nor the distribution of AC loss over the bearing surface is taken into account. Furthermore, the relationship between AC losses and magnetic field inhomogeneity in an actual SMB environment has not been explored experimentally. A new analytical model was proposed in this thesis which takes both magnetic field periodicity and AC loss distribution into account. Performing spin-down measurements with magnets of different levels of inhomogeneity tested the new analytical expressions. A relationship between magnetic field inhomogeneity and the dynamic behaviour of the superconducting bearing was also revealed in the spin-down measurements results. The resonance region widens and the resonance frequency of the bearing, and hence the bearing stiffness, decreases with inhomogeneity. This should be considered when designing SMBs for real applications. The experiments performed in chapter 5 were the most challenging in this thesis. This chapter was devoted to the second research goal:
Investigating the AC loss and its relation with magnetic field inhomogeneity in actual SMB conditions.

7.1.4 High-speed Application of SMBs

The principle of application of high-temperature SMBs for high-speed motors/generators was proved by designing, building, and testing a high-speed experimental rig. The frequency dependence of AC losses in SMBs was studied in a motor/generator

prototype. This prototype is believed to be the fastest superconducting bearing made in New Zealand. A rotational speed of 90000 rpm was maintained for a shaft of about 28 g mass with an input power of 3.24 W. Spin-down measurements showed that a frequency-dependent term appears in deceleration rate vs rotational frequency graphs. This means that at high rotational frequencies, an eddy-current-like mechanism exists as well as hysteresis loss. However, this eddy-current-like loss mechanism becomes dominant and it initially increases with rotational frequency, then decreases again, which can be explained by the nonlinear magnetic diffusion theory in high-temperature superconductors. The cryogenic performance of a flexible thermal link was also evaluated. It proved to be capable of removing excessive Joule heating created at kHz-rated operational frequencies.

The experimental rig built for these experiments was the most promising in this thesis since it demonstrates the engineering capabilities of *Paihau-Robinson Research Institute* for an ongoing technological project in New Zealand. Chapter 6 of this thesis was devoted to the third research goal:
Designing, building, and testing a high-speed motor/generator demonstration in order to prove the principle and to develop our capabilities of manufacturing SMBs that can meet our project requirements.

7.2 Future Work

The following paragraphs outline the questions that were raised during the course of this thesis, yet not studied due to the limited time. I hope these questions, as well as those covered in this thesis, inspire other researchers to follow the work done in this thesis and to investigate the unaddressed problems.

In chapter 4, the flux creep exponent (n-index) was estimated from levitation force relaxation in a high-temperature SMB. In this method, the classic Kim-Anderson model was used. Although being evaluated in many high-temperature relaxation experiments, including this thesis, the Kim-Anderson model was formulated for low-temperature superconductors. More detailed models have been formulated to describe relaxation in high-temperature superconductors. A potential future study can employ these models to study levitation force decay and to estimate decay parameters. All levitation decay experiments reported in this thesis were performed at a constant temperature of 77 K. The impact of temperature on the non-destructive method explained in chapter 4, can improve the applicability and the accuracy of this method.

The application of FBG sensors in SMBs for temperature and strain measurements was studied during levitation force decay experiments. Considering the main advantages of FBGs over conventional electronic sensors, FBGs can be employed in dynamic high-speed measurements, and can become a useful tool to monitor temperature and strain on HTS bulk surfaces in practical SMB applications. The flux-pinning-induced strain distribution was measured at a constant temperature and velocity. The impact of temperature and velocity on flux-pinning-induced strain can be studied in the future.

Chapter 5 covered the relationship between magnetic field inhomogeneity and AC losses as well as the impact of inhomogeneity on the stiffness of the SMB. The main challenge in performing spin-down measurements was to engineer the experimental rig. As it was discussed, the PM coupling imposed a speed limit and caused vibrations during the release process. More efficient coupling systems can be designed in future allowing the loss mechanism and dynamic behaviour to be studied more accurately and over a wider frequency range.

For practical SMB applications, where the rotor is an assembly of PMs, the assembly with the lowest contribution to AC losses should be selected. Furthermore, a figure of merit can be defined for the magnetic field trapped in the HTS assembly. The inhomogeneity of the magnetic field trapped in the HTS assembly also contributes to AC losses in a different way, which requires a different definition of figure of merit.

In chapter 6 the rotational frequency dependence of AC losses was studied over a wide rotational frequency range from a magnetic diffusion point of view. There are only a few studies which have performed such high-speed measurements due to the complexity of the design and operation at kHz-rated rotational frequencies. The impact of temperature and magnetic field inhomogeneity on the frequency at which the deceleration rate peaks appears to be of practical importance for high-speed projects.

References

[1] J.R. Hull and M. Murakami. "Applications of bulk high-temperature Superconductors". In: *Proceedings of the IEEE* 92.10 (Oct. 2004), pp. 1705–1718. DOI: 10.1109/jproc.2004.833796.

[2] Chan-Joong Kim. *Superconductor Levitation*. Springer Singapore, 2019. DOI: 10.1007/978-981-13-6768-7.

[3] Magsoar. Valdemoro, Spain. URL: http://www.magsoar.com/ (visited on 01/25/2019).

[4] John R Hull. "Superconducting bearings". In: *Superconductor Science and Technology* 13.2 (Jan. 2000), R1–R15. DOI: 10.1088/0953-2048/13/2/201.

[5] Alberto Tenconi, Silvio Vaschetto, and Alessandro Vigliani. "Electrical Machines for High-Speed Applications: Design Considerations and Tradeoffs". In: *IEEE Transactions on Industrial Electronics* 61.6 (June 2014), pp. 3022–3029. DOI: 10.1109/tie.2013.2276769.

[6] I. A. Zverev, I.-U. Eun, and C. M. Lee. "Simulation of Spindle Units Running on Rolling Bearings". In: *The International Journal of Advanced Manufacturing Technology* 21.10-11 (July 2003), pp. 889–895. DOI: 10.1007/s00170-002-1411-2.

[7] A. Borisavljevic, H. Polinder, and J.A. Ferreira. "On the Speed Limits of Permanent-Magnet Machines". In: *IEEE Transactions on Industrial Electronics* 57.1 (Jan. 2010), pp. 220–227. DOI: 10.1109/tie.2009.2030762.

[8] A M Forrest. "Meissner and Ochsenfeld revisited". In: *European Journal of Physics* 4.2 (Apr. 1983), pp. 117–120. DOI: 10.1088/0143-0807/4/2/011.

[9] Heike Kamerlingh Onnes. "Investigations into the properties of substances at low temperatures, which have led, amongst other things, to the preparation of liquid helium". In: *Nobel lecture* 4 (1913), pp. 306–336.

[10] "The electromagnetic equations of the supraconductor". In: *Proceedings of the Royal Society of London. Series A - Mathematical and Physical Sciences* 149.866 (Mar. 1935), pp. 71–88. DOI: 10.1098/rspa.1935.0048.

[11] J.M. Casimir-Jonker and W.J. De Haas. "Some experiments on a supraconductive alloy in a magnetic field". In: *Physica* 2.1-12 (Jan. 1935), pp. 935–942. DOI: 10.1016/s0031-8914(35)90179-3.

[12] A. A. Abrikosov. "Nobel Lecture: Type-II superconductors and the vortex lattice". In: *Reviews of Modern Physics* 76.3 (Dec. 2004), pp. 975–979. DOI: 10.1103/revmodphys.76.975.

[13] V. L. Ginzburg. "On the theory of superconductivity". In: *Il Nuovo Cimento* 2.6 (Dec. 1955), pp. 1234–1250. DOI: 10.1007/bf02731579.

[14] Robert Doll and M Näbauer. "Experimental proof of magnetic flux quantization in a superconducting ring". In: *Physical Review Letters* 7.2 (1961), p. 51. DOI: 10.1103/PhysRevLett.7.51.

[15] ZZ Hu, JX Jin, J Liu, HT Ren, LH Lei, and TF Xiang. "Development and applications of high T c superconducting bulk materials". In: *2009 International Conference on Applied Superconductivity and Electromagnetic Devices*. IEEE. 2009, pp. 42–47. DOI: 10.1109/asemd.2009.5306697.

[16] V. ARKADIEV. "A Floating Magnet". In: *Nature* 160.4062 (Sept. 1947), pp. 330–330. DOI: 10.1038/160330a0.

[17] I. Šimon. "Forces Acting on Superconductors in Magnetic Fields". In: *Journal of Applied Physics* 24.1 (Jan. 1953), pp. 19–24. DOI: 10.1063/1.1721125.

[18] K. F. Schoch and B. Darrel. "A Superconducting Gyroscope for Gimballed Platform Application". In: *Advances in Cryogenic Engineering*. Springer US, 1967, pp. 657–665. DOI: 10.1007/978-1-4757-0489-1_68.

[19] T.A Buchhold. "Three-phase motor with superconductive bearings". In: *Cryogenics* 5.4 (Aug. 1965), pp. 216–219. DOI: 10.1016/0011-2275(65)90061-5.

[20] J.R. Powell and G.T. Danby. "Magnetic suspension for levitated tracked vehicles". In: *Cryogenics* 11.3 (June 1971), pp. 192–204. DOI: 10.1016/0011-2275(71)90311-0.

[21] C. A. Guderjahn, S. L. Wipf, H. J. Fink, R. W. Boom, K. E. MacKenzie, D. Williams, and T. Downey. "Magnetic Suspension and Guidance for High Speed Rockets by Superconducting Magnets". In: *Journal of Applied Physics* 40.5 (Apr. 1969), pp. 2133–2140. DOI: 10.1063/1.1657938.

[22] M. K. Wu, J. R. Ashburn, C. J. Torng, P. H. Hor, R. L. Meng, L. Gao, Z. J. Huang, Y. Q. Wang, and C. W. Chu. "Superconductivity at 93 K in a new mixed-phase Y-Ba-Cu-O compound system at ambient pressure". In: *Physical Review Letters* 58.9 (Mar. 1987), pp. 908–910. DOI: 10.1103/physrevlett.58.908.

[23] C. W. Chu. "Superconductivity above 90 K". In: *Proceedings of the National Academy of Sciences* 84.14 (July 1987), pp. 4681–4682. DOI: 10.1073/pnas.84.14.4681.

[24] E. A. Early, C. L. Seaman, K. N. Yang, and M. B. Maple. "Demonstrating superconductivity at liquid nitrogen temperatures". In: *American Journal of Physics* 56 (7 1988), pp. 617–620. ISSN: 0002-9505. DOI: 10.1119/1.15524.

[25] E. H. Brandt. "Friction in levitated superconductors". In: *Applied Physics Letters* 53.16 (Oct. 1988), pp. 1554–1556. DOI: 10.1063/1.100435.

[26] E. H. Brandt. "Levitation in Physics". In: *Science* 243.4889 (Jan. 1989), pp. 349–355. DOI: 10.1126/science.243.4889.349.

[27] E. H. Brandt. "Rigid levitation and suspension of high-temperature superconductors by magnets". In: *American Journal of Physics* 58.1 (Jan. 1990), pp. 43–49. DOI: 10.1119/1.16317.

[28] Francis C. Moon. *Superconducting Levitation*. Wiley, Mar. 1995. DOI: 10.1002/9783527617524.

[29] Anjali Bhatnagar Riise. *Levitation force and magnetization in bulk and thin film high T c superconductors*. Tech. rep. Oslo Univ., 1998.

[30] Paul Seidel, ed. *Applied Superconductivity*. Wiley-VCH Verlag GmbH & Co. KGaA, Jan. 2015. DOI: 10.1002/9783527670635.

[31] Loïc Quéval, Kun Liu, Wenjiao Yang, Víctor MR Zermeño, and Guangtong Ma. "Superconducting magnetic bearings simulation using an H-formulation finite element model". In: *Superconductor Science and Technology* 31.8 (2018), p. 084001. DOI: 10.1088/1361-6668/aac55d.

[32] C. Navau, N. Del-Valle, and A. Sanchez. "Macroscopic Modeling of Magnetization and Levitation of Hard Type-II Superconductors: The Critical-State Model". In: *IEEE Transactions on Applied Superconductivity* 23.1 (Feb. 2013), pp. 8201023–8201023. DOI: 10.1109/tasc.2012.2232916.

[33] A. M. Campbell. "An Introduction to Numerical Methods in Superconductors". In: *Journal of Superconductivity and Novel Magnetism* 24.1-2 (Sept. 2010), pp. 27–33. DOI: 10.1007/s10948-010-0895-5.

[34] Charles P Bean. "Magnetization of high-field superconductors". In: *Reviews of modern physics* 36.1 (1964), p. 31. DOI: 10.1103/RevModPhys.36.31.

[35] Kévin Berger, Jean Lévêque, Denis Netter, Bruno Douine, and Abderrezak Rezzoug. "Influence of Temperature and/or Field Dependences of the *EJ* Power Law on Trapped Magnetic Field in Bulk YBaCuO". In: *IEEE transactions on applied superconductivity* 17.2 (2007), pp. 3028–3031. DOI: 10.1109/tasc.2007.902095.

[36] Boyang Shen, Francesco Grilli, and Tim Coombs. "Overview of H-formulation: A versatile tool for modeling electromagnetics in high-temperature superconductor applications". In: *IEEE access* 8 (2020), pp. 100403–100414. DOI: 10.1109/ACCESS.2020.2996177.

[37] DHN Dias, GG Sotelo, RB Kasal, R de Andrade Jr, and AC Ferreira. "The flux creep effect in superconducting magnetic bearings levitation force". In: *Journal of Physics: Conference Series*. Vol. 97. 1. IOP Publishing. 2008, p. 012216. DOI: 10.1088/1742-6596/97/1/012216.

[38] Guang-Tong Ma, Jia-Su Wang, and Su-Yu Wang. "Numerical Study of the Speed-Related Behavior of the Magnetic Force in the HTS Maglev System Based on a 3-D Model". In: *Journal of superconductivity and novel magnetism* 24.5 (2011), pp. 1593–1598. DOI: 10.1007/s10948-010-1062-8.

[39] D Ruiz-Alonso, T Coombs, and AM Campbell. "Computer modelling of high-temperature superconductors using an A–V formulation". In: *Superconductor Science and Technology* 17.5 (2004), S305. DOI: 10.1088/0953-2048/17/5/042.

[40] Philip W Anderson. "Theory of flux creep in hard superconductors". In: *Physical Review Letters* 9.7 (1962), p. 309. DOI: 10.1103/PhysRevLett.9.309.

[41] Philip W Anderson and YB Kim. "Hard superconductivity: theory of the motion of Abrikosov flux lines". In: *Reviews of modern physics* 36.1 (1964), p. 39. DOI: 10.1103/RevModPhys.36.39.

[42] Y. Yeshurun, A. P. Malozemoff, and A. Shaulov. "Magnetic relaxation in high-temperature superconductors". In: *Reviews of Modern Physics* 68.3 (July 1996), pp. 911–949. DOI: 10.1103/revmodphys.68.911.

[43] Zhiqiang Yu, Wenjie Feng, Zhifeng Gu, and Cheng Wen. "Dynamic Electromagnetic Behaviors of High-Temperature Superconductor Levitation System Based on YBCO Material from 3D Perspective". In: *Journal of Superconductivity and Novel Magnetism* (2019), pp. 1–16. DOI: 10.1007/s10948-019-05238-x.

[44] John Bardeen. "Theories of High T_c Superconductors". In: *MRS Proceedings* 99 (1987), p. 27. DOI: 10.1557/proc-99-27.

[45] Anup Patel, Simon Craig Hopkins, Algirdas Baskys, V Kalitka, A Molodyk, and Bartlomiej Andrzej Glowacki. "Magnetic levitation using high temperature superconducting pancake coils as composite bulk cylinders". In: *Superconductor Science and Technology* 28.11 (2015), p. 115007. DOI: 10.1088/0953-2048/28/11/115007.

[46] YS Tseng, CH Chiang, and WC Chan. "Levitation force relaxation in YBCO superconductors". In: *Physica C: Superconductivity* 411.1-2 (2004), pp. 32–34. DOI: 10.1016/j.physc.2004.06.001.

[47] You-He Zhou, Xing-Yi Zhang, and Jun Zhou. "Relaxation transition due to different cooling processes in a superconducting levitation system". In: *Journal of Applied Physics* 103.12 (June 2008), p. 123901. DOI: 10.1063/1.2938048.

[48] Lu Liu, Jiasu Wang, Zigang Deng, Jing Li, Jun Zheng, Guangtong Ma, and Suyu Wang. "Levitation Force Transition of High-Tc Superconducting Bulks in Varying External Magnetic Field". In: *IEEE Transactions on Applied Superconductivity* 20.3 (June 2010), pp. 920–923. DOI: 10.1109/tasc.2010.2041645.

[49] Jimin Xu, Fei Zhang, Tao Sun, Xiaoyang Yuan, and Cuiping Zhang. "Effect of reciprocating motions around working points on levitation force of superconductor-magnet system". In: *Cryogenics* 78 (Sept. 2016), pp. 96–102. DOI: 10.1016/j.cryogenics.2016.07.010.

[50] Yun-Jiang Rao. "In-fibre Bragg grating sensors". In: *Measurement Science and Technology* 8.4 (Apr. 1997), pp. 355–375. DOI: 10.1088/0957-0233/8/4/002.

[51] A. Chiuchiolo, M. Bajko, J. C. Perez, H. Bajas, M. Consales, M. Giordano, G. Breglio, and A. Cusano. "Fiber Bragg Grating Cryosensors for Superconducting Accelerator Magnets". In: *IEEE Photonics Journal* 6.6 (Dec. 2014), pp. 1–10. DOI: 10.1109/jphot.2014.2343994.

[52] R. Rajinikumar, K.G. Narayankhedkar, G. Krieg, M. Suber, A. Nyilas, and K.P. Weiss. "Fiber Bragg Gratings for Sensing Temperature and Stress in Superconducting Coils". In: *IEEE Transactions on Applied Superconductivity* 16.2 (June 2006), pp. 1737–1740. DOI: 10.1109/tasc.2005.864332.

[53] Hongjie Zhang, Fanping Deng, Qiuliang Wang, Luguang Yan, Yingming Dai, and Keeman Kim. "Development of Strain Measurement in Superconducting Magnet Through Fiber Bragg Grating". In: *IEEE Transactions on Applied Superconductivity* 18.2 (June 2008), pp. 1419–1422. DOI: 10.1109/tasc.2008.922242.

[54] Maximilian Fisser, Xiyong Huang, Dominic A Moseley, Chris Bumby, and Rodney A Badcock. "Evaluation of continuous fiber Bragg grating and signal processing method for hotspot detection at cryogenic temperatures". In: *Superconductor Science and Technology* 35.5 (2022), p. 054005. DOI: 10.1088/1361-6668/ac5d68.

[55] Zhen Zhang, Yingzhe Wang, Ze Feng, Jinrui Shi, Chengtao Wang, Daozheng Li, Huanli Yao, Chunyan Li, Rui Kang, Litong Li, and Qingjin Xu. "Preliminary Strain Measurement in High Field Superconducting Magnets With Fiber Bragg Grating". In: *IEEE Transactions on Applied Superconductivity* 32.6 (2022), pp. 1–5. DOI: 10.1109/tasc.2022.3158341.

[56] M Zeisberger, I Latka, W Ecke, T Habisreuther, D Litzkendorf, and W Gawalek. "Measurement of the thermal expansion of melt-textured YBCO using optical fibre grating sensors". In: *Superconductor Science and Technology* 18.2 (2005), S202–S205. DOI: 10.1088/0953-2048/18/2/041.

[57] Ines Latka, Tobias Habisreuther, and Matthias Zeisberger. "Fiber Bragg grating based spatially resolved characterization of flux-pinning-induced strain of disk-shaped bulk YBCO samples". In: *Cryogenics* 49.7 (July 2009), pp. 340–345. DOI: 10.1016/j.cryogenics.2009.03.004.

[58] John R Hull, Thomas M Mulcahp, Kenneth L Uherka, Robert A Erck, and Robert G Abboud. "Flywheel energy storage using superconducting magnetic bearings". In: *Applied superconductivity* 2.7-8 (1994), pp. 449–455. DOI: 10.1016/0964-1807(94)90035-3.

[59] John R Hull, Thomas M Mulcahy, and Joseph F Labataille. "Velocity dependence of rotational loss in Evershed-type superconducting bearings". In: *Applied physics letters* 70.5 (1997), pp. 655–657. DOI: 10.1063/1.118324.

[60] John R Hull, Joseph F Labataille, Thomas M Mulcahy, and J Anthony Lockwood. "Reduced hysteresis loss in superconducting bearings". In: *Applied superconductivity* 4.1-2 (1996), pp. 1–10. DOI: 10.1016/0964-1807(96)00011-7.

[61] YH Han, JR Hull, SC Han, NH Jeong, JM Oh, and Tae-Hyun Sung. "Losses of superconductor journal bearing". In: *AIP Conference Proceedings*. Vol. 710. 1. American Institute of Physics. 2004, pp. 1899–1905. DOI: 10.1063/1.1774893.

[62] John R Hull, TM Mulcahy, KL Uherka, and RG Abboud. "Low rotational drag in high-temperature superconducting bearings". In: *IEEE Transactions on Applied Superconductivity* 5.2 (1995), pp. 626–629. DOI: 10.1109/77.402628.

[63] Arthur C Day, John R Hull, Michael Strasik, Phil E Johnson, Kevin E McCrary, John Edwards, John A Mittleider, James R Schindler, Richard A Hawkins, and Michael L Yoder. "Temperature and frequency effects in a high-performance superconducting bearing". In: *IEEE transactions on applied superconductivity* 13.2 (2003), pp. 2179–2184. DOI: 10.1109/tasc.2003.813028.

[64] JR Hull, M Strasik, JA Mittleider, JF Gonder, PE Johnson, KE McCrary, and CR McIver. "High rotational-rate rotor with high-temperature superconducting bearings". In: *IEEE Transactions on applied superconductivity* 19.3 (2009), pp. 2078–2082. DOI: 10.1109/tasc.2009.2017864.

[65] Kazuyuki Demachi, Ryusuke Numata, Ryota Shimizu, Kenzo Miya, and Hiromasa Higasa. "AC loss of HTSC bulks for magnetic levitation". In: *Journal of Materials Processing Technology* 108.2 (2001), pp. 141–144. DOI: 10.1016/s0924-0136(00)00742-1.

[66] N Koshizuka. "R&D of superconducting bearing technologies for flywheel energy storage systems". In: *Physica C: Superconductivity and its applications* 445 (2006), pp. 1103–1108. DOI: 10.1016/j.physc.2006.05.045.

[67] AN Terentiev and AA Kuznetsov. "Drift of levitated YBCO superconductor induced by both a variable magnetic field and a vibration". In: *Physica C: Superconductivity* 195.1-2 (1992), pp. 41–46. DOI: 10.1016/0921-4534(92)90071-j.

[68] M Strasik, JR Hull, JA Mittleider, JF Gonder, PE Johnson, KE McCrary, and CR McIver. "An overview of Boeing flywheel energy storage systems with high-temperature superconducting bearings". In: *Superconductor science and technology* 23.3 (2010), p. 034021. DOI: 10.1088/0953-2048/23/3/034021.

[69] Ke-xi Xu, Dong-jie Wu, YL Jiao, and MH Zheng. "A fully superconducting bearing system for flywheel applications". In: *Superconductor Science and Technology* 29.6 (2016), p. 064001. DOI: 10.1088/0953-2048/29/6/064001.

[70] AN Terentiev, HJ Lee, C-J Kim, and GW Hong. "Identification of magnet and superconductor contributions to the ac loss in a magnet-superconductor levitation system". In: *Physica C: Superconductivity* 290.3-4 (1997), pp. 291–296. DOI: 10.1016/s0921-4534(97)01675-4.

[71] A Stenvall and T Tarhasaari. "An eddy current vector potential formulation for estimating hysteresis losses of superconductors with FEM". In: *Superconductor Science and Technology* 23.12 (2010), p. 125013. DOI: 10.1088/0953-2048/23/12/125013.

[72] MN Wilson. *Superconducting Magnets*. Clarendon Press, 1983. ISBN: 0 19 854805 2.

[73] H Hashizume, Toshihiko Sugiura, K Miya, Y Ando, S Akita, S Torii, Y Kubota, and T Ogasawara. "Numerical analysis of ac losses in superconductors". In: *Cryogenics* 31.7 (1991), pp. 601–606. DOI: 10.1016/0011-2275(91)90057-4.

[74] V Lahtinen, M Lyly, A Stenvall, and T Tarhasaari. "Comparison of three eddy current formulations for superconductor hysteresis loss modelling". In: *Superconductor Science and Technology* 25.11 (2012), p. 115001. DOI: 10.1088/0953-2048/25/11/115001.

[75] BR Weinberger, L Lynds, JR Hull, and U Balachandran. "Low friction in high temperature superconductor bearings". In: *Applied physics letters* 59.9 (1991), pp. 1132–1134. DOI: 10.1063/1.106367.

[76] M Ye, Wenjiang Yang, Yu Liu, Yang Li, and L Yu. "A Design Method of HTS Bulks Array for Decreasing Rotation Loss in a Superconducting Maglev Microthrust Stand". In: *IEEE Transactions on Applied Superconductivity* 28.4 (2018), pp. 1–5. DOI: 10.1109/tasc.2018.2816106.

[77] Jeong-Phil Lee, Sang-Chul Han, and Byeong-Choel Park. "Experimental estimation on magnetic friction of superconductor flywheel energy storage system". In: *Journal of Magnetics* 16.2 (2011), pp. 124–128. DOI: 10.4283/jmag.2011.16.2.124.

[78] A Cansiz, AM Campbell, and TA Coombs. "An Evershed type superconducting flywheel bearing". In: *Physica C: Superconductivity* 390.4 (2003), pp. 305–310. DOI: 10.1016/s0921-4534(03)00725-1.

[79] Ahmet Cansiz and John R Hull. "Stable load-carrying and rotational loss characteristics of diamagnetic bearings". In: *IEEE transactions on magnetics* 40.3 (2004), pp. 1636–1641. DOI: 10.1109/tmag.2004.827181.

[80] Shang Jin, Zou Yincai, Bian Xing, Guan Xiang, Wu Jihao, and Li Qing. "Simulation and calculation on rotation loss of high temperature superconducting bearings". In: *Physica C: Superconductivity and its Applications* 568 (2020), p. 1353565. DOI: 10.1016/j.physc.2019.1353565.

[81] Takashi Hikihara, Hitoshi Adachi, Francis C Moon, and Yoshisuke Ueda. "Dynamical behavior of flywheel rotor suspended by hysteretic force of HTSC magnetic bearing". In: *Journal of Sound and Vibration* 228.4 (1999), pp. 871–887. DOI: 10.1006/jsvi.1999.2452.

[82] F.N. Werfel, U. Flögel-Delor, R. Rothfeld, D. Wippich, and T. Riedel. "Centrifuge advances using HTS magnetic bearings". In: *Physica C: Superconductivity* 354.1-4 (2001), pp. 13–17. DOI: 10.1016/s0921-4534(01)00015-6.

[83] F. C. Moon and P.-Z. Chang. "High-speed rotation of magnets on highTcsuperconducting bearings". In: *Applied Physics Letters* 56.4 (Jan. 1990), pp. 397–399. DOI: 10.1063/1.102795.

[84] M Strasik, JR Hull, PE Johnson, J Mittleider, KE McCrary, CR McIver, and AC Day. "Performance of a conduction-cooled high-temperature superconducting bearing". In: *Materials Science and Engineering: B* 151.3 (2008), pp. 195–198. DOI: 10.1016/j.mseb.2008.03.019.

[85] Yunus Kaya, Ahmet Cansiz, and Irfan Yildizer. "Driving Mechanism of a Superconducting Magnetic Bearing System". In: *Journal of Superconductivity and Novel Magnetism* 26.4 (2012), pp. 1233–1239. DOI: 10.1007/s10948-012-1842-4.

[86] A. Cansiz, I. Yildizer, E. A. Oral, and Y. Kaya. "An Effective Noncontact Torque Mechanism and Design Considerations for an Evershed-Type Superconducting Magnetic Bearing System". In: *IEEE Transactions on Applied Superconductivity* 24.1 (2014), pp. 22–29. DOI: 10.1109/tasc.2013.2280033.

[87] T. Matsumura, S. Hanany, J.R. Hull, B. Johnson, and T. Jones. "Magnetic Field Inhomogeneity and Torque in High Temperature Superconducting Magnetic Bearings". In: *IEEE Transactions on Appiled Superconductivity* 15.2 (2005), pp. 2316–2319. DOI: 10.1109/tasc.2005.849641.

[88] T. Matsumura, Y. Sakurai, H. Kataza, S. Utsunomiya, and R. Yamamoto. "Magnetically coupled gear based drive mechanism for contactless continuous rotation using superconducting magnetic bearing below 10 K". In: *Physica C: Superconductivity and its Applications* 530 (2016), pp. 138–141. DOI: 10.1016/j.physc.2016.07.003.

[89] Z.J. Yang and J.R. Hull. "Energy loss in superconducting bearing systems". In: *IEEE Transactions on Appiled Superconductivity* 7.2 (1997), pp. 318–321. DOI: 10.1109/77.614494.

[90] AA Kordyuk, G Krabbes, VV Nemoshkalenko, and RV Viznichenko. "Surface influence on flux penetration into HTS bulks". In: *Physica B: Condensed Matter* 284 (2000), pp. 903–904. DOI: 10.1016/s0921-4526(99)02219-x.

[91] Alexander A Kordyuk, Vladimir V Nemoshkalenko, Roman V Viznichenko, and Wolfgang Gawalek. "The investigation of magnetic flux dynamics in the bulk HTS with the levitation techniques". In: *Materials Science and Engineering: B* 53.1-2 (1998), pp. 174–176. DOI: 10.1016/s0921-5107(97)00322-x.

[92] Kazuyuki Demachi, Akira Miura, Tetsuya Uchimoto, Kenzo Miya, Hiromasa Higasa, Ryoichi Takahata, and Hiroo Kameno. "Experimental and numerical evaluation of rotation speed degradation of radial type superconducting magnetic bearing". In: *Physica C: Superconductivity* 357 (2001), pp. 882–885. DOI: 10.1016/s0921-4534(01)00438-5.

[93] M Kita, T Ichihara, I Masaie, K Demachi, Naomichi Sakai, and I Hirabayashi. "Rotation loss reduction of superconducting magnetic bearings by stacking and rearranging the shape of the bulks". In: *Physica C: Superconductivity* 426 (2005), pp. 821–825. DOI: 10.1016/j.physc.2005.01.053.

[94] Kazuyuki Demachi, Issei Masaie, Takumi Ichihara, and Makoto Kita. "Rotation speed degradation of superconducting magnetic bearing made of unsymmetrical shaped YBCO bulks". In: *Physica C: Superconductivity* 426 (2005), pp. 826–833. DOI: 10.1016/j.physc.2005.03.081.

[95] Issei Masaie, Kazuyuki Demachi, Takumi Ichihara, and Mitsuru Uesaka. "Numerical evaluation of rotational speed degradation in the superconducting magnetic bearing for various superconducting bulk shapes". In: *IEEE transactions on applied superconductivity* 15.2 (2005), pp. 2257–2260. DOI: 10.1109/tasc.2005.849625.

[96] C. E. Rossman, J. I. Budnick, and B. R. Weinberger. "Correlation of frictional losses of spinning levitated magnets with ac susceptibility in high-temperature superconductors". In: *Applied Physics Letters* 70.2 (1997), pp. 255–257. DOI: 10.1063/1.118383.

[97] Comsol Multiphysics. MA, USA. URL: https://www.comsol.com/ (visited on 10/10/2019).

[98] F Sass, G G Sotelo, R de Andrade Junior, and Frédéric Sirois. "H-formulation for simulating levitation forces acting on HTS bulks and stacks of 2G coated conductors". In: *Superconductor Science and Technology* 28.12 (Nov. 2015), p. 125012. DOI: 10.1088/0953-2048/28/12/125012.

[99] Loïc Quéval, Kun Liu, Wenjiao Yang, Víctor M R Zermeño, and Guangtong Ma. "Superconducting magnetic bearings simulation using an H-formulation finite element model". In: *Superconductor Science and Technology* 31.8 (June 2018), p. 084001. DOI: 10.1088/1361-6668/aac55d.

[100] James G. Storey, Mathieu Szmigiel, Fergus Robinson, Stuart C. Wimbush, and Rodney A. Badcock. "Stiffness Enhancement of a Superconducting Magnetic Bearing Using Shaped YBCO Bulks". In: *IEEE Transactions on Applied Superconductivity* 30.4 (June 2020), pp. 1–6. DOI: 10.1109/tasc.2020.2982884.

[101] Advanced Hall Sensors Ltd. Manchester, UK. URL: https://www.ahsltd.com/p15a-hall-sensor (visited on 10/01/2020).

[102] Tektronix. OR, USA. URL: https://www.tek.com/en/products/keithley/source-measure-units/2400-standard-series-sourcemeter (visited on 10/01/2020).

[103] National Instruments. TX, USA. URL: https://www.ni.com/docs/en-US/bundle/usb-6008-6009-getting-started/resource/375553a.pdf (visited on 02/10/2020).

[104] Trio Motion Technology. Gloucestershire, UK. URL: https://triomotion.com/public/products/p826-p827.php (visited on 03/01/2021).

[105] CAN Superconductors. Kamenice, Czech Republic. URL: https://shop.can-superconductors.com/index.php?id_product=14&controller=product&id_lang=1 (visited on 10/01/2029).

[106] Tinius Olsen. PA, USA. URL: https://www.tiniusolsen.com/ (visited on 04/10/2020).

[107] National Instrument. TX, USA. URL: https://www.ni.com/en-nz/shop/labview.html (visited on 11/10/2019).

[108] Selleys. VIC, Australia. URL: https://www.selleys.co.nz/products/adhesives/heavy-duty-repairs/selleys-araldite-5-minute/ (visited on 04/01/2020).

[109] Antonio Morandi, Massimo Fabbri, Pier Luigi Ribani, Anthony Dennis, John Durrell, Yunhua Shi, and David Cardwell. "The Measurement and Modeling of the Levitation Force Between Single-Grain YBCO Bulk Superconductors and Permanent Magnets". In: *IEEE Transactions on Applied Superconductivity* 28.5 (Aug. 2018), pp. 1–10. DOI: 10.1109/tasc.2018.2822721.

[110] B.M Smolyak, G.N Perelshtein, and G.V Ermakov. "Effects of relaxation in levitating superconductors". In: *Cryogenics* 42.10 (Oct. 2002), pp. 635–644. DOI: 10.1016/s0011-2275(02)00081-4.

[111] James Storey, Mathieu Szmigiel, Fergus Robinson, Stuart C. Wimbush, and Rod Badcock. "Stiffness Enhancement of a Superconducting Magnetic Bearing Using Shaped YBCO Bulks". In: (Dec. 2019). DOI: 10.36227/techrxiv.11344931.v1.

[112] SuperMagnetMan. AL, USA. URL: https://supermagnetman.com/collections/neo-cones/products/cone0150n (visited on 12/01/2019).

[113] CAN Superconductors. Kamenice, Czech Republic. URL: https://www.can-superconductors.com/hts-bulks-and-materials/custom-hts/ (visited on 10/01/2029).

[114] Galoce. Shaanxi, China. URL: https://www.galoce.com/ (visited on 10/01/2019).

[115] TE Connectivity. USA. URL: https://www.te.com/usa-en/product-02560984-000.html (visited on 11/01/2019).

[116] Cryogenic Control Systems. CA, USA. URL: https://www.cryocon.com/CryoSensors.php#PTRTD (visited on 11/01/2019).

[117] Cryogenic Control Systems. CA, USA. URL: https://www.cryocon.com/S900ProdFolder.php (visited on 11/01/2019).

[118] Cryogenic Control Systems. CA, USA. URL: https://www.cryocon.com/M26CProdFolder.php (visited on 11/01/2019).

[119] FBGS. Germany / Belgium. URL: https://fbgs.com/components/draw-tower-gratings-dtgs/ (visited on 02/01/2021).

[120] FBGS. Germany / Belgium. URL: https://fbgs.com/technology/ormocer-coating/ (visited on 02/01/2021).

[121] W. Schnelle, J. Engelhardt, and E. Gmelin. "Specific heat capacity of Apiezon N high vacuum grease and of Duran borosilicate glass". In: *Cryogenics* 39.3 (Mar. 1999), pp. 271–275. DOI: 10.1016/s0011-2275(99)00035-1.

[122] M&I Materials Limited. In: (). Manchester, UK.

[123] Magnets New Zealand. Auckland, New Zealand. URL: https://www.magnets.co.nz/shop/neodymium/discs-and-cylinders-neodymium/17mm-x-10mm-neodymium-disc/ (visited on 02/15/2020).

[124] Maxon Group. Switzerland. URL: https://www.maxongroup.com/maxon/view/category/motor?etcc_cu=onsite&etcc_med_onsite=Product&etcc_cmp_onsite=ECX+SPEED+program&etcc_plc=Overview-Page-Brushless-DC-Motors&etcc_var=\%5bcom\%5d\%23en\%23_d_&target=filter&filterCategory=ECX (visited on 10/10/2019).

[125] Edwards Vacuum. Atlas Copco Group, Sweden. URL: https://www.edwardsvacuum.com/en/our-products/turbomolecular-pumping-stations/T-station-85 (visited on 03/10/2020).

[126] Oxford Cryosystems. Oxford, UK. URL: https://www.oxcryo.com/mechanical-coolers/gm-cryocoolers/single-stage-coldheads (visited on 04/01/2020).

[127] Keyence. Illinois, USA. URL: https://www.keyence.com/download/download/confirmation/?dlAssetId=AS_6000&dlSeriesId=&dlModelId=&dlLangId=&dlLangType=en-US (visited on 03/01/2020).

[128] Monarch Instrument. Amherst, USA. URL: https://monarchinstrument.com/products/remote-optical-led-sensor-with-8-ft-cable-and-mounting (visited on 04/01/2020).

[129] kilwell FIBRELAB. Rotorua,New Zealand. URL: https://www.kilwellfibretube.co.nz/ (visited on 03/01/2020).

[130] SuperMagnetMan. AL, USA. URL: https://supermagnetman.com/collections/neo-cylinders/cyl-dia-6-36mm-10-9mm (visited on 07/01/2020).

[131] SuperVolt. China. URL: https://www.aliexpress.com/item/32899626673.html?spm=a2g0o.productlist.0.0.4ba36795Dzp6Yf&algo_pvid=e7cfbcbc-c0a9-40c3-a3a5-fa4d9d6eb053&algo_expid=e7cfbcbc-c0a9-40c3-a3a5-fa4d9d6eb053-26&btsid=0be3764515844005769027763eea44&ws_ab_test=searchweb0_0,searchweb201602_,searchweb201603_ (visited on 04/01/2022).

[132] Edwards Vacuum. Atlas Copco Group, Sweden. URL: https://www.edwardsvacuum.com/en/our-products/small-dry-pumps/dry-scroll-pumps (visited on 03/10/2020).

[133] I. Masaie, K. Demachi, T. Ichihara, and M. Uesaka. "Numerical Evaluation of Rotational Speed Degradation in the Superconducting Magnetic Bearing for Various Superconducting Bulk Shapes". In: *IEEE Transactions on Appiled Superconductivity* 15.2 (June 2005), pp. 2257–2260. DOI: 10.1109/tasc.2005.849625.

[134] I. Masaie, K. Demachi, T. Ichihara, and M. Uesaka. "Rotational Loss Modeling in Superconducting Magnetic Bearing". In: *IEEE Transactions on Applied Superconductivity* 16.2 (June 2006), pp. 1807–1810. DOI: 10.1109/tasc.2005.864309.

[135] Francesco Grilli, Antonio Morandi, Federica De Silvestri, and Roberto Brambilla. "Dynamic modeling of levitation of a superconducting bulk by coupled H-magnetic field and arbitrary Lagrangian–Eulerian formulations". In: *Superconductor Science and Technology* 31.12 (Oct. 2018), p. 125003. DOI: 10.1088/1361-6668/aae426.

[136] J. Z. Sun, C. B. Eom, B. Lairson, J. C. Bravman, and T. H. Geballe. "Magnetic relaxation, current-voltage characteristics, and possible dissipation mechanisms for high-Tcsuperconducting thin films of Y-Ba-Cu-O". In: *Physical Review B* 43.4 (Feb. 1991), pp. 3002–3008. DOI: 10.1103/physrevb.43.3002.

[137] Bruno Douine, Kevin Berger, Charles-Henri Bonnard, Frederic Sirois, Abelin Kameni, and Jean Leveque. "Improved Method for Determining the n-Value of HTS Bulks". In: *IEEE Transactions on Applied Superconductivity* 26.3 (Apr. 2016), pp. 1–4. DOI: 10.1109/tasc.2016.2533603.

[138] J. P. Rush, C. J. May-Miller, K. G. B. Palmer, N. A. Rutter, A. R. Dennis, Y.-H. Shi, D. A. Cardwell, and J. H. Durrell. "Transport in Bulk Superconductors: A Practical Approach?" In: *IEEE Transactions on Applied Superconductivity* 26.3 (Apr. 2016), pp. 1–4. DOI: 10.1109/tasc.2016.2537647.

[139] Mohammad Siamaki, James G. Storey, and Rodney A. Badcock. "Towards a Non-Destructive Method of Mapping the iE-J/i Relation Using Force Decay Measurements on Superconducting Bulks". In: *IEEE Transactions on Applied Superconductivity* 31.5 (Aug. 2021), pp. 1–5. DOI: 10.1109/tasc.2021.3068980.

[140] G Ries, H W Neumuller, and W Schmidt. "Voltage-current characteristic in Bi2Sr2CaCu2O8from transport and magnetization measurements". In: *Superconductor Science and Technology* 5.1S (Jan. 1992), S81–S84. DOI: 10.1088/0953-2048/5/1s/013.

[141] E. Sandvold and C. Rossel. "Evidence for collective flux pinning from magnetic relaxation combined with I–V characteristics in YBCO thin films". In: *Physica C: Superconductivity* 190.3 (Jan. 1992), pp. 309–315. DOI: 10.1016/0921-4534(92)90612-g.

[142] M.P. Philippe, J.-F. Fagnard, S. Kirsch, Z. Xu, A.R. Dennis, Y.-H. Shi, D.A. Cardwell, B. Vanderheyden, and P. Vanderbemden. "Magnetic characterisation of large grain, bulk Y–Ba–Cu–O superconductor–soft ferromagnetic alloy hybrid structures". In: *Physica C: Superconductivity* 502 (July 2014), pp. 20–30. DOI: 10.1016/j.physc.2014.04.025.

[143] J. Friedel, P. G. De Gennes, and J. Matricon. "Nature of the driving force in flux creep phenomena". In: *Applied Physics Letters* 2.6 (Mar. 1963), pp. 119–121. DOI: 10.1063/1.1753804.

[144] M. V. Feigel'man, V. B. Geshkenbein, A. I. Larkin, and V. M. Vinokur. "Theory of collective flux creep". In: *Physical Review Letters* 63.20 (Nov. 1989), pp. 2303–2306. DOI: 10.1103/physrevlett.63.2303.

[145] Xiyong Huang, Mike Davies, Dominic A. Moseley, Jofferson T. Gonzales, Hubertus W. Weijers, and Rodney A. Badcock. "Sensitive Fiber Optic Sensor for Rapid Hot-Spot Detection at Cryogenic Temperatures". In: *IEEE Sensors Journal* 22.12 (June 2022), pp. 11775–11782. DOI: 10.1109/jsen.2022.3174894.

[146] OriginLab. Ma, USA. URL: https://www.originlab.com/ (visited on 01/25/2020).

[147] E. Diez-Jimenez, J.L. Perez-Diaz, C. Ferdeghini, F. Canepa, C. Bernini, C. Cristache, J. Sanchez-Garcia-Casarrubios, I. Valiente-Blanco, E.M. Ruiz-Navas, and J.A. Martínez-Rojas. "Magnetic and morphological characterization of Nd2Fe14B magnets with different quality grades at low temperature 5–300K". In: *Journal of Magnetism and Magnetic Materials* 451 (Apr. 2018), pp. 549–553. DOI: 10.1016/j.jmmm.2017.11.109.

[148] M D Ainslie and H Fujishiro. "Modelling of bulk superconductor magnetization". In: *Superconductor Science and Technology* 28.5 (Mar. 2015), p. 053002. DOI: 10.1088/0953-2048/28/5/053002.

[149] High temperature superconducting wire critical current database. Paihau-Robinson research Institute, Victoria University of Wellington. URL: http://htsdb.wimbush.eu/dataset/1165595 (visited on 12/01/2020).

[150] Z. L. Feng, W. M. Yang, J. W. Li, M. Wang, Y. X. Yang, Z. B. Gao, and X. N. Huang. "A Practical Processing Method for the Fabrication of NdBCO Seed Crystals and High-Performance Single-Domain GdBCO Bulk Superconductors". In: *Journal of Superconductivity and Novel Magnetism* 33.6 (Feb. 2020), pp. 1559–1568. DOI: 10.1007/s10948-020-05424-2.

[151] Yunhua Shi, Michael Gough, Anthony R Dennis, John H Durrell, and David A Cardwell. "Distribution of the superconducting critical current density within a Gd–Ba–Cu–O single grain". In: *Superconductor Science and Technology* 33.4 (Feb. 2020), p. 044009. DOI: 10.1088/1361-6668/ab6dc2.

[152] G. Fuchs, P. Schätzle, G. Krabbes, S. Gruß, P. Verges, K.-H. Müller, J. Fink, and L. Schultz. "Trapped magnetic fields larger than 14 T in bulk YBa2Cu3O7-x". In: *Applied Physics Letters* 76.15 (Apr. 2000), pp. 2107–2109. DOI: 10.1063/1.126278.

[153] P Diko, V Antal, K Zmorayová, M Šefčiková, X Chaud, J Kováč, X Yao, I Chen, M Eisterer, and H W Weber. "The influence of post-growth thermal treatments on the critical current density of TSMG YBCO bulk superconductors". In: *Superconductor Science and Technology* 23.12 (Nov. 2010), p. 124002. DOI: 10.1088/0953-2048/23/12/124002.

[154] Tom H Johansen. "Flux-pinning-induced stress and magnetostriction in bulk superconductors". In: *Superconductor Science and Technology* 13.10 (Sept. 2000), R121–R137. DOI: 10.1088/0953-2048/13/10/201.

[155] Chen Guang Huang, Hua Dong Yong, and You He Zhou. "Magnetostrictive behaviors of type-II superconducting cylinders and rings with finite thickness". In: *Superconductor Science and Technology* 26.10 (2013), p. 105007. DOI: https://doi.org/10.1088/0953-2048/26/10/105007.

[156] S Kalsi, R A Badcock, K Hamilton, and J G Storey. "Homopolar superconducting AC machines, with HTS dynamo driven field coils, for aerospace applications". In: *IOP Conference Series: Materials Science and Engineering* 756.1 (Mar. 2020), p. 012028. DOI: 10.1088/1757-899x/756/1/012028.

[157] Mohammad Siamaki, James G. Storey, Lars Wiesehoefer, and Rodney A. Badcock. "Design, Build, and Evaluation of an AC Loss Measurement Rig for High-Speed Superconducting Bearings". In: *Energies* 15.4 (Feb. 2022), p. 1427. DOI: 10.3390/en15041427.

[158] Mohammad Siamaki, James G. Storey, Lars Wiesehoefer, and Rodney A. Badcock. "The impact of magnetic field periodicity on the hysteresis loss in superconducting magnetic bearings". In: *Superconductivity* 5 (Mar. 2023), p. 100040. DOI: 10.1016/j.supcon.2023.100040.

[159] Ahmet Cansiz. *Force, stiffness and hysteresis losses in high temperature superconducting bearings*. Illinois Institute of Technology, ProQuest Dissertations Publishing, 1999.

[160] T. Sugiura and H. Fujimori. "Mechanical resonance characteristics of a high-T/sub c/ superconducting levitation system". In: *IEEE Transactions on Magnetics* 32.3 (May 1996), pp. 1066–1069. DOI: 10.1109/20.497425.

[161] S. A. Basinger, J. R. Hull, and T. M. Mulcahy. "Amplitude dependence of magnetic stiffness in bulk high-temperature superconductors". In: *Applied Physics Letters* 57.27 (1990), pp. 2942–2944. DOI: 10.1063/1.104205.

[162] F. C. Moon, K-C. Weng, and P-Z. Chang. "Dynamic magnetic forces in superconducting ceramics". In: *Journal of Applied Physics* 66.11 (1989), pp. 5643–5645. DOI: 10.1063/1.343677.

[163] Wang Liqiu, Zhou Xuesheng, and Wei Xiaohao. *Heat conduction. Mathematical models and analytical solutions*. Springer Berlin, Heidelberg, 2008. DOI: 10.1007/978-3-540-74303-3.

[164] Y.S. Cha. "Magnetic diffusion and dissipation in high-Tc superconductors subjected to sinusoidal applied fields". In: *Physica C: Superconductivity* 361.1 (Aug. 2001), pp. 1–12. DOI: 10.1016/s0921-4534(01)00287-8.

[165] Y.S Cha. "Magnetic diffusion in high-Tc superconductors". In: *Physica C: Superconductivity* 330.1-2 (Mar. 2000), pp. 1–8. DOI: 10.1016/s0921-4534(99)00584-5.

[166] T.R. Askew, J.G. Nestell, R.B. Flippen, D.M. Groski, and N.McN. Alford. "Dynamic measurement of flux flow resistivity in YBa/sub 2/Cu/sub 3/O/sub 7/ wires". In: *IEEE Transactions on Applied Superconductivity* 3.1 (Mar. 1993), pp. 1398–1401. DOI: 10.1109/77.233637.

[167] T.R. Askew, J.C. O'Daniel, J.M. Weber, and Y.S. Cha. "Nonlinear Magnetic Diffusion in Single-Domain YBCO Cylinders Under Pulsed Field Conditions". In: *IEEE Transactions on Appiled Superconductivity* 15.2 (June 2005), pp. 3758–3761. DOI: 10.1109/tasc.2005.849424.

Appendices

A

Magnetic Field and Discrete Fourier Analysis of Permanent Magnets

The following graphs are the magnetic fields of the PMs used in section 5.4 and their associated discrete Fourier transform.

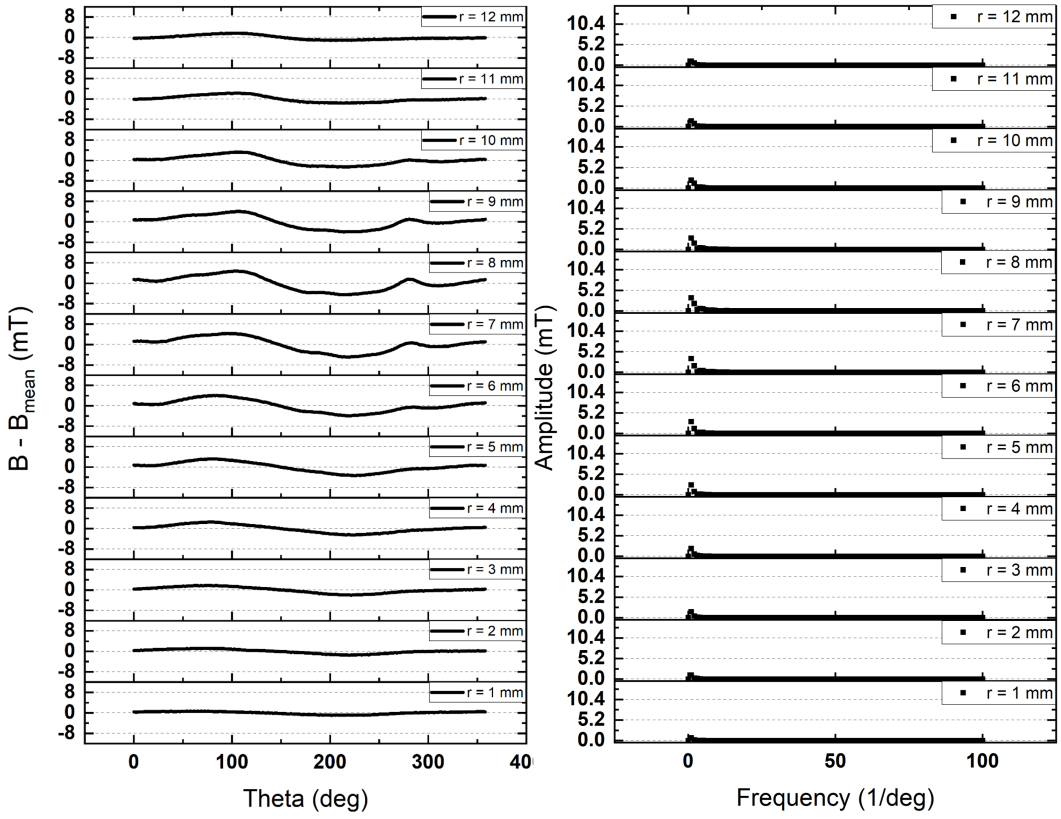

Figure A.1: Left: magnetic field of PM1 measured azimuthaly over its surface with r= 1 mm being the innermost radius. The radius of the magnet is 8.5 mm. The distance between the Hall sensor and the magnet surface is 2.7 mm. Right: the discrete Fourier transform of $B - B_{mean}$.

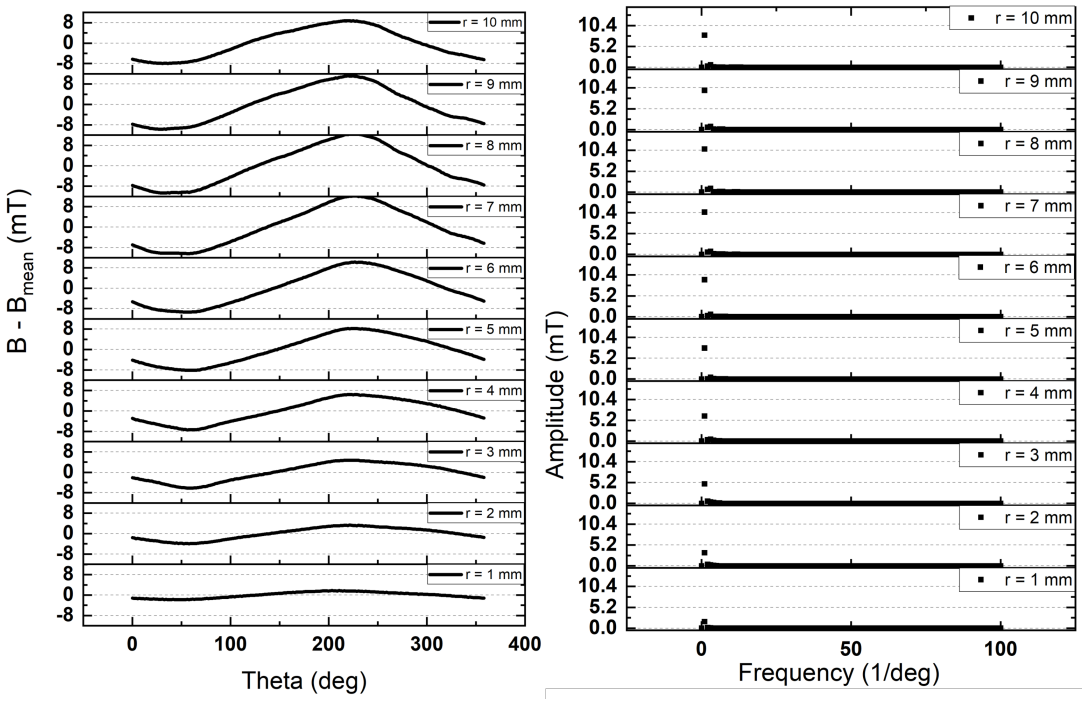

Figure A.2: Left: magnetic field of PM2 measured azimuthaly over its surface with r= 1 mm being the innermost radius. The radius of the magnet is 8.5 mm. The distance between the Hall sensor and the magnet surface is 2.7 mm. Right: the discrete Fourier transform of $B - B_{mean}$.

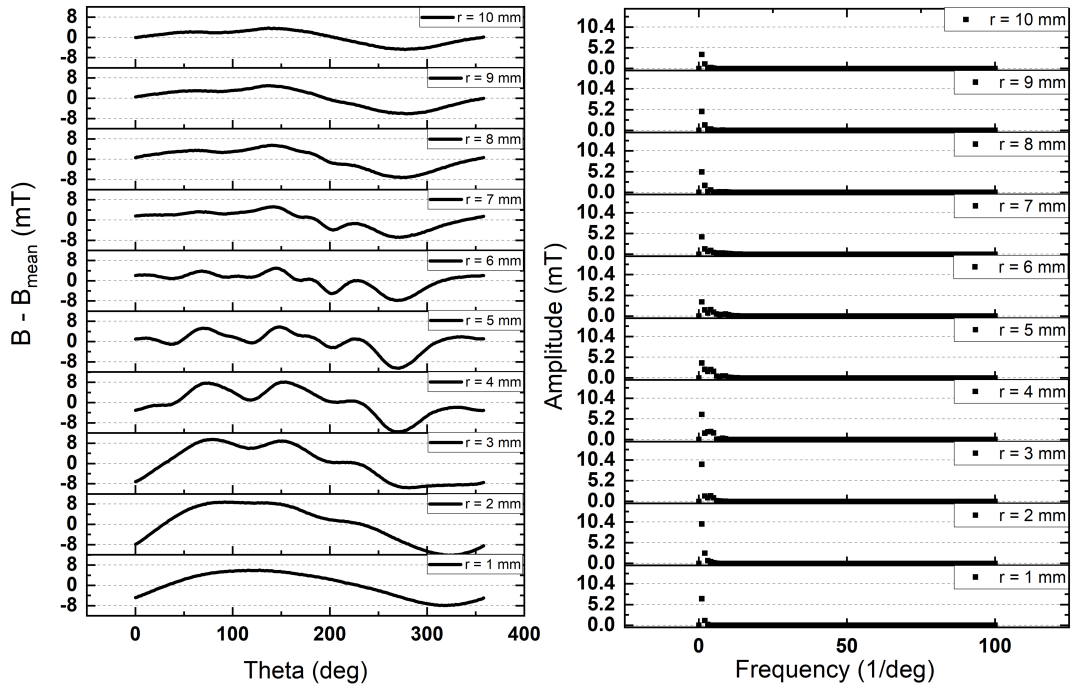

Figure A.3: Left: magnetic field of PM3 measured azimuthaly over its surface with r= 1 mm being the innermost radius. The radius of the magnet is 8.5 mm. The distance between the Hall sensor and the magnet surface is 2.7 mm. Right: the discrete Fourier transform of $B - B_{mean}$.

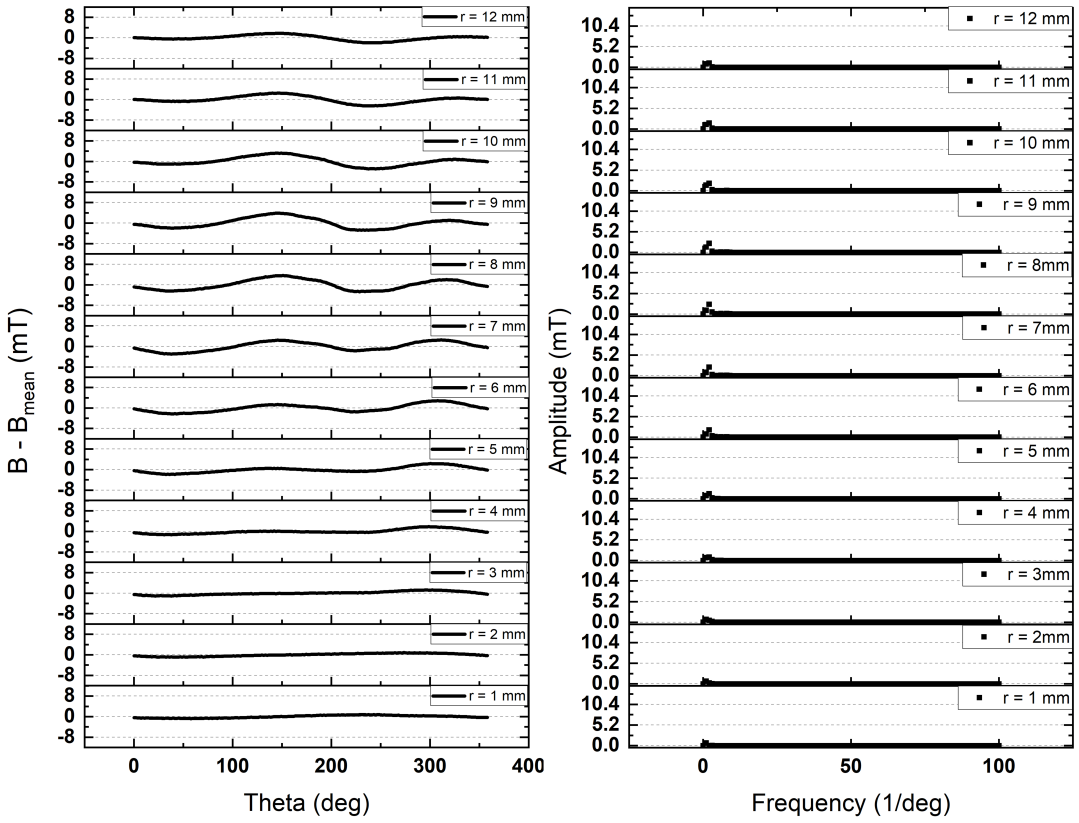

Figure A.4: Left: magnetic field of PM4 measured azimuthaly over its surface with r= 1 mm being the innermost radius. The radius of the magnet is 8.5 mm. The distance between the Hall sensor and the magnet surface is 2.7 mm. Right: the discrete Fourier transform of $B - B_{mean}$.

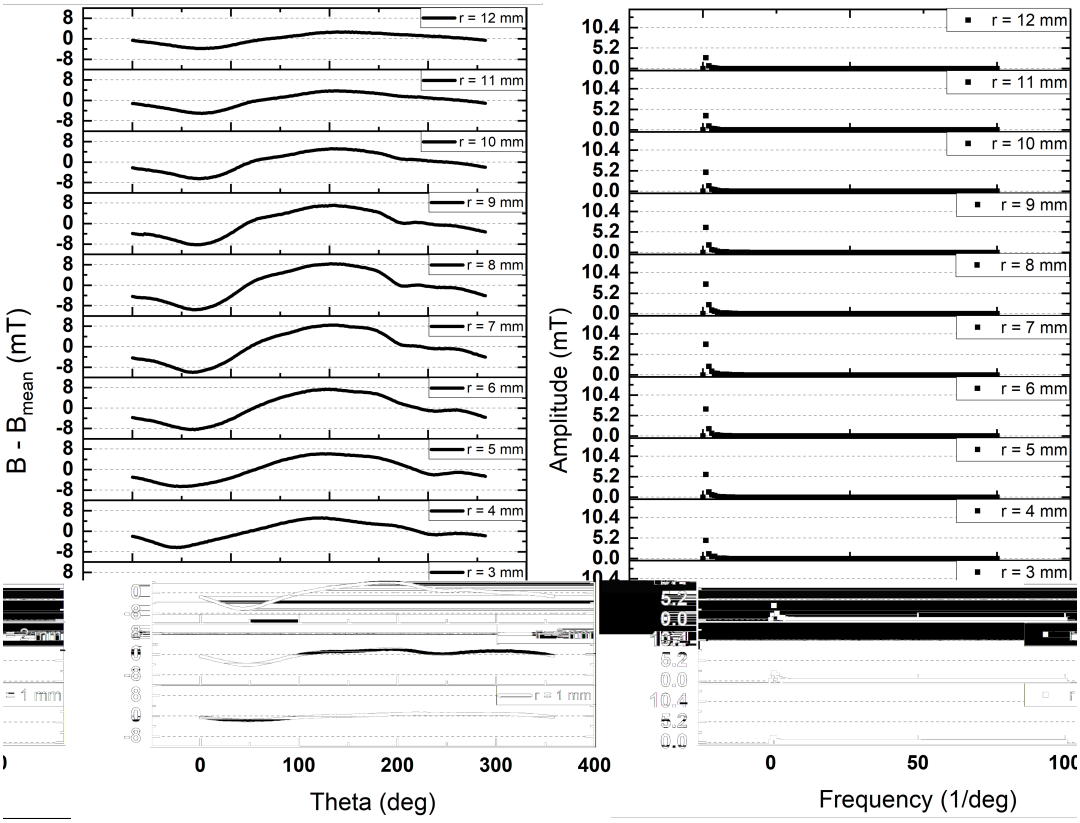

Figure A.5: Left: magnetic field of PM5 measured azimuthaly over its surface with r= 1 mm being the innermost radius. The radius of the magnet is 8.5 mm. The distance between the Hall sensor and the magnet surface is 2.7 mm. Right: the discrete Fourier transform of $B - B_{mean}$.

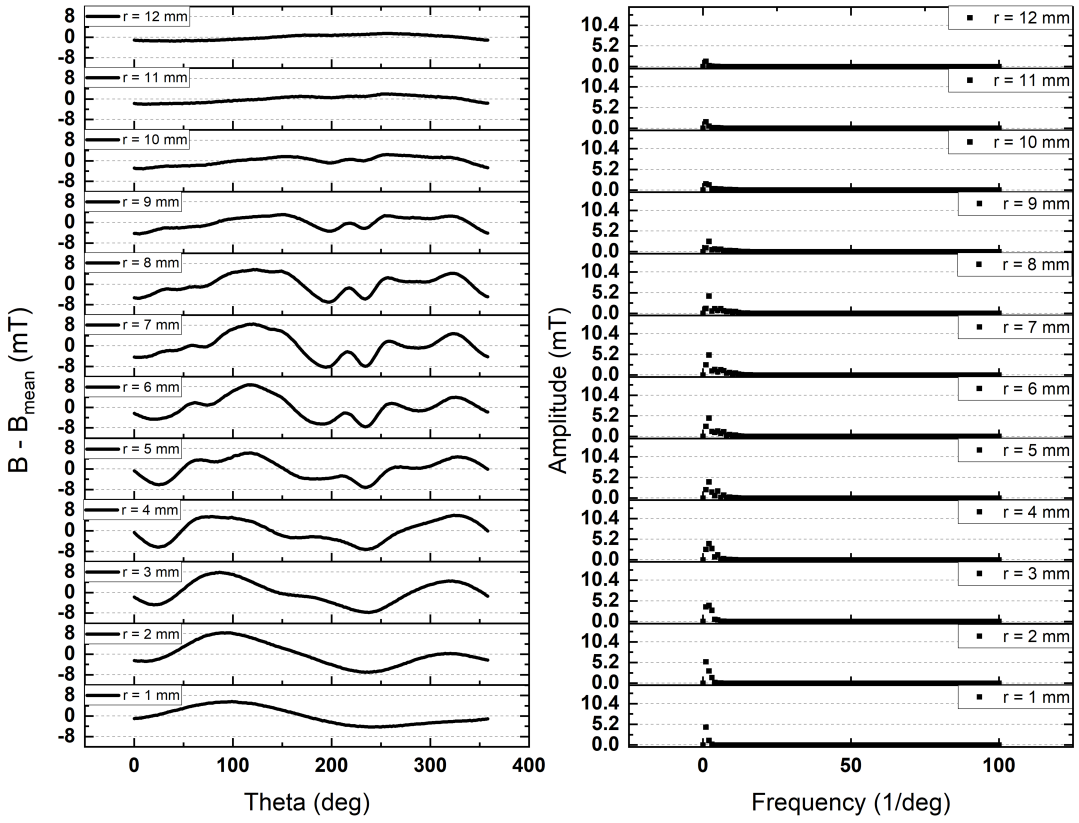

Figure A.6: Left: magnetic field of PM6 measured azimuthaly over its surface with r= 1 mm being the innermost radius. The radius of the magnet is 8.5 mm. The distance between the Hall sensor and the magnet surface is 2.7 mm. Right: the discrete Fourier transform of $B - B_{mean}$.

B

List of Publications

- **Mohammad Siamaki**, James G. Storey, and Rodney A. Badcock. "Towards a Non-Destructive Method of Mapping the *E*-*J* Relation Using Force Decay Measurements on Superconducting Bulks". In: IEEE Transactions on Applied Superconductivity 31.5 (Aug. 2021), pp. 1–5. Available on: `https://doi.org/10.1109/tasc.2021.3068980`.
- **Mohammad Siamaki**, James G. Storey, Lars Wiesehoefer, and Rodney A. Badcock. "Design, Build, and Evaluation of an AC Loss Measurement Rig for High-Speed Superconducting Bearings". In: Energies 15.4 (Feb. 2022), p. 1427. Available on: `https://doi.org/10.3390/en15041427`.